Computational Studies of the Mechanical Response of Nano-Structured Materials

Nathan Beets

Dissertation submitted to the faculty of the
Virginia Polytechnic Institute and State University
in partial fulfillment of the requirements for the degree of

Doctor of Philosophy
In
Materials Science and Engineering

Diana Farkas (Chair)
David Bai
Sean Corcoran
Michael Von Spakovsky

Jan 23, 2020, Blacksburg, VA
Keywords: Molecular Dynamics, Plastic Deformation, Nano-structured Metals, Interfaces

Computational Studies of the Mechanical Response of Nano-Structured Materials

Nathan Beets

Abstract

In this dissertation, simulation techniques are used to understand the role of surfaces, interfaces, and capillary forces on the deformation response of bicontinuous metallic composites and porous materials. This research utilizes atomistic scale modeling to study nanoscale deformation phenomena with time and spatial resolution not available in experimental testing. Molecular dynamics techniques are used to understand plastic deformation of metallic bicontinuous lattices with varying solid volume fraction, connectivity, size, surface stress, loading procedures, and solid density.

Strain localization and yield response on nanoporous gold lattices as a function of their solid volume fraction are investigated in axially strained periodic samples with constant average ligament diameter. Simulation stress results revealed that yield response was significantly lower than what can be expected form the Gibson-Ashby formalism for predicting the yield response of macro scale foams. It was found that the number of fully connected ligaments contributing to the overall load bearing structure decreased as a function of solid volume fraction. Correcting for this with a scaling factor that corrects the total volume fraction to "connected, load bearing" solid fraction makes the predictions from the scaling equations more realistic.

The effects of ligament diameter in nanoporous lattices on yield and elastic response in both compressive and tensile loading states are reported. Yield response in compression and tension is found to converge for the two deformation modes with increasing ligament diameter, with the samples consistently being stronger in tension, but weaker in compression. The plastic response results are fit to a predictive model that depends on ligament size and surface parameter (f). A modification is made to the model to be in terms of surface area to volume ratio (S/V) rather than ligament diameter (1/d) and the response from capillary forces seems to be more closely modeled with the full surface stress parameter rather than surface energy.

Fracture response of a nanoporous gold structure is also studied, using the stress intensity-controlled equations for deformation from linear elastic fracture mechanics in combination with a box of atoms, whose interior is governed by the molecular dynamics formalism. Mechanisms of failure and propagation, propagation rate, and ligament-by-ligament deformation mechanisms such as dislocations and twin boundaries are studied and compared to a corresponding experimental nanoporous gold sample investigated via HRTEM microscopy. Stress state and deformation behavior of individual ligaments are compared to tensile tests of cylinder and hyperboloid nanowires with varying orientations. The information gathered here is used to successfully predict when and how ligaments ahead of the crack tip will fracture.

The effects of the addition of silver on the mechanical response of a nanoporous lattice in uniaxial tension and compression is also reported. Samples with identical morphology to the study of the effects of ligament diameter are used, with varying random placement

concentrations of silver atoms. A Monte Carlo scheme is used to study the degree of surface segregation after equilibration in a mixed lattice. Dislocation behavior and deformation response for all samples in compression and tension are studied, and yield response specifically is put in the context of a surface effect model.

Finally, a novel bicontiuous fully phase separated Cu-Mo structure is investigated, and compared to a morphologically similar experimental sample. Composite interfacial energy and interface orientation structure are studied and compared to corresponding experimental results. The effect of ligament diameter on mechanical response in compressive stress is investigated for a singular morphology, stress distribution by phase is investigated in the context of elastic moduli calculated from the full elastic tensor and pure elemental deformation tests. Dislocation evolution and its effects on strain hardening are put in the context of elastic strain, and plastic response is investigated in the context of a confined layer slip model for emission of a glide loop. The structure is shown to be an excellent, low interface energy model that can arrest slip plane formation while maintaining strength close to the theoretical prediction.

Dislocation content in all samples was quantified via the dislocation extraction algorithm. All visualization, phase dependent stress analysis, and structural/property analysis was conducted with the OVITO software package, and its included python editor. All simulations were conducted using the LAMMPS molecular dynamics simulation package.

Overall, this dissertation presents insights into plastic deformation phenomena for nano-scale bicontinuous metallic lattices using a combination of experimentation and simulation. A more holistic understanding of the mechanical response of these materials is obtained and an addition to the theory concerning their mechanical response is presented.

Computational Studies of the Mechanical Response of Nano-Structured Materials

Nathan Beets

General Audience Abstract

Crystalline metals can be synthesized to have a sponge-like structure of interconnected ligaments and pores which can drastically change the way that the material chemically interacts with its environment, such as how readily it can absorb oxygen and hydrogen ions. This makes it attractive as a catalyst material for speeding up or altering chemical reactions. The change in structure can also drastically change how the material responds when deformed by pressing, pulling, tearing or shearing, which are important phenomena to understand when engineering new technology. High surface or interface area to volume ratios can cause a massive surface-governed capillary force (the same force that causes droplets of water to bead up on rain coat) and lead to a higher pressure within the material. The effect that both structure and capillary forces have on the way these materials react when deformed has not been established in the context of capillary force theory or crystalline material plasticity theory. For this reason, we investigate these materials using simulation methods at the atomic level, which can give accurate and detailed data on the stress and forces felt atom-by-atom in a material, as well as defects in the material, such as dislocations and vacancies, which are the primary mechanisms that cause the crystal lattice to permanently deform and ultimately break. A series of parameters are varied for multiple model systems to understand the effects of various scenarios, and the understanding provided by these tests is presented.

DEDICATION

-To my roguish and devilishly sexy group of friends and fellow grad students, who have been my constant empathizers and occasional enablers. You have brought me so much mirth, laughter, brotherhood, and beer in these past 3 years. You have been easily the best friends I have ever had, and I will miss you more than I can describe. You all are in no small part responsible for making this time in this place the best of my adult life so far.

-To the wonderful teachers and mentors who have opened up a new world of mathematical and scientific tools which I will use for the rest of my career, and hopefully life. Especially, to Dr. Sean Corcoran, Dr. David Bai, Dr. Michael Von Spakovsky, Dr. Karsten Albe, Dr. Amit Misra, Dr. Dwight Viehland, and Dr. Mitsu Murayama. Had I multiple brains and ample appendages, I would write papers with all of you.

-To my church community at BUMC Edges, for being the rock and reason on which I so often lean, and a steadfast, close-knit vessel for the holy trinity.

-To my radical, superb, top-notch advisor, Dr. Diana Farkas. You continue to inspire me and show me the beauty and complexity of the world on the nano-scale, and the joy in studying it. You have helped me find my confidence and conviction as a scientist, and are (outside the folks in the next paragraph) my single biggest role model. Thanks also for being very patient with my numerous mistakes.

-And to my parents, Doug and Helen. You have always been my shoulder to cry on, my reason in unreasonable times, my cheerleaders, and my biggest supporters throughout my graduate career, and my entire life. By far, the biggest proportion of my success I owe to you. More importantly, you continue to inspire me to use my gifts to make a better future for mankind, go against the grain, and fight the power. You're the true rock, the rebels with a cause, the warrior poets, and my heroes.

Table of Contents

COMMENTS ON DISSERTATION STRUCTURE:

Atomistic simulation has a vital role to play in mechanical behavior of nanostructured materials. The calculations are simple enough that a simulation can include millions of atoms over millions of time steps, yet accurate enough to realistically represent crystal defects. Atomic scale resolution of simulated systems is available to the researcher, allowing time and length scale resolution not available in experiment. When setting up a simulation, the researcher must ensure that the interatomic potential (which defines the forces felt by the atoms) is accurate, and the time-step for atom motion is small enough, and the overall sample structure and thermodynamic parameters are carefully constructed to replicate a physical structure and the simulation is run long enough to give meaningful results. If this can be accomplished, accurate three dimensional characterization of defects and nano-scale structural changes comparable to experiments are possible. Furthermore, careful extraction of bulk stress, energy, and position data from millions of atoms using advanced analysis algorithms can allow one to not only answer how, but also why certain defects form, and why certain mechanical properties (such as yield stress and elastic modulus) are observed. As such, circumstantial findings can be put in the context of larger established scientific understanding, and answer questions about the physical behavior of these structures generally.

This dissertation is compiled in manuscript format in accordance with the Virginia Tech Graduate School guidelines. It includes 5 manuscripts that have been prepared by the author during his doctoral candidacy. These manuscripts make up chapters 2-6. The first chapter contains explanations of simulation tools and scientific concepts that were excluded from the manuscripts for brevity. The order in which the manuscripts are presented is intended to follow the logical connections of their content. Chapters 2-5 focus on deformation of a nanoporous lattice, with somewhat different approaches. Chapter 2 (published in the Journal of Metals [1]) and chapter 3 (published in Acta Materialia [2]) focus on the deformation response of a nanoporous gold structure in uniaxial compression and tension, with carrying solid volume fraction of gold, and ligament diameter, respectively. Chapter 4 (also published in Acta Materialia [3]) investigates the fracture response of computational and experimental nanoporous samples, by use of an integrated MD and continuum coding scheme. Chapter 5 (in preparation to be submitted to Acta Materialia or Computational Materials Science) investigates the effects of adding silver to a nanoporous gold structure, and the difference between random placement of atoms, and surface segregation using a Monte-Carlo scheme. Chapter 6 (published in Acta Materialia [4]) investigates the mechanical response of a novel metallic composite structure, and develops a model system with mechanical behavior close to the theoretical predictions. The dissertation also includes all the front matter recommended by the Graduate School and a summary of the conclusions in this work following the chapters.

[1] N. Beets, D. Farkas, Mechanical Response of Au Foams of Varying Porosity from Atomistic Simulations, JOM 70(10) (2018) 2185-2191.

[2] N. Beets, D. Farkas, S. Corcoran, Deformation mechanisms and scaling relations in the mechanical response of nano-porous Au, Acta Mater. 165 (2019) 626-637.

[3] N. Beets, J. Stuckner, M. Murayama, D. Farkas, Fracture in Nanoporous Gold: an Integrated Computational and Experimental Study, Acta Mater. (2019).

[4] N. Beets, Y. Cui, D. Farkas, A. Misra, Mechanical response of a bicontinuous copper–molybdenum nano-composite: Experiments and simulations, Acta Mater. 178 (2019) 79-89.

LIST OF FIGURES:

LIST OF TABLES:

ACKNOWLEDGEMENTS AND ATTRIBUTIONS

Dr. Diana Farkas: Professor in the Materials Science and Engineering Department at Virginia Tech (VT). She is my dissertation advisor and committee chair. She principally conceived the research goals and provided advice, revisions and content in all stages of the research in chapters 2-6 of this dissertation.

Dr. Sean Corcoran: Professor in the Materials Science and Engineering Department at Virginia Tech (VT). He is one of my committee members, and helped set up the Cahn-Hilliard formalism in all chapters, and create a sample with the proper lattice orientation relation in chapter 6. He also helped with the modification to the yield response model in chapter 3.

Dr. Joshua Stuckner: Current materials researcher at NASA's Glenn Research Center, Dr. Stuckner developed the software AQUAMI, which allowed for the calculation of ligament diameter and standard deviation in all samples. Dr. Stuckner also provided all experimental results in chapter 4.

Dr. Mitsu Murayama: Professor in the Materials Science and Engineering Department at Virginia Tech (VT), and Dr. Stuckner's PhD advisor. Dr. Murayama was one of the project leaders, and helped Dr. Stuckner obtain the TEM images seen in chapter 4.

Dr. Karsten Albe: Professor in the Materials Modeling Department at the Technical University of Darmstadt, Germany. Provided research guidance and supplemental funding for most of the results provided in chapter 5.

Dr. Alexander Stukowski: Materials Scientist and Software Engineer at the Technical University of Darmstadt, Germany. Was the principal developer of OVITO, the dislocation extraction algorithm, and personally helped with the thermodynamics and setup in chapter 5.2.2.

Mr. Tim Kolb: Data Scientist at Cognizant. Provided assistance and ideas in obtaining many of the results in chapter 5, and came up with a surface stress test, which was used to obtain the values in tables 3-2, and 5-2, respectively.

Mr. Yuchi Cui: Graduate Student working under the advice of Dr. Amit Misra. Obtained all experimental results in chapter 6.

Dr. Amit Misra: Professor in the Materials Science and Engineering department at the University of Michigan. One of the project leaders who discovered the novel composite morphology investigated in chapter 6.

INTRODUCTION

Overview

The majority of the research presented in this dissertation used molecular dynamics simulation methods in conjunction with Embedded Atom Potential functions to study atom motion and sample behavior under different loading conditions. The following chapter is a brief overview of the fundamental mathematical implementation of molecular dynamics, and brief descriptions of some of the companion algorithms and simulation methods used.

Motivation

Material deformation in crystalline solids occurs by atoms responding to stresses induced by an applied external force. Commonly, this means line defects such as twins and dislocations being nucleated, which help accommodate the permanent change in shape of the overall sample. These fundamental mechanisms that govern permanent material deformation (called plastic deformation, or yielding) are extremely difficult to experimentally characterize due to their nano-scopic nature, and determining the fundamental causes of theses deformation phenomena is even harder, from an experimental perspective.

Understanding the structural and thermodynamic causes of the defects that induce defect nucleation and plastic deformation is paramount for fundamental understanding of novel nanostructured materials. So, to model atomic interactions and effectively replicate plasticity events, we use molecular dynamics; a simulation method that solves the many body problem for a defined collection of atoms by evaluating forces, velocities, and positions via an interatomic potential function, solved over a specified timestep atom by atom. The mechanics of this algorithm are described in chapter 1.

Original Contributions

Chapter 1: This is an outline of the major formalism of molecular dynamics, as well as the sample generation and analysis algorithms used to some degree for all original research presented here. There is nothing novel contained in this chapter.

Chapter 2: Experimental studies of nanoporous gold lattices with solid volume fractions below 0.5 consistently find strength values significantly less than what is predicted from the Gibson Ashby Scaling Relations for general macro-scale foams, given below:

$$E_{np} = E_{lig}\varphi^2$$

$$\sigma_{np} = (0.3)\sigma_{lig}\varphi^{\left(\frac{3}{2}\right)}$$

This chapter demonstrates that the Yield Stress and Elastic Modulus of nanoporous gold lattices deviate from this accepted formalism as a function of solid, load bearing connected ligament volume fraction. A series of molecular dynamics compression tests are performed on structures with common diameter but varying solid volume fraction. Less dense lattices consistently have

more unconnected ligaments, which do not contribute to the bearing any tensile or compressive load, and are thus excluded to get a more accurate, load bearing volume fraction estimate. A modified version of the connectivity parameter is proposed, which modifies total volume fraction as a function of load-bearing connectivity, given below.

$$\xi = (4\varphi^2)^{\frac{3}{2}} = 8\varphi^3 \; for \; \varphi < 0.5$$

Chapter 3: Experimental mechanical testing of nanoporous gold has demonstrated that these structures have a pronounced, and previously unexplained asymmetry in tensile vs. compressive yield response. This chapter replicates this asymmetry in their yield response with lattices being stiffer in tension, and more ductile in compression with molecular dynamics simulations. This study reveals that this tension/compression asymmetry arises from capillary phenomena, and stress imbalance at the surface, and the yield stress results are fitted to a model derived from fundamental thermodynamics, based on the surface area to volume ratio, given below:

$$\sigma_y(\mathrm{d}) = \sigma_0(\mathrm{d}) + \sigma_{surf}(\mathrm{d})$$

$$\sigma_s \begin{cases} -\dfrac{2Sf}{3V} & \text{(compression)} \\ \dfrac{2Sf}{3V} & \text{(tension)} \end{cases}$$

Chapter 4: Experimental fracture tests on Nanoporous Gold have revealed that during dynamic loading, the material experiences rapid, brittle fracture, despite nanoporous gold being a comparatively ductile material, for reasons that have remained yet unclear. This chapter investigates the fracture response of a nanoporous lattice, and is the first of its kind to simulate nanoporous fracture in a molecular dynamics environment with controllable stress tip intensity. We accomplish this by integrating a molecular dynamics simulation box with the displacement equations from linear elastic fracture mechanics for mode 1 fracture, given below:

$$u_x = \frac{K_I}{\mu}\sqrt{\frac{r}{2\pi}}\left[1 - 2\nu + \sin^2(\frac{\theta}{2})\right]\cos\left[\frac{\theta}{2}\right]$$
$$u_y = \frac{K_I}{\mu}\sqrt{\frac{r}{2\pi}}\left[1 - 2\nu - \cos^2(\frac{\theta}{2})\right]\sin\left[\frac{\theta}{2}\right]$$

We are able to show that strain hardening that comes from lattice warping around the crack tip propagates the strain field deeper with increasing stress intensity, which may explain the speed of advancement. Experimental studies have also shown that slow loading fracture experiments of NPG commonly have jumpy, irregular tip advancement rates, which is replicated by our simulation. We show that this irregular advancement is due to variation in ligament diameter, orientation, and morphology, and correlate tensile tests on hyperbolic and cylindrical nanowires to specific ligaments observed to fail in the lattice itself. These tests allowed us to algorithmically predict when and how specific ligaments would break with great accuracy.

Chapter 5: Experimental fabrication of nanoporous gold involves electrochemical dealloying of gold/silver leaf, which creates a majority gold nanoporous lattice, with some residual silver left behind. The effect this silver has on the mechanical properties of the nanoporous lattice had not been studied, so we carried out a series of molecular dynamics and monte carlo simulations to see what the effects were. Trends in Elastic Modulus and Yield Stress scaled almost exactly according to the surface stress model proposed in chapter 3, with no major deviation. It was found that surface composition directly controlled the magnitude of the surface stress, and thus scaled the yield stress. Elastic Modulus, on the other hand, was directly controlled by bulk composition.

Chapter 6: A novel bicontinuous composite morphology has been created by an experimental group at the University of Michigan, and has been shown to have Yield Stress and Elastic Modulus close to the theoretical prediction. Since the material generated was a nanostructure, phase-separated stress and strain field values as well as the energy of the interface were impossible to obtain experimentally, but vital to understand the mechanical behavior from a theoretical perspective. We performed a series of atomistic simulations to obtain this data. Our key findings were that a Kurdjumov-Sacchs interface orientation relationship observed experimentally allowed both lattices to have low residual stress fields and almost no interface disordering. This meant that the load borne by both lattices up to plasticity correlated to the ratio of elastic moduli, and Yield stress of both phases correlated to the predictions of confined later slip. Furthermore, no shear banding was observed, and the elastic strain even after 30% strain deformation, was only 2.3%.

Chapter 1: Molecular Dynamics Theory and Overview

1.1 Fundamental mechanisms; interatomic potentials, lattices, and force calculations

In order to calculate forces, velocities, and positions of atoms for sequential steps in a molecular dynamics simulation, one needs to first define an interatomic potential function, which describes the potential energy of an atom, dependent upon the distance between said atom and its nearest neighbors. For solid, crystalline materials, these potentials commonly have an attractive part (with overall negative interaction energy) and a repulsive part (with overall positive interaction energy) [5]. A simple example for single-body interactions in a copper system is shown in Figure 1-1 below:

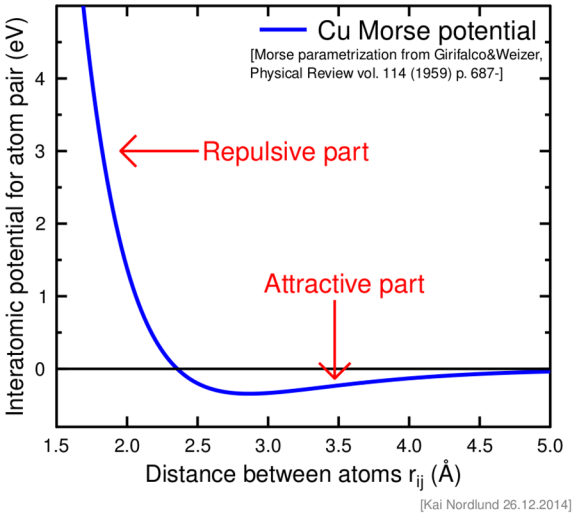

Figure 1-1: A simple copper two-body potential [6].

The repulsive part of the potential acts like a soft "wall" of sorts that allows atoms to be treated as point particles.

Calculating such a potential function perfectly for a model system of atoms (say, for example, crystalline copper) would require calculating the force contribution from every particle in the universe, but such a feat is untenable for any human, much less a graduate student, sustained solely by coffee and ramen. So, we can approximate the interaction closely by choosing a set number of nearest neighbor atoms.

$$V_{TOT} = \sum_i^N V_1(r_i) + \sum_{i,j}^N V_2(r_i, r_j) + \sum_{i,j,k}^N V_3(r_i, r_j, r_k) + \cdots \quad (1.1)$$

The form of equation 1.1 is very general for higher order interaction terms with more and more particles, of cutoff value N. One of the first and more simple interatomic potential functions used for a two-body interaction is the Leonard-Jones[5] interatomic potential function, given below:

$$V_{LJ} = 4\epsilon\left[\left(\frac{\sigma}{r}\right)^{12} - \left(\frac{\sigma}{r}\right)^{6}\right] \quad (1.2)$$

Here, ε is the depth of the potential well, and σ is the distance at which the potential crosses the zero line, and goes from net positive energy reaction to net negative energy reaction. This potential is good for modeling dipoles, noble gasses, and some liquids.

Another pair potential that was one of the first used to model molecular vibrations in solids was the Morse potential, given below;

$$V(r) = D_e\left(e^{-2a(r-r_e)} - 2e^{-a(r-r_e)}\right) \tag{1.3}$$

In this, D_e is the equilibrium bond energy, and r_e is the bond distance [6]. However for crystalline (especially FCC) metals specifically, the most accurate and common way of calculating the force is given by the Embedded Atom Method, which has general form given in equation 1.4:

$$V_{TOT} = \sum_i^N F_i\left(\sum_j \rho\left(r_{ij}\right)\right) + \frac{1}{2}\sum_{i,j}^N V_2\left(r_{i,j}\right) \tag{1.4}$$

Here, F_i is a function of the electron density (ρ) given a pair of atoms in a particular grouping. This function is commonly derived from electron density functional theory calculations (DFT). V_2 is a purely repulsive pair potential which can be fitted from electronic structure data, but is often tuned by actually testing the potentials [7]. This electronic structure data is gathered for specific crystal structures, so the equation above gives a many body interaction function that will energetically prefer the crystal structure of the material in question.

The utility of the EAM setup is its ability to incorporate findings from electronic structure data to a usable many-body potential that can generate accurate forces on an atom for up to 4 nearest neighbors. It can also be used with many atom types, so simulating multi-component alloys and composites with the EAM method is relatively easy. All interatomic potentials used in this dissertation were EAM potentials.

With an interatomic potential defined, calculating force vectors, positions and velocity vectors on atoms is relatively easy, since force is the position derivate of energy.

$$F = -\frac{d}{dr}U(r) \tag{1.5}$$

And of course, if one has a force vector, calculating acceleration, position, and velocity is merely a function of sequential time integrals. Using Newton's equations of motion, we can use time integrals to find velocity and position, as shown in equations 1.6 and 1.7.

$$F = ma, \frac{F}{m} = a = \frac{dv}{dt} = \frac{d^2x}{dt^2} \tag{1.6}$$

$$v = \int_t^{t+\Delta t} a * dt\,, x = \int_t^{t+\Delta t} v * dt \tag{1.7}$$

These time integrals are performed over set time, Δt called the simulation timestep. From the initial state, based on the initial positions of the atoms and velocity distribution, atom positions

are moved according to the distance dictated by their velocity calculated from the last step. From this new set of positions and velocities, new forces and velocities are calculated, and the simulation proceeds. It is important to find a timestep that is short enough so that atoms may not overlap causing unreasonably high forces and velocities, effectively causing the structure to blow up after only a few steps, yet not too short that obtaining meaningful deformation results over long enough periods of time becomes untenable. For most metals, a femtosecond is reasonable, and that was the timestep defined for all simulations in this dissertation.

Once an interatomic potential has been created, one needs an atomic structure to simulate, and have the potential act on. If the crystal structure and correspondent lattice parameters are known, one can define a parallelepiped and fill it with atoms with the dimensions and morphology or grain structure desired. "Atoms" here are represented by point masses, but since they are acted on by a potential with a repulsive term, no radius needs to be defined. Single crystalline, fully periodic material is the simplest and easiest case by far. However, novel morphologies were created for much of the work presented in this dissertation by an alternate method. This will be discussed in section 1.9.

1.2 Temperature, velocity, and pressure calculations

It is often desirable to give the collection of atoms in question an initial velocity distribution, so it can start out at equilibrium temperature. At the length scales studied by molecular dynamics, kinetic energy and the mean velocity distribution of atoms at any given point determines the temperature of the solid in question, according to the Maxwell-Boltzmann distribution [8]:

$$f_v = \left(\frac{m}{2\pi k_b T}\right)^{\left(\frac{3}{2}\right)} 4\pi v e^{-\frac{mv^2}{2k_b T}} \tag{1.8}$$

where m is mass of the particles in question, k_b is Boltzmann's constant, T is temperature, and v is velocity, which can be written as

$$v = \sqrt{v_x^2 + v_y^2 + v_z^2} \tag{1.9}$$

One can use a random number generator to assign velocities to atoms that conform to this mean velocity for the desired temperature. Sampling random velocities from the distribution (f_v) will give a collection of atoms moving around the mean of this distribution, and with enough particles, one can be certain a temperature reasonably close to "T" can be obtained.

With the system temperature defined, we can calculate the system pressure. This is calculated as a virial stress term, given as:

$$P = \frac{Nk_b T}{V} + \frac{1}{3V}\sum_{i=0}^{N}\sum_{j=0}^{i-1}(r_i - r_j)f_{ij} \tag{1.10}$$

where P is the calculated pressure of the system and V volume of the simulation box. f_{ij} is the force calculated atom by atom. The second term can be expressed as the summed dot products of each atom pair's relative position vector and interaction force. Often, MD simulations include a cutoff radius, such that atoms that are far enough apart do not interact. Thus, in large simulations,

cumulative f_{ij} is equal to zero, even though the forces felt by individual atoms are of course non-zero.

Various ensembles can be applied to this system, depending on what the user wants to investigate. The most computationally efficient ensemble is the canonical, or NVT ensemble, which allows the user to define Number of particles, Volume of the box, and Temperature. However, for the majority of our simulations, we wanted to fix the pressure on non-deformed sides of a box to be zero. So, we used the NPT ensemble, which fixes Number of particles, Pressure, and Temperature, respectively. Controlling pressure and temperature will be discussed in the next section.

1.3 Thermostatting and Barostatting.

Controlling temperature externally requires maintaining thermal equilibrium with an external mass that is maintained at a constant temperature, called a heat bath. This method was originally developed by Noose, and later by Hoover, and is commonly referred to as a Noose-Hoover thermostat [3]. Use of a Noose-Hoover thermostat alters the equations of motion to the form

$$\frac{dr_i}{dt} = v_i; \quad \frac{dv_i}{dt} = \frac{f_i}{m_i} - \zeta v_i \tag{1.11}$$

The coefficient "ζ" is a variable calculated timestep by timestep that acts on the entire collection of atoms in the simulation box. It is calculated from the equation

$$\frac{d\zeta}{dt} = \frac{1}{t_{T^2}}\left(\frac{T}{T_0} - 1\right) \tag{1.12}$$

Where t_T is the thermal relaxation time, which must be specified by the user. Importantly, the Noose-Hoover thermostat does not fix temperature to be a constant, but sets a time-averaged temperature of T_0. Other thermostats have been developed to satisfy the NVT ensemble, which are the Anderson [9], Berendsen [10] and Langevin [11] thermostats, but those are not used in any of the work presented in this dissertation.

If a fixed system pressure is desired in addition to fixed temperature, an isobaric-isothermal or NPT (fixed Number of atoms, Pressure and Temperature) ensemble may be employed. The numerical approach to controlling pressure is a barostat. Adjusting the pressure is most commonly done by altering the simulation box size and relative closeness of atoms. Due to the huge force dependence on position of interatomic potential functions, minute changes in atomic position can produce unrealistic forces and velocities, and can put the sample under enormous stress.

One of the most commonly used barostats, and the one used in this dissertation is the Nose-Hover Barostat [12]. A NPT ensemble with a Nose-Hoover barostat uses the altered equations of motion given in equation 1.13, below.

$$\frac{dr_i}{dt} = v_i + \eta(r_i - r_{cm}); \quad \frac{dv_i}{dt} = \frac{f_i}{m_i} - (\zeta + \eta)v_i \tag{1.13}$$

Here, r_{cm} is the center of mass of the system and η is the barostat friction coefficient. η and ζ, like the Nose-Hoover thermostat, are system-wide, time-dependent variables controlled by the differential equations

$$\frac{d\zeta}{dt} = \frac{1}{t_{T^2}}\left(\frac{T}{T_0} - 1\right); \frac{d\eta}{dt} = \frac{1}{Nk_bT_0t_{p^2}}V(P - P_0) \tag{1.14}$$

where tP is the barostat relaxation time, $P0$ is the target pressure. For the case of imposed isotropic pressure, η, P and P_O may be considered scalars. The simulation box geometry is, in the isotropic case, controlled by the differential equation

$$\frac{dR}{dt} = \eta R \tag{1.15}$$

where R is a 3x3 matrix containing the cell edge vectors. For anisotropic pressure conditions, P and P_O may be treated as 3x3 symmetric stress symmetric tensors, necessarily making η a 3x3 symmetric tensor. The components of $P0$ may be set independently, coupled with one another or excluded from barostating. Also used in MD are the Berendsen [10] and Perinello-Rahmen [13] barostats. But again, we only use the Noose-Hoover barostat for this work.

1.4 Boundary Conditions

Spatial boundary conditions describe how atoms near the simulation box edges are treated. The effects of the very short length scales inherent to atomistic modeling can be partially eased by selecting periodic boundary conditions. When periodic boundary conditions are employed, atoms can influence each other across opposite boundaries. If an atom is forced out of the top simulation box, it is placed in the bottom of the simulation box such that the summed distance between the original and final positions and the points at which it crossed the top and bottom boundaries conforms to the solution for the equation of motion for that particle at that timestep. The use of non-periodic boundaries is used to model surfaces in MD simulations of solids. Periodic boundary surfaces must be parallel and shaped exactly alike. This is achievable in any parallelepiped-shaped simulation box. Typically, barostating can only be applied to spatial components that have periodic boundaries. One drawback to using periodic boundary conditions is that longer ranging effects, like strain fields, caused by nano-scale phenomena, such as dislocations, can extend across the boundaries. If the simulation box is short enough in a periodic direction this can cause an artificial change in the magnitude of these effects. But for the kinds of structures and the length scales we are investigating, this is not an issue.

1.5 Deformation and Strain Rate.

It should be noted that since time steps in molecular dynamics are so small, and for each time step, forces, velocities, and positions for every single atom must be calculated, any kind of deformation performed on a sample of many millions of atoms will by necessity have strain rates of between (1*10^9), and (1*10^5), which for a 0.1 strain deformation, would require between 1,000,000 and 1,000,000,000 total timesteps. “Slow” simulations in this way are not feasible for systems of millions of atoms, since such a simulation could literally take years. This is not a major problem, however, because several studies have showed that strain rate has little effect on the elastic modulus and yield stress for EAM-governed metals and alloys, until significantly after

plasticity [14, 15]. When deforming, all mechanisms of thermostatting and barostatting apply, except no pressure control is fixed on the side of the sample being deformed.

1.6 Dislocation Extraction Algorithm.

For all chapters included in this dissertation, we investigated dislocation content and behavior by use of the Dislocation Extraction Algorithm, developed by Alexander Stokowski [16]. This method uses the Common Neighbor Analysis Method (CNA) developed in 1987 by Honeycutt and Andersen to identify clusters of "disordered" atoms with atom placements that do not conform to the defined crystal structure to within a set position tolerance [17]. These atoms are isolated, and a closed, two-dimensional manifold is constructed around the closed region of disordered atoms. The crystalline atoms surrounding this manifold are examined, and a Burgers circuit and vector is constructed for each manifold segment. The mesh is minimized down to a single line running along the center of the manifold tube, and a total length defined. When used in conjunction with a three dimensional visualization package, this can allow the user to visualize dislocations as they move through a material, and track their density at any given timestep. Wherever in the text we discuss "residual dislocation density," this is how those values were obtained.

1.7 Cahn Hilliard Formalism:

A note should be made about the method used to generate all samples used for this research. All samples studied in this dissertation are constructed from bicontinuous, fully separated phase fields, which has been shown to reasonably replicate nanoporous structures, and shows ligament diameter and length distributions consistent with nuclear magnetic resonance experiments. This method consists of defining a three-dimensional, lightly perturbed phase field with perturbation over an arbitrary order parameter, ranging from values of -1 to 1. The equation below is solved as a function of time, for defined timestep, Δt.

$$\frac{\partial c}{\partial t} = D\nabla^2(c^3 - c - \gamma\nabla^2 c) \tag{1.16}$$

Here, D is the diffusion coefficient, c is the concentration varying from -1 to 1, and Υ is the square of the square of the length of the transition regions between different domains [18]. When this is solved over a perturbed phase field, it gives clean phase separation and a bicontinuous, light/dark phase structure. One can then define all parts of the phase field above a certain cutoff parameter to be "solid," and these can be filled with atoms. Alternately, you can define the dark and light phase as "solid phase 1," and "solid phase 2," or something similar, and fill both with an atomic lattice of your choosing. This system can be solved defining periodic boundary values, so a fully three dimensional periodic structure is produced.

1.8 Bibliography

[1] G. Vetterick, A.C. Leff, M. Marshall, J.K. Baldwin, A. Misra, K. Hattar, M.L. Taheri, Direct observation of a coincident dislocation- and grain boundary-mediated deformation in nanocrystalline iron, Materials Science and Engineering: A 709 (2018) 339-348.
[2] J. Du, F. Mompiou, W.-Z. Zhang, In-situ TEM study of dislocation emission associated with austenite growth, Scr. Mater. 145 (2018) 62-66.

[3] S. Yin, G. Cheng, G. Richter, H. Gao, Y. Zhu, Transition of Deformation Mechanisms in Single-Crystalline Metallic Nanowires, ACS Nano 13(8) (2019) 9082-9090.
[4] J. Stuckner, M. Murayama, Mechanical properties of nanoporous gold subjected to tensile stresses in real-time, sub-microscopic scale, Journal of Materials Science 54(18) (2019) 12106-12115.
[5] J.E. Jones, S. Chapman, On the determination of molecular fields. —II. From the equation of state of a gas, Proceedings of the Royal Society of London. Series A, Containing Papers of a Mathematical and Physical Character 106(738) (1924) 463-477.
[6] L.A. Girifalco, V.G. Weizer, Application of the Morse Potential Function to Cubic Metals, Physical Review 114(3) (1959) 687-690.
[7] S.M. Foiles, M.I. Baskes, M.S. Daw, Embedded-atom-method functions for the fcc metals Cu, Ag, Au, Ni, Pd, Pt, and their alloys, Physical Review B 33(12) (1986) 7983-7991.
[8] H.J.W. Müller-Kirsten, Basics of Statistical Physics, WORLD SCIENTIFIC2012.
[9] H.C. Andersen, Molecular dynamics simulations at constant pressure and/or temperature, The Journal of Chemical Physics 72(4) (1980) 2384-2393.
[10] H.J.C. Berendsen, J.P.M. Postma, W.F. van Gunsteren, A. DiNola, J.R. Haak, Molecular dynamics with coupling to an external bath, The Journal of Chemical Physics 81(8) (1984) 3684-3690.
[11] T. Schneider, E. Stoll, Molecular-dynamics study of a three-dimensional one-component model for distortive phase transitions, Physical Review B 17(3) (1978) 1302-1322.
[12] G.J. Martyna, D.J. Tobias, M.L. Klein, Constant pressure molecular dynamics algorithms, The Journal of Chemical Physics 101(5) (1994) 4177-4189.
[13] M. Parrinello, A. Rahman, Polymorphic transitions in single crystals: A new molecular dynamics method, J. Appl. Phys. 52(12) (1981) 7182-7190.
[14] S. Ding, X. Wang, Strain rate and temperature effects on the mechanical properties of TiN/VN composite: Molecular dynamics study, Journal of Alloys and Compounds 814 (2020) 152151.
[15] M. Yaghoobi, G.Z. Voyiadjis, The effects of temperature and strain rate in fcc and bcc metals during extreme deformation rates, Acta Mater. 151 (2018) 1-10.
[16] A. Stukowski, K. Albe, Extracting dislocations and non-dislocation crystal defects from atomistic simulation data, Model. Simul. Mater. Sci. Eng. 18(8) (2010) 13.
[17] J.D. Honeycutt, H.C. Andersen, Molecular dynamics study of melting and freezing of small Lennard-Jones clusters, The Journal of Physical Chemistry 91(19) (1987) 4950-4963.
[18] J.W. Cahn, J.E. Hilliard, Free Energy of a Nonuniform System. I. Interfacial Free Energy, The Journal of Chemical Physics 28(2) (1958) 258-267.

Chapter 2: Mechanical Response of Au Foams of Varying Porosity from Atomistic Simulations

2.0: Abstract:

The results of atomistic simulations of the deformation response of Au nano-foams with different levels of porosity and constant ligament size are presented. The results of virtual tensile testing are compared with the predictions from scaling laws for both the elastic modulus and the yield strength. It is shown that the mechanisms of plasticity can vary with the degree of porosity. The results are consistent with a model in which, as the porosity increases, only a fraction of the ligaments carry the load, resulting in an apparent relative density that is lower that the actual value.

2.1 Introduction

Nanoporous metals, and specifically nanoporous gold foams, have been attracting considerable attention as a novel material in recent decades[1]. The mechanical properties of nanoporous metals are of particular interest for a variety of reasons, mostly derived from their typically high surface to volume ratio[2]. The application of the principle of ‘‘smaller is stronger’’, which has been observed by numerous studies of nanowires[3], applies to macroscopic foam samples of very small ligament diameters. It is expected that, since nanowires are observed to have very high stiffness, nanoporous metals would exceed their macro-scale counterparts in stiffness by several orders of magnitude[2]. The mechanical strength of nanoporous materials has been studied using different experimental techniques, such as nano-indentation[4-6]. The nanoporous metal foams modeled in these studies are synthesized through dealloying[6-8].

From a basic understanding point of view, foams provide the unique opportunity to link nanoscale properties with microscale measurements. Efforts to predict the properties of nonporous gold (specifically its yield stress and elastic modulus) center around the Gibson–Ashby formalism, [9-10] which predicts properties as functions of the relative density of the foam, as follows:

$$E_{np} = E_{lig}\varphi^2 \tag{1}$$

$$\sigma_{np} = (0.3)\sigma_{lig}\varphi^{\left(\frac{3}{2}\right)} \tag{2}$$

Here, E is the elastic modulus, φ the relative density or volume fraction of a solid, and σ the yield stress involved. The subscript ‘‘np’’ represents the nanoporous sample values, while the subscript ‘‘lig’’ represents the properties of the ligaments of corresponding size. In general, the mechanical response of the ligaments is not the same as bulk Au when the ligaments are nano-sized.

In many instances, the observed strength and stiffness of these structures were significantly less than predicted by the Gibson–Ashby formalism [11-12]. However, as the relative density increases, the observed behavior comes closer to the prediction of the model by Gibson and Ashby.

Understanding this phenomenon has been difficult due to the incomplete knowledge of the fundamental mechanisms governing the behavior of nanoporous structures. Several studies, both in experiment and in simulation, have addressed the significant role played by the surfaces[13-14]. It has also been demonstrated that, when put in an electrochemical environment, these properties can to a degree be tuned with varying external conditions[15]. Surface effects increase with the inverse of the ligament diameter and, below a critical ligament size, samples can become mechanically unstable, even without applied loading[16-17].

In this paper, we utilize atomistic computer simulation techniques to perform virtual tensile mechanical tests on a group of 6 samples with constant 5.5-nm ligament diameter with solid volume fractions ranging from 27% to 50%. Virtual tensile tests of these samples and a corresponding pillar of the same 5.5-nm diameter are carried out. This allows for testing the yield stress and elastic modulus predictions given by the Gibson–Ashby equations. An analysis of the deformation mechanisms for these different samples is also reported.

2.2 Methods

2.2.1 Sample Generation

Several methods have been developed and published to computationally generate bi-continuous nanoporous structures with porosity higher than 50%[18-20]. Crowson et al[17].developed a strategy based on spinodal decomposition, and utilized a phase field technique to solve the Cahn–Hillard equations. This technique separates an immiscible alloy into two distinct phases, closely resembling the structure and ligament size distribution of the experimental samples of nanporous Au obtained by dealloying [16,17], and is the one that was chosen to generate the series of digital samples utilized in the present work. Stability studies also conducted by Crowson [17] found that pillars smaller than 1.7 nm tend to collapse, due to the large surface to volume ratio. Kolluri et al [18]. found that, for ligaments between 2.1 nm and 1.5 nm, nanoporous digital samples collapse without any applied stress. We therefore chose a larger ligament size of 5.5 nm.

Using this technique, we created a series of samples with ligament diameters of 5.5 nm and relative densities ranging from 27% to 50%. These digital model structures were all generated with periodic boundaries in the X, Y, and Z directions, which in all samples coincided with the three <100>-type directions of the lattice[16]. The samples were cubes of 43.0 nm size and contained 1.3–2.5 million atoms. We note that maintaining a constant ligament size and changing the volume fraction

resulted in samples that are not self-similar. Figure 1 shows the microstructure of the digital samples with 50% and 27% relative density.

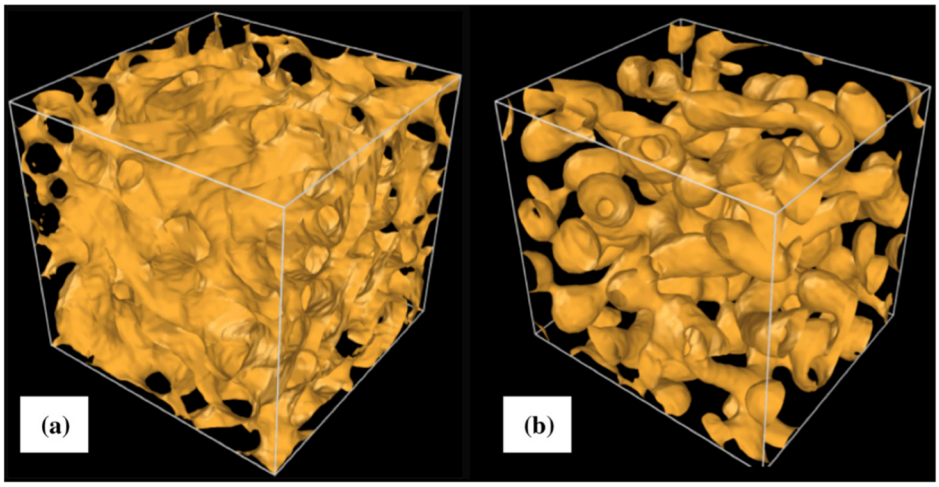

Figure 2-1: The Morphology of the digital samples with (a) 50% and (b) 27% relative density

We characterized the morphology of the samples created. The AQUAMI code developed by Stuckner[21] was used to obtain ligament size distributions as a function of the solid volume fractions[21]. The results were fitted to Gaussian distributions for each sample, and the resulting average ligament diameters and standard deviations obtained. All the samples have average ligament sizes within 15% of the target 5.5 nm. The standard deviation of the ligament size distribution was found to vary from 1.5 nm for the larger solid fractions to 2.5 nm for the lowest relative densities. The ratios of standard deviation to average ligament size in our samples compare well with experimentally measured distributions in dealloyed samples [22].

2.2.2 Sample Relaxation and Virtual Tensile Testing

Relaxation and deformation were performed using the LAMMPS molecular dynamics (MD) implementation and EAM interatomic potential functions for Au developed by Foiles et al[23,24]. Each sample, including the 5.5-nm pillar mentioned, was relaxed and deformed using a Noose–Hoover thermostat and barostat, and equilibrated at 300 K for approximately 2 ns. After equilibration, each sample was deformed in tension at a rate of 3 9 10^{8} s^{-1} up to 5% strain. The tensile axis coincided with the [001] direction of the lattice, perpendicular to the box edge. The deformation was strain-controlled with the total stress on the sample monitored as the deformation proceeds, resulting in standard stress– strain curves. Visualization of defects was per- formed using the OVITO software[25]. This included the analysis of dislocations by the DXA dislocation extraction formalism[26].

2.3 Results

2.3.1 Stress–Strain Results

Figure 2a shows the stress–strain curves obtained for the tensile deformation of the samples with various levels of porosity. Figure 2b shows the corresponding test performed on a simple cylindri- cal nanopillar of the same 5.5-nm diameter. The elastic modulus of the pillar is somewhat smaller than that of bulk Au. This is due to the elastic anisotropy of Au that gives a modulus for the <100> orientation lower than that for polycrys- talline bulk Au. The yield

strength of the pillar is significantly higher than that of bulk Au, a s expected from the ‘‘smaller is stronger’’ effect for nano-sized pillars.

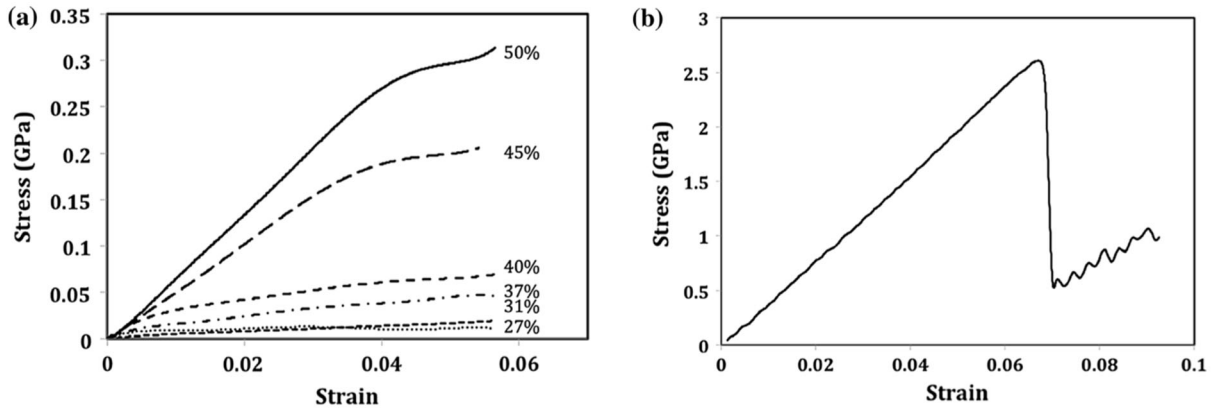

Figure 2-2: Stress/Strain curves obtained for (a) the tensile deformation of the samples with 5.5nm ligament diameter and various levels of relative density and (b) a nanopillar of 5.5nm diameter

As the porosity is increased, the samples behave as significantly softer in both the elastic and plastic regimes. This is expected from the Gibson–Ashby relationships. In addition, a lower solid fraction can affect ligament connectivity, and lower ligament connectivity can significantly affect the load-bearing characteristics of the structure. Disconnected liga- ments can drastically lower the stiffness and strength. Even if our samples are generated using the same formalism, they are not self-similar and they can have different ligament connectivity, which may affect the mechanical response.

Table I shows the elastic modulus and yield strength derived from the results of Fig. 2. These results can be compared with the Gibson–Ashby predictions calculated based on the elastic response of the nanopillar of the same ligament diameter and simulated using the same interatomic potential and identical conditions. It is seen that both the elastic moduli and yield strengths observed for the higher porosity levels are much lower than the Gibson– Ashby predictions.

Table 2-1: Elastic Modulus and Yield Strength Obtained in the Virtual Tensile Tests.

Relative Density (%)	Elastic Modulus (GPa)	Predicted Elastic Modulus (GPa)	Yield Strength (GPa)	Predicted Yield Strength (GPa)
22	0.07	1.69	0.0012	0.0814
27	0.14	2.54	0.004	0.111
31	0.24	3.35	0.0104	0.136
37	0.98	4.78	0.027	0.178
40	1.54	5.59	0.063	0.199
45	5.06	7.07	0.176	0.238
50	6.81	8.73	0.255	0.279
100 (pillar)	35	35	2.631	2.631

This agrees with previous observations by Liu et al.[27], who observed that the strength and elastic modulus of macroscopic nanoporous Au samples are much lower than that predicted by the Gibson– Ashby scaling laws. They attributed this discrepancy to lowered network connectivity in the nanoporous structure, and introduced the concept of effective relative density.

In order to visualize the origin of this significant difference, we studied the non-uniform displacements of the individual atoms in the sample for various degrees of porosity. The non-uniform dis- placement values were obtained by subtracting the uniform displacement of the overall sample from the individual atomic displacement of each atom. Figure 3 shows the results obtained for the sample with 27% relative density, with atoms colored by the magnitude of their non-uniform displacements after 5% tensile deformation. Different regions of the sample are deforming in significantly different ways, with some atoms experiencing very large displacements, indicating that they are not con- strained by the bi-continuous structure. This is also clearly seen in the study of the non-uniform dis- placements of the individual atoms, as shown in Fig. 4. Samples with lower levels of porosity do not show a large variation of displacement values, as also shown in Fig.4. As the relative density decreases, significant fractions of the atoms in the sample experience large displacements, which can be attributed to a lowered connectivity of the structure.

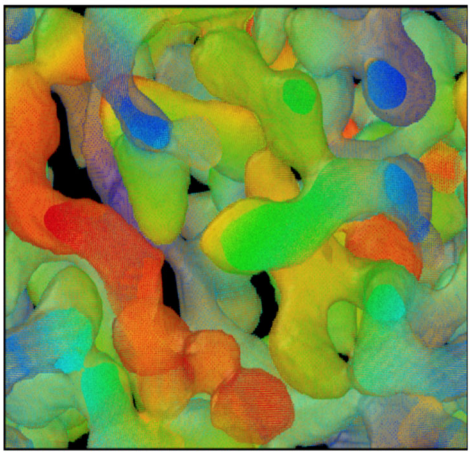

Figure 2-3: Sample with 27% relative density with atoms colored by the magnitude of their non-uniform displacements after 5%tensile deformation.

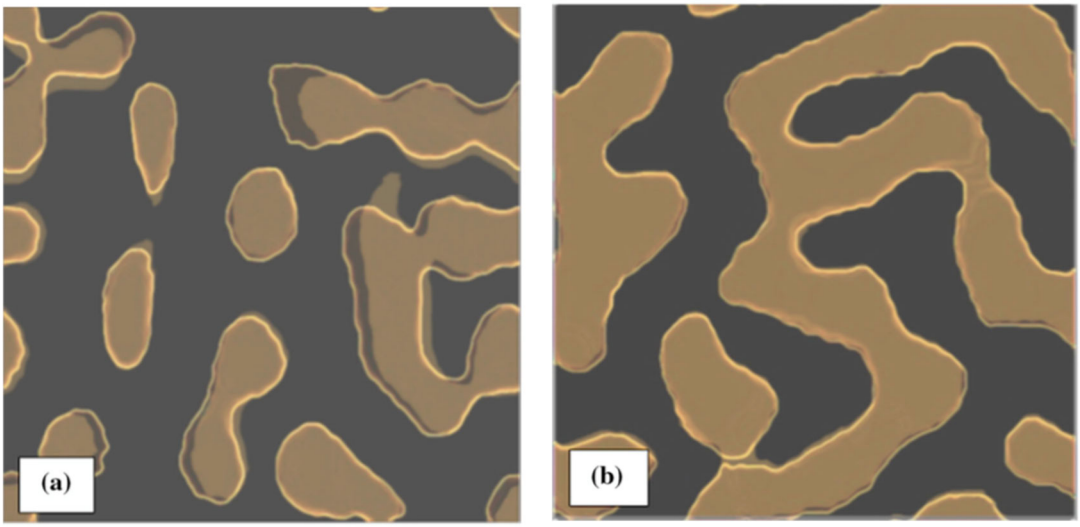

Figure 2-4: Non-uniform configuration change for the samples of (a) 27% and (b) 50% relative density, both after 5% tensile deformation.

Figure 5 shows the configurational change after 5% deformation in representative slices of the samples with 50% and 27% relative density. The sample with higher relative density deforms in a more uniform way, whereas the sample with lower relative density exhibits configurational changes due to non-uniform deformation. These changes can be attributed to lower constraints imposed by the bi- continuous structure. This can be interpreted as due to lower connectivity in the higher porosity sample.

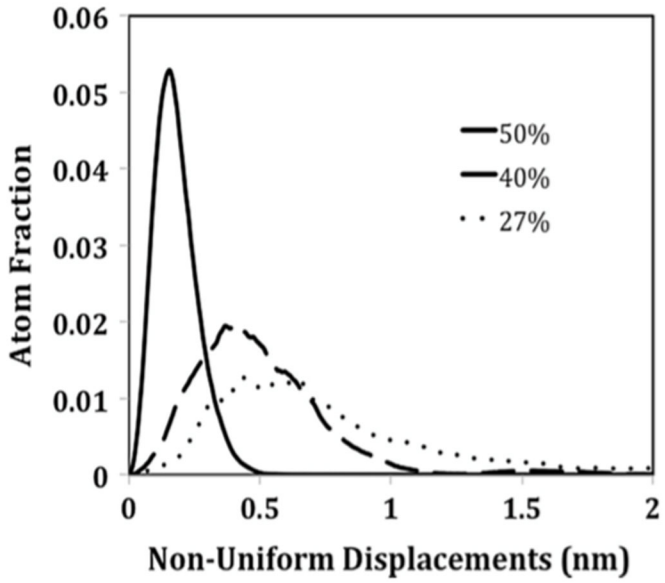

Figure 2-5: Histograms of the non-uniform displacements for the samples with 50%, 40%, and 27% relative solid density with a bin size of 0.01 nm. The y-axis is the fraction of ato,s having displacements with 0.01 nm of the value in the x-axis.

2.3.2 Scaling of the Elastic Modulus

The observed scaling of the elastic modulus is shown in Fig. 6a, compared with the predictions of the Gibson–Ashby model. The Gibson–Ashby scaling was calculated using the value of 35 GPa, obtained for the modulus of the nanopillar with the same diameter as the foam ligaments in our nanoporous samples under the same conditions. It is seen that the modulus observed for the higher porosity levels is much lower than the Gibson– Ashby predictions.

Following Liu et al.[27], we modified the scaling equations by introducing an effective relative den- sity for the foam. We propose a modified effective relative density for foams that have densities lower than 0.5. In order to model our MD results, the modified apparent density, u_a, can be assumed, as follows:

$$\frac{\varphi_a}{\varphi} = 4\varphi^2 \; for \; \varphi < 0.5 \quad (3)$$

$$\frac{\varphi_a}{\varphi} = 1 \; for \; \varphi > 0.5 \quad (4)$$

Figure 6a also shows the scaling predicted using the Gibson–Ashby formalism with this apparent relative density instead of the actual value, in good agreement with our simulation results. This means that, for solid fractions lower than 50%, we find that the elastic modulus does not obey the Gibson–Ashby scaling with the square of the solid fraction, but rather follows a sixth power dependence on the solid fraction.

$$E_{np} = 16E_{Lig}\varphi^6 \; for \; \varphi < 0.5 \quad (5)$$

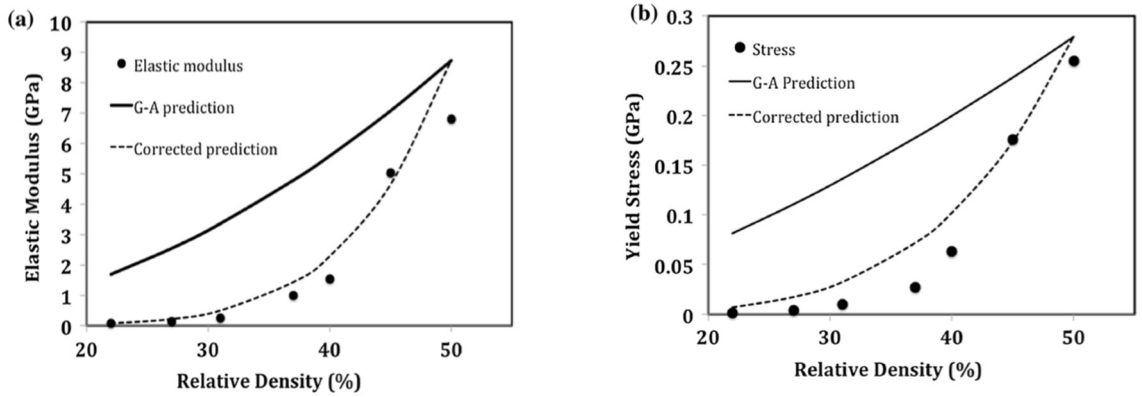

Figure 2-6: (a) Scaling of the elastic modulus with the foam relative density. (b) Scaling of the yield strength with the relative foam density

2.3.3 Scaling of the Yield Strength and Deformation Mechanisms

Figure 6b shows the observed scaling for the yield strength. The Gibson–Ashby scaling was calculated using the value of 2.631 GPa, obtained for the strength of the nanopillar of the same diameter as the foam ligaments under the same conditions. (Figure 2b). The values obtained in our simulations are lower than expected from the Gibson–Ashby scaling relationship. However, if the effective rela- tive density proposed above is used in the scaling relationship for the yield

strength, the agreement is quite good. This means that the yield strength values depend on the actual relative density as follows:

$$\sigma_{np} = 2.4\sigma_{lig}\varphi^{4.5} \; for \; \varphi < 0.5 \tag{6}$$

2.3.4 Deformation Mechanisms

Plastic deformation was found to occur through the emission of dislocations from the ligament surfaces. The dislocations emitted from the surfaces were mostly Shockley partial dislocations that travel throughout the ligament. As they travel through the ligament, they create stacking faults within the ligaments. The process can be then quantified by the fraction of atoms in these stacking faults, identified by the hcp-like environment. Our samples contained up to 2.4% hcp atoms for defor- mation levels of 5%.

We analyzed the evolution of the dislocation densities in the samples as they are deformed and the results are shown in Fig. 7b. The dependence on the relative density for a 5% deformation level is shown in Fig. 7a. The dislocation density in the deformed sample increases with decreasing solid fraction. Most importantly, we analyzed the distri- bution of the dislocations in the sample and found that, for the lower solid fractions, the dislocation density is not uniform but significantly concentrated in the nodes. This is shown in Fig. 7c and d. A possible explanation for this is the presence of buckling in the ligaments for the lower relative densities. This could also explain the larger non- uniform displacements that were observed for those samples.

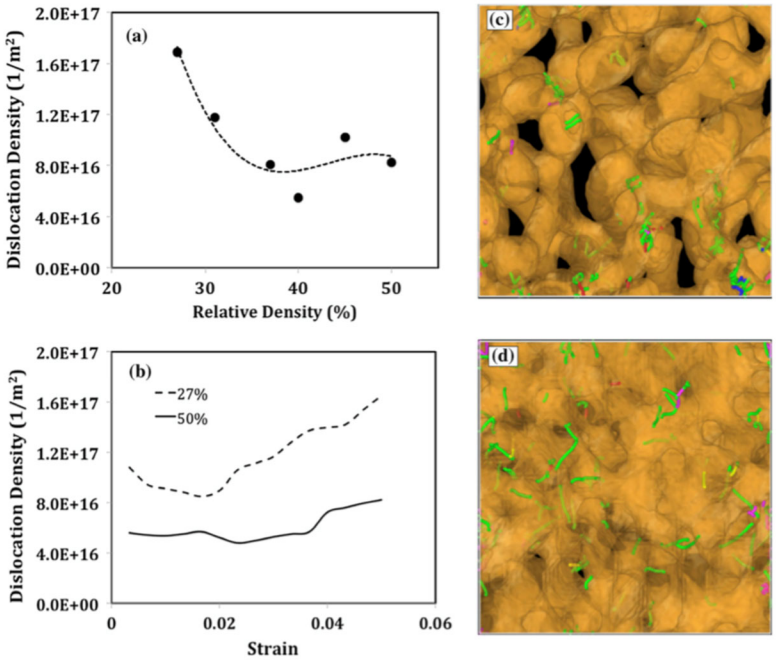

Figure 2-7: (a) Dislocation density present in the samples after 5% deformation for various levels of porosity. (b) Dislocation density evolution in the samples with 50% and 27% relative density after 5% tensile deformation. (c, and d) are dislocations present in the samples with a relative density of 27% and 50%, respectively.

2.4 Discussion and Conclusion

Using atomistic simulations, the response of nanoporous Au under uniaxial tensile loading has been shown to be strongly dependent on the fraction of the relative density of the sample. Nanoporous Au with 50% porosity behaves in a manner that is similar to the predictions of Gibson and Ashby for porosities of 50%, but there is a significant differ- ence between the predicted behavior according to the Gibson and Ashby model and the atomistic simulation results for higher levels of porosity. Both the elastic modulus and the yield strength of the foams were found to be significantly lower than the Gibson–Ashby predictions when the porosity is increased above the 50% level.

A possible reason for this discrepancy is changes in the network connectivity in nanoporous struc- tures with very high porosity levels. Reducing the solid fraction in a network while maintaining all ligaments and their connections would mean increasing the aspect ratio of the ligament. High porosity and small u requires ligaments with a high aspect ratio that can be easily lose their connectiv- ity. Therefore, the connectivity, n, is expected to decrease with u. The Gibson–Ashby predictions can be empirically corrected by replacing the relative density (u) with an apparent relative density (u_a),

as suggested by Liu et al[27]. This apparent relative density can be understood as the volume fraction of load-bearing ligaments. Our simulations suggest that, for our ligament size and for porosities greater than 50%, the ratio of the effective or apparent relative density to the actual relative density is about four times the square of the actual relative density (Eq. 2).

The u_a/u ratio has also been related to the connectivity, n, as follows [11,28]:

$$\xi = \left(\frac{\varphi_a}{\varphi}\right)^{\frac{3}{2}} \tag{7}$$

Using the ratios of u_a/u that explain our simulation results, we obtain:

$$\xi = (4\varphi^2)^{\frac{3}{2}} = 8\varphi^3 \; for \; \varphi < 0.5 \tag{8}$$

The value of the connectivity parameter, n, approaches 1 when the relative density approaches 50% or greater. This is a good description of the scaling observed in the present MD simulations.

It has to be pointed out that this is based on samples of only one ligament diameter, of 5.5 nm, and virtual tensile testing. It is possible that a different correction may be required for samples deformed in compression, and also in samples with different ligament sizes. In addition, the present model is based on samples created through the spinodal decomposition method. In addition, we have created only one sample for each relative density studied. Our samples contain a sufficiently large number of ligaments to give representative results, and these results can give a general indication of basic trends in the mechanical response of nanoporous Au.

It is interesting to compare the values of the ratio (u_a/u) in our model to those found experimentally by Liu et al [27]. They found that the effective relative density is around 0.07 for

a real relative density of 0.25, and an effective relative density of 0.15 for a real relative density of 0.33.

Using our model (Eq. 2), we would predict an apparent relative density of 0.08 for a real relative density of 0.25, and an effective relative density of 0.14 for a real relative density of 0.33. This is an excellent agreement even though the ligament sizes are different.

The deformation mechanism in all of our samples is through dislocations, but the distribution of dislocations in the samples clearly varies for different relative densities. The visualization of crystallographic defects for different porosity levels suggests that there is accumulation of partial dislocations and stacking faults in and around the nodes of the ligaments. The role of the ligament nodes can be important, as they can be preferential nucleation sites for dislocations. The nodes can also affect the surface to volume ratios of the samples. As pointed out earlier, our samples have a constant ligament diameter, but they are necessarily not self similar and the surface to volume ratios do vary. We have found values ranging from 0.82 nm to 0.52 nm for real relative densities ranging from 0.22 to 0.5, respectively. Despite these limitations, our results clearly support the idea that a correction to the relative density is necessary if the Gibson–Ashby formalism is to be used to predict values of the elastic modulus and yield strength for foams of relative densities lower than 50%.

2.5 Acknowledgements

This work was supported by the National Science Foundation, DMREF program under Grant No. DMR1533969.

2.6 Bibliography:

[1] J. Weissmüller, K. Sieradzki, Dealloyed nanoporous materials with interface-controlled behavior, MRS Bulletin 43(1) (2018) 14-19.
[2] A.M. Hodge, T. John Balk, Chapter 4 Mechanical Properties of Nanoporous Gold, Nanoporous Gold: From an Ancient Technology to a High-Tech Material, The Royal Society of Chemistry2012, pp. 51-68.
[3] J. Diao, K. Gall, M.L. Dunn, Yield Strength Asymmetry in Metal Nanowires, Nano Letters 4(10) (2004) 1863-1867.
[4] J. Biener, A.M. Hodge, A.V. Hamza, L.M. Hsiung, J.H. Satcher, Nanoporous Au: A high yield strength material, J. Appl. Phys. 97(2) (2005) 2-5.
[5] J. Biener, A.M. Hodge, J.R. Hayes, C.A. Volkert, L.A. Zepeda-Ruiz, A.V. Hamza, F.F. Abraham, Size Effects on the Mechanical Behavior of Nanoporous Au, Nano Letters 6(10) (2006) 2379-2382.
[6] J. Biener, G.W. Nyce, A.M. Hodge, M.M. Biener, A.V. Hamza, S.A. Maier, Nanoporous plasmonic metamaterials, Advanced Materials 20(6) (2008) 1211-1217.
[7] J. Erlebacher, M.J. Aziz, a. Karma, N. Dimitrov, K. Sieradzki, Evolution of nanoporosity in dealloying, Nature 410(6827) (2001) 450-453.
[8] J. Erlebacher, I. McCue, Geometric characterization of nanoporous metals, Acta Mater. 60(17) (2012) 6164-6174.

[9] L.J. Gibson, M.F. Ashby, The Mechanics of Three-Dimensional Cellular Materials, Proceedings of the Royal Society of London. Series A, Mathematical and Physical Sciences 382(1782) (1982) 43-59.
[10] L.J. Gibson, M.F. Ashby, Cellular Solids: Structure and Properties, 2 ed., Cambridge University Press, Cambridge, 1997.
[11] H.-J. Jin, J. Weissmüller, D. Farkas, Mechanical response of nanoporous metals: A story of size, surface stress, and severed struts, MRS Bulletin 43(1) (2018) 35-42.
[12] B.D. Ngô, B. Roschning, K. Albe, J. Weissmüller, J. Markmann, Scripta Materialia On the origin of the anomalous compliance of dealloying-derived nanoporous gold, Scr. Mater. 130 (2017) 74-77.
[13] D. Farkas, A. Caro, E. Bringa, D. Crowson, Mechanical response of nanoporous gold, Acta Mater. 61(9) (2013) 3249-3256.
[14] N. Mameka, J. Markmann, H.J. Jin, J. Weissmüller, Electrical stiffness modulation - Confirming the impact of surface excess elasticity on the mechanics of nanomaterials, Acta Mater. 76 (2014) 272-280.
[15] N. Mameka, J. Markmann, J. Weissmüller, On the impact of capillarity for strength at the nanoscale, Nature Communications 8(1) (2017) 1976.
[16] D. Crowson, D. Farkas, S. Corcoran, Surface Stress Effects on the Elastic Behavior of Nanoporous Metals, MRS Proceedings 900(1) (2005) 1-6.
[17] D.A. Crowson, D. Farkas, S.G. Corcoran, Mechanical stability of nanoporous metals with small ligament sizes, Scr. Mater. 61(5) (2009) 497-499.
[18] K. Kolluri, M.J. Demkowicz, Coarsening by network restructuring in model nanoporous gold, Acta Mater. 59(20) (2011) 7645-7653.
[19] A.C. To, S. Li, Perfectly matched multiscale simulations, Physical Review B 72(3) (2005) 035414.
[20] B.N.D. Ngô, A. Stukowski, N. Mameka, J. Markmann, K. Albe, J. Weissmüller, Anomalous compliance and early yielding of nanoporous gold, Acta Mater. 93 (2015) 144-155.
[21] J. Stuckner, K. Frei, I. McCue, M.J. Demkowicz, M. Murayama, AQUAMI: An open source Python package and GUI for the automatic quantitative analysis of morphologically complex multiphase materials, Comput. Mater. Sci. 139 (2017) 320-329.
[22] N. Badwe, X. Chen, K. Sieradzki, Mechanical properties of nanoporous gold in tension, Acta Mater. 129 (2017) 251-258.
[23] S. Plimpton, Fast Parallel Algorithms for Short-Range Molecular Dynamics, Journal of Computational Physics 117(1) (1995) 1-19.
[24] S.M. Foiles, M.I. Baskes, M.S. Daw, Embedded-atom-method functions for the fcc metals Cu, Ag, Au, Ni, Pd, Pt, and their alloys, Physical Review B 33(12) (1986) 7983-7991.
[25] A. Stukowski, K. Albe, Extracting dislocations and non-dislocation crystal defects from atomistic simulation data, Model. Simul. Mater. Sci. Eng. 18(8) (2010) 13.
[26] S. Alexander, A. Karsten, Dislocation detection algorithm for atomistic simulations, Model. Simul. Mater. Sci. Eng. 18(2) (2010) 025016.
[27] J. Li, Y. Chen, S. Xue, H. Wang, X. Zhang, Comparison of size dependent strengthening mechanisms in Ag/Fe and Ag/Ni multilayers, Acta Mater. 114 (2016) 154-163.
[28] E.T. Lilleodden, P.W. Voorhees, On the topological, morphological, and microstructural characterization of nanoporous metals, MRS Bulletin 43(1) (2018) 20-26.

Chapter 3: Deformation Mechanisms and Scaling Relations in the Mechanical Response of Nano-porous Au.

Nathan Beets, Diana Farkas, Sean Corcoran*

Department of Materials Science and Engineering, Virginia Tech
Holden Hall, 445 Old Turner St #213, Blacksburg, VA 24060

3.0 Abstract

We report a series of atomistic virtual mechanical tests on digitally created samples of nanoporous gold with 60% porosity, and average ligament diameters varying from 5.5 nm to 14.4 nm. Corresponding tests were also conducted for nanowires of equivalent surface to volume ratio and crystalline orientation. The validity of the Gibson-Ashby (G-A) scaling relations for the elastic and plastic behavior of the NP-Au structures is discussed. Tension/compression asymmetry in the plastic behavior was observed in both the nanoporous samples as well as the nanowires. Consistent with previous experimental and computational studies, the asymmetry becomes increasingly evident for the smaller ligament diameters, clearly pointing to capillary effects for large surface to volume ratios. Based on the present simulation results, a simple analytical model is presented for predicting the tension/compression asymmetry. The effects of internal ligament stresses on the deformation mechanisms and dislocation activity in the NP-Au structures are also discussed.

Keywords:
Nanoporous Gold, Atomistic Simulation, NanoMaterials, Capillary Phenomena.

3.1 Introduction

Nanoporous gold (NP-Au), an open cell structural material with pores and ligaments on the nanoscale has received widespread attention for its unique mechanical and chemical properties [19-31]. The structure of interconnected pores and ligaments allows for a high surface area to volume ratio which, when combined with the properties of gold nanowires can have applications in various fields [32, 33].

Experimentally, these structures can be created via an electrochemical dealloying process. Ligament size and fraction can be controlled in the nanometer range by the conditions of applied potential, dealloying time, electrolyte composition, and post processing treatments [29, 32-36].

The mechanical properties of NP-Au are not well understood. These structures have been shown to be very brittle in tension, but ductile in compression, separating them from the behavior of bulk polycrystalline Au [19, 20, 25, 26, 37-47]. Because samples often disintegrate under very small tensile loads, experimental testing is difficult. Predicting their behavior theoretically has been attempted using the Gibson-Ashby (G-A) scaling laws [23, 48-50]. If the strength of bulk polycrystalline Au is used, these scaling laws underestimate the strength of the NP-Au. This is generally attributed to the fact that nanowires are known to be stronger than bulk Au [19]. It is also not clear that the scaling laws are still valid for very small ligament diameters [51]. A recent

experimental study showed that a modification of the G-A formalism is necessary to get accurate Young's modulus predictions for nano structures, with ligament diameters below 100 nm [42].

The mechanical behavior of gold nanowires should help understand the scaling behavior of NP-Au samples, since these structures can be seen as an interconnected network of wires [48]. Nanowires have been observed to reach theoretical strength values at the nano-scale [52] through the "smaller is stronger" effect. This has been generally believed to be the reason why the G-A scaling relations fail if the properties of bulk Au are used when predicting the NP-Au behavior. The connection between deformation of nanowires and the deformation of NP-Au structures has been observed experimentally [53].

Simulations provide a unique opportunity to study the scaling relations accurately. They allow the investigation of deformation mechanisms of both nanowire samples and NP-Au samples for very small ligament sizes using identical crystalline orientations and interatomic force laws [23, 28, 37, 44, 54-57]. Large scale simulations can reach ligament sizes that overlap with those studied experimentally using standard molecular dynamics techniques. Samples with ligament sizes up to 20 nm can now be studied in practical computational times.

Another important contribution of simulations has been to predict a significant tension/compression asymmetry for very small ligament sizes [28, 43-48]. More recently, this asymmetry have been observed in experiments by Lührs et al, validating the trends predicted by simulations [47]. Based on simulations for a 2 nm ligament size, a model has been proposed for this asymmetry based on the effects of the large surface area to volume ratio in small diameter ligament NP-Au structures [28]. Current computational power allows simulations for larger ligament sizes and a better validation of the proposed model and further understanding of the tension/compression asymmetry.

The present work takes advantage of increased computational capabilities to quantify the effect of ligament diameter on the mechanical properties of NP-Au. Specifically, this dependence is explained in terms of the large surface area to volume ratios. We report atomistic simulations of NP-Au and corresponding Au nanowires with the same surface area to volume ratios under the same simulation conditions. We study the validity of the Gibson-Ashby scaling relations for these samples and present an improved model for the tension/compression asymmetry observed in both the NP-Au samples and nanowire samples.

3.2 Methods

Several methods have been developed and published to computationally generate bicontinuous NP-Au structures with porosity higher than 50% [58] [59] [60]. Crowson et al. [27] developed a strategy based on spinodal decomposition and utilized a phase field technique to solve the Cahn-Hillard equations. This technique creates two distinct phases, ligaments and pores, closely resembling the structure and ligament size distribution of experimental NP-Au obtained by dealloying [27, 61]. We used this method to generate the series of digital samples utilized in the present work.

Stability studies also conducted by Crowson [27] found that nanowires with ligament diameters smaller than 1.7 nm tend to collapse, due to capillary forces. Kolluri et al. [58] found that for ligaments in a lattice with average diameters between 1.5 and 2.1 nm, NP-Au digital samples collapse

without any applied stress. Given these results, in the present work, we created a series of samples with ligament diameters between 5.5 nm and 14.4 nm. These digital model structures were all generated with periodic boundaries in the X, Y, and Z directions [61]. All samples were self-similar and characterized by 60% porosity. We replicated the morphology, shown in Fig 1a, for different ligament diameters so that all samples were morphologically identical, with only the ligament size being varied. All the samples were cubic in shape and had identical crystallographic orientations, with the three <100> type directions oriented along the axes of the cube.

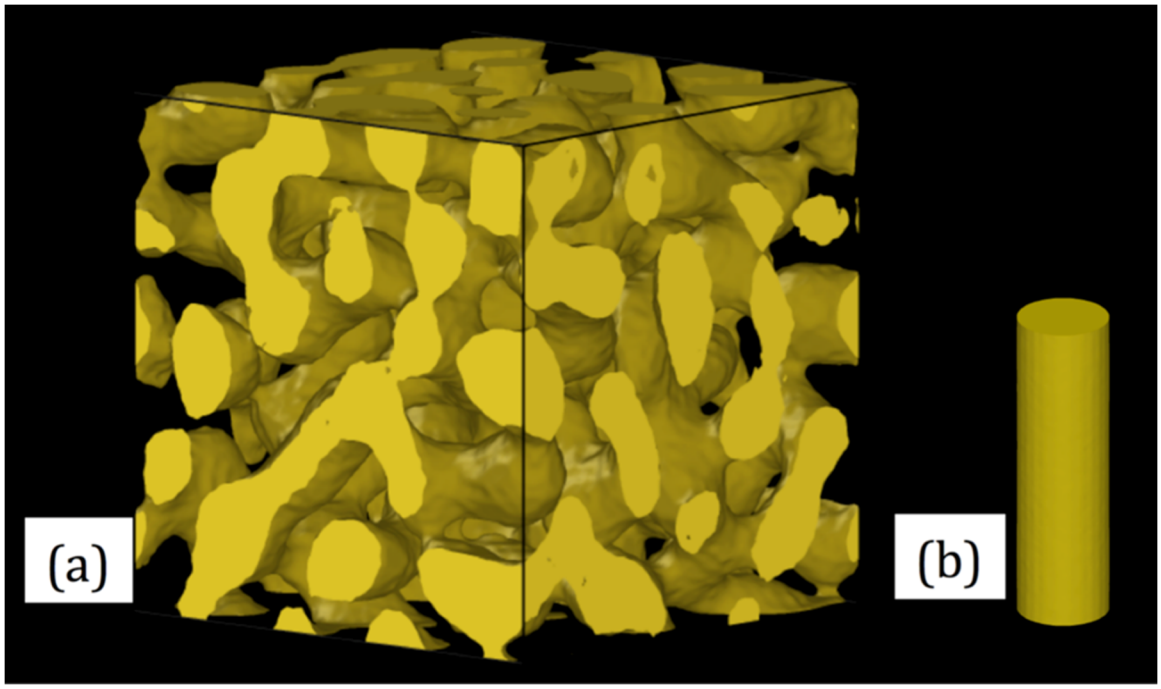

Figure 3-1: Sample morphologies for the NP-Au (a) and nanowire (b) samples. The samples as shown in (a) and (b) have the same surface area to volume ratio.

Relaxation and deformation were performed using the LAMMPS molecular dynamics implementation and EAM interatomic potential functions for Au developed by Set al. [7, 62]. Though these interatomic potential functions have been used extensively, they are adequate to investigate the trends in yield as affected by ligament diameter, as well as the validity of the Gibson-Ashby scaling relations. The AQUAMI code developed by Stuckner [63] was used to determine the average ligament diameter of our samples as 5.5, 6.9, 10, 11.9, and 14.4 nm respectively, and the pore fraction for all samples after relaxation was 60% pore 40% solid. Figure 2 shows the distribution for the 6.9 nm samples and a corresponding Gaussian profile for comparison.

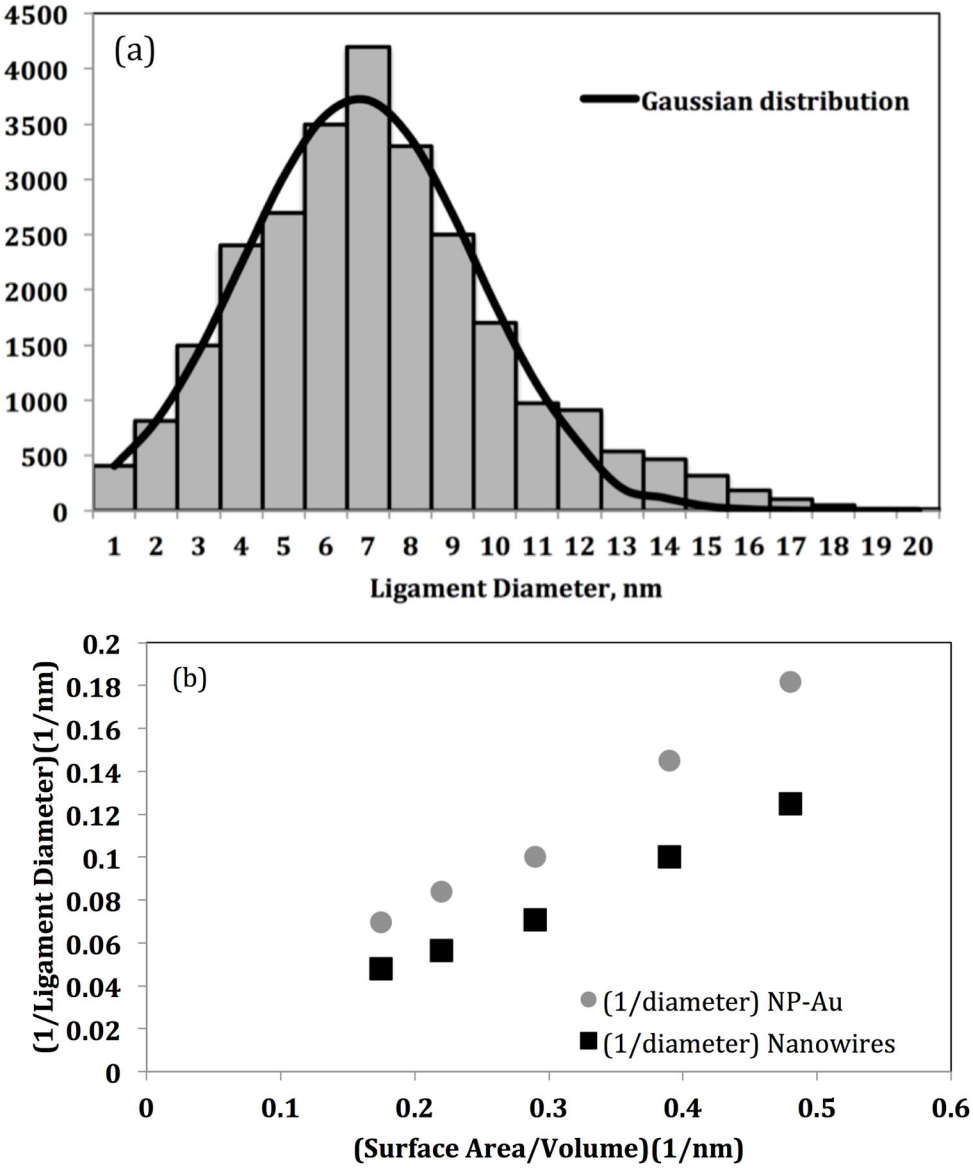

Figure 3-2: (a) Ligament size distribution for the 6.9 nm ligament diameter NP-Au sample. The distribution shape is the same for all ligament sizes studied. (b) The relationship between surface area to volume ratio to ligament diameter for our NP-Au samples.

Each sample was relaxed and deformed using a Noose-Hoover thermostat and barostat, and equilibrated at 300 K for approximately 2 ns. After equilibration, each sample was deformed in tension and compression at a rate of $(3x10^8)$ s^{-1} up to 10% strain. The deformation was strain-controlled with the stress and energy levels of all atoms on the interior and surfaces monitored as the deformation proceeds. Selected snapshots were obtained by quenching to 10 K in 10 ps in order to eliminate thermal vibrations and study the local distribution of stresses. Visualization of defects was performed using OVITO [16]. This included the analysis of dislocations by the DXA dislocation extraction formalism and analysis of volume and surface area relationships via the surface mesh formalism [64].

In addition to the NP-Au samples, we created a series of solid cylindrical gold nanowires oriented with the nanowire axis along the <100> direction, as shown in Fig 1b. The nanowires were subjected to corresponding relaxation, tension and compression tests that were identical to those performed on the NP-Au samples. These provided information on the stress states, dislocation nucleation behavior, and yield/flow stress trends, which were used for comparison with the results from the NP-Au samples.

For studying the validity of the G-A scaling relations, the nanowires were constructed to have identical surface area to volume ratios as the NP-Au. Importantly, this meant that they did not have exactly the same ligament diameters. This is expected to provide a more accurate test of the scaling relations due to the critical role of capillary forces controlled by the surface to volume ratio [65]. While the ratio can be stated as 4/d for cylinders of diameter d, and 6/d for spherical voids of the same diameter, the complex morphology of nonporous solids will result in a different ratio for the same ligament diameter. Figure 2b shows the relation between ligament diameter and surface-area-to-volume ratio for each of the NP-Au samples generated.

3.3 Results:

3.3.1: Sample Structure

Fig. 1a shows the morphology of our digital self-similar NP-Au samples. Using the surface mesh tool in OVITO, the solid volume fraction of our samples is 0.4 , that is 60% porosity [16]. In order to study the ligament size distribution, 10 different 5 nm thick slices were taken through each sample, and the ligament size distribution in the samples was measured using the AQUAMI algorithm [63]. The average was then taken of the mean and standard deviations for all slices, with the results shown in Fig. 2a. Since a common morphology was used for all ligament diameters, and was simply rescaled to match the desired mean ligament diameter value, this distribution had an identical shape in all our NP-Au samples. The distribution is close to a normal with a standard deviation that is 42% of the average ligament size. This compares well with recent experimental measurements of dealloyed samples [19].

The surface-area-to-volume ratios of the samples were obtained as a function of the ligament diameter (Figure 2b). As expected for self-similar samples, these results follow a linear behavior, that can be represented as $S/V = 2.56/d$. This is in contrast to the ratio for nanowires which is $S/V = 4/d$. This means that for the nanowire samples to match the surface to volume ratios of the NP-Au samples, their diameter had to be about 50% larger than the ligament diameter of the corresponding NP-Au.

We analyzed the per-atom stress state of individual atoms both in the NP-Au samples as well as the nanowires. In order to calculate the internal and external per atom hydrostatic stress tensor, we added the diagonal components of the computed stress tensor for each atom. The computation of the stress tensor components requires an assumption for the atomic volume of each atom. We used the perfect lattice atomic volume of 0.0169 nm^3, which is a reasonable approximation for the atoms inside the ligaments. This assumption tends to overestimate the stress for the surface atoms, leading us to assume that the true surface atom volumes are closer to twice this value, on average. The stress analysis in this paper primarily focuses on stress distribution on ligament interiors and total sample

values, which do not require accurate surface volume measurements, so it is not an issue here. An image of the 5.5 nm sample and the 14.4 nm sample with individual atoms colored by atomic hydrostatic stress value is shown in Fig. 3(a) and 3(b), respectively. The results for the average stress of the atoms inside the ligaments and nanowires as a function of the surface area to volume ratio are plotted Fig. 4.

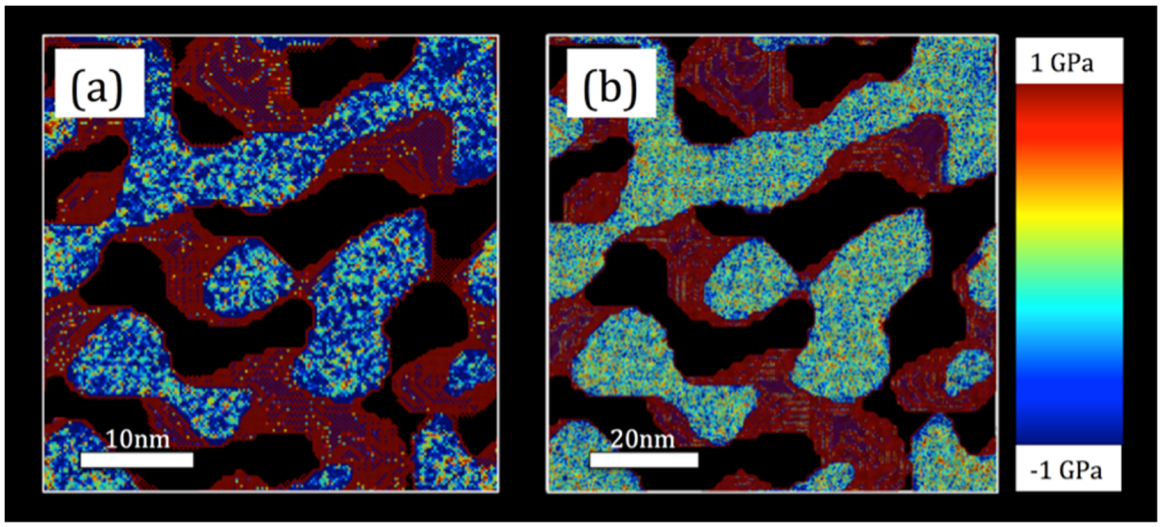

Figure 3-3: Comparison of stress states on atoms in the NP-Au gold samples. (a) is the 5.5 nm ligament sample, while (b) is the 11.9 nm ligament sample. (COLOR ONLINE)

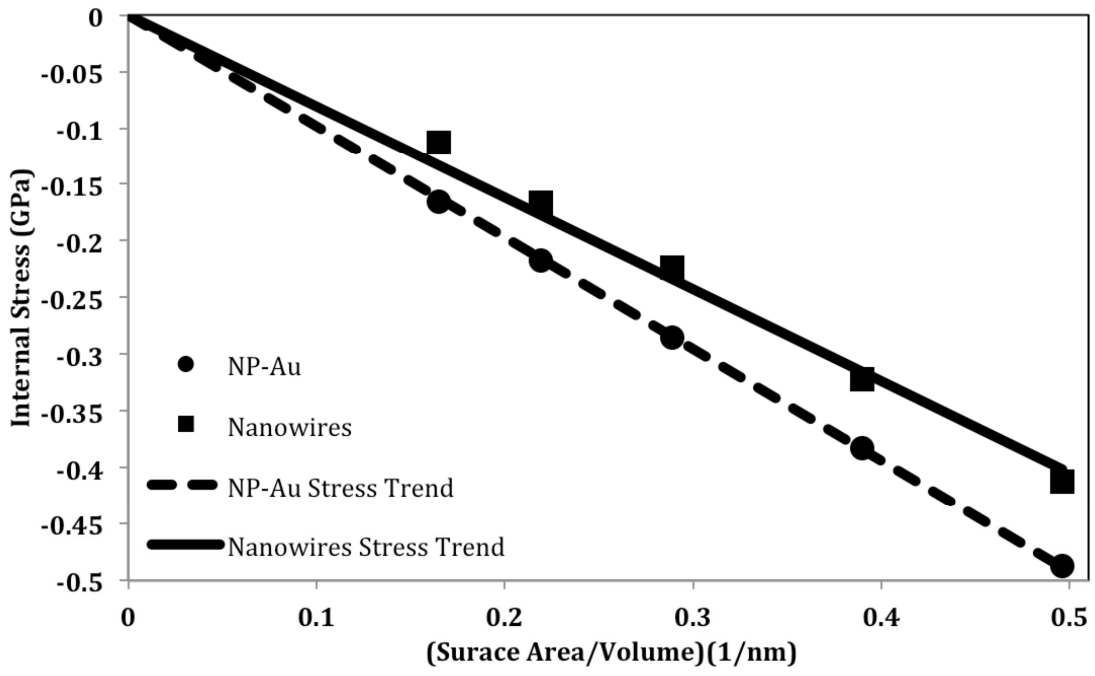

Figure 3-4: Average hydrostatic stress of the atoms inside the ligaments/nanowires as a function of the surface area to volume ratio of the samples. The stress is calculated as the trace of the stress tensor matrix, and the atoms are separated by structure type, using the common neighbor analysis modifier in OVITO.

The stresses observed inside the ligaments in the NP-Au samples are very similar to those observed in the nanowires of the same surface area to volume ratio, and exhibit a linear trend, as predicted by the general capillary force law, wherein ΔP is the compressive stress [65, 66].

$$\Delta P = \left(\frac{2}{3}\right) f \left(\frac{S}{V}\right) \quad (1)$$

This linear trend allows us to calculate the values of the surface stress *f*. We obtain 1.48 and 1.21 J/m^2 for the NP-Au and nanowire samples, respectively. These values compare well with the values computed for surface stress from the interatomic potential which are between 1.28 and 1.32 for low index surface orientations [7].

A tensile stress on the surface atoms of the nanowires and NP-Au samples balances the compressive internal stress, given by equation 1 [67], [44]. This tensile stress of the surface atoms was found to be largely independent of the ligament/nanowire diameter, being relatively constant for all samples observed. Using the atomic volume of the perfect lattice we obtain an upper bound to the value of the tensile stresses in the surface atoms of about 6 GPa. An alternative estimate can be obtained from calculating the number of surface atoms compared to the number of internal atoms, and computing the average surface atom tensile stress necessary to balance the compressive internal stress. This method gives an estimate of around 2.9 GPa for the average tensile stress of the surface atoms. The discrepancy between these two estimates is possibly due to the fact that the actual atomic volumes of surface atoms can be larger than those of the atoms in the perfect lattice, as mentioned previously.

3.3.2 Virtual Tensile and Compressive Tests

We performed strain controlled deformation experiments, allowing for Poisson contraction in an NPT (isothermal-isobaric) ensemble, maintaining periodicity and zero applied stress in the directions perpendicular to the axial deformation. For the nanowires, the zero applied stress condition in the directions perpendicular to the deformation axis defines the free surface, which allows for the aforementioned Poisson contraction. Both tension and compression were simulated up to 10% strain in both the NP-Au structures and the corresponding nanowires for the five ligament sizes. The resulting stress/strain curves are shown in Fig. 5. Notice here the trend of the ligament diameter vs. stress for tension vs. compression, shown by the arrow inset.

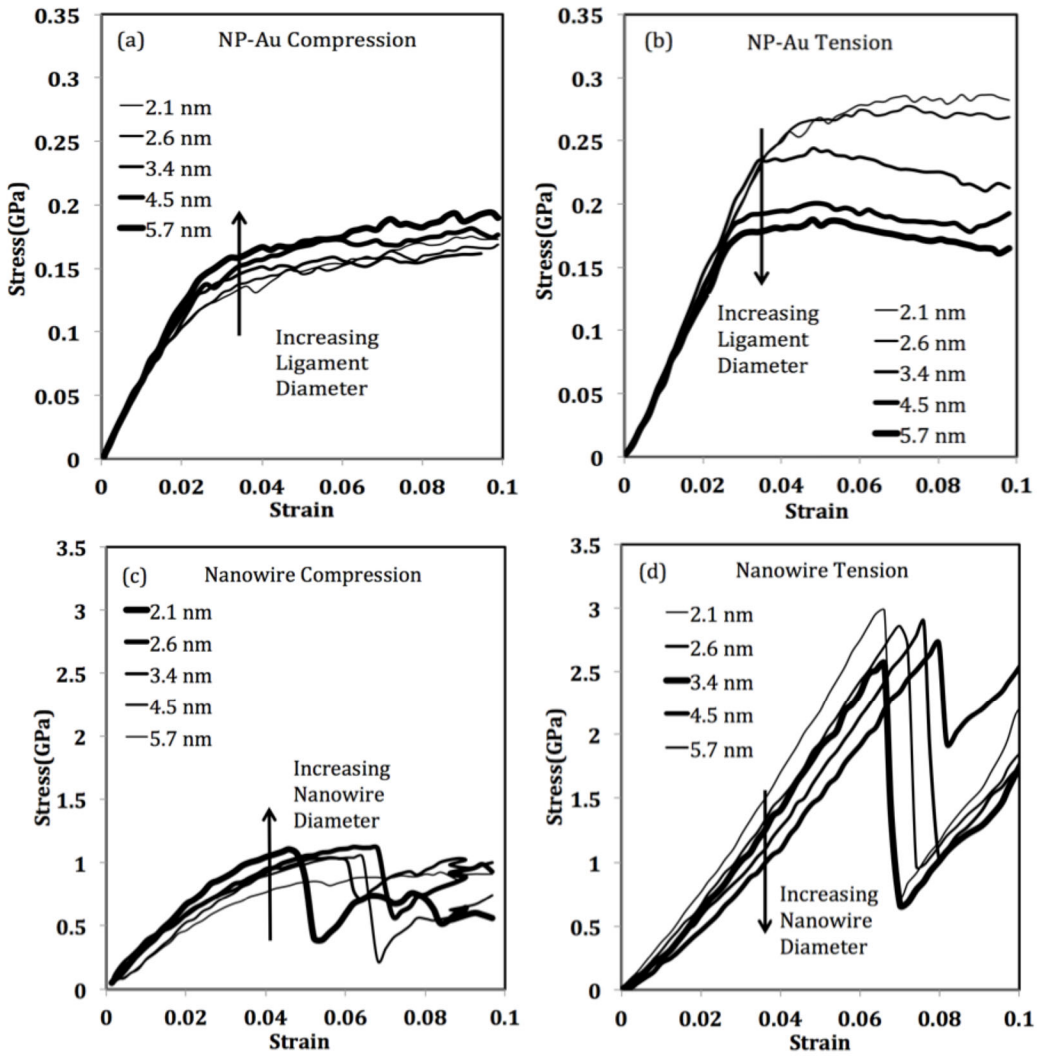

Figure 3-5. Stress-strain curves for all samples, with graph line thickness increasing with increasing (Volume/Surface Area) (nm) (a) NP-Au samples in compression (b) NP-Au samples in tension, (c) Nanowire samples in compression and (d) Nanowire samples in tension.

For both cylindrical nanowire samples and the NP-Au samples, a significant tension/compression asymmetry is observed in the plastic regime. It is interesting to note that the effect of asymmetry for smaller ligament sizes can balance the well known "smaller is stronger" effect in compression.

The elastic moduli of the samples were obtained from the initial stage of the deformation, up to 1% strain. The results are shown in Fig. 6, including moduli calculated both in compression and in tension. The elastic modulus of a single crystalline sample is included for reference for both the NP-Au and Nanowires.

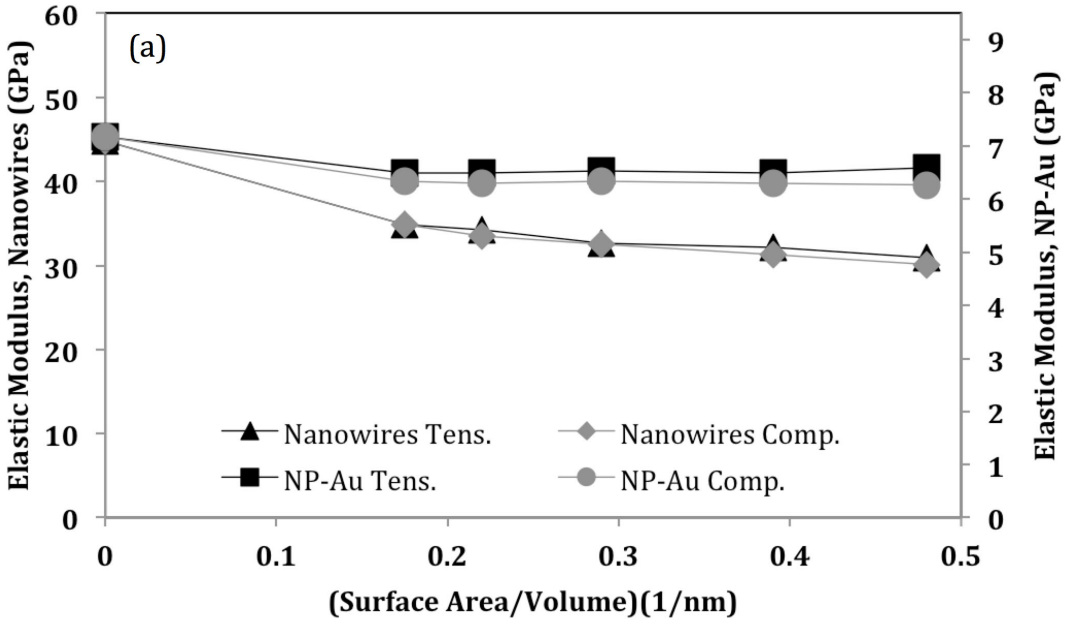

Figure 3-6: Elastic Moduli for all samples.

The elastic modulus results obtained for the nanowires are significantly lower than the 79 GPa typical for bulk polycrystalline gold. The reason for this difference is that the nanowires are oriented in the [100] direction and our results should be compared with the elastic modulus predicted for that specific orientation. This can be calculated from the compliances in the [100] direction, as follows [68]:

$$s_{12} = -\frac{c_{12}}{(c_{11}-c_{12})(c_{11}+c_{12})} \tag{2}$$

$$s_{12} = \frac{(c_{11}+c_{12})}{(c_{11}-c_{12})(c_{11}+c_{12})} \tag{3}$$

from which we can calculate the directional [100] elastic modulus,

$$\widetilde{E} = -\frac{s_{11}}{s_{11}^2-s_{12}^2} \tag{4}$$

Using the values of c_{11} and c_{12} specific for this potential [7] we find that the elastic modulus for the <100> direction to be 44.85 GPa. For confirmation, we tested a bulk cubic periodic sample of 46000 atoms with no free surfaces and a <100> orientation. This test yielded an elastic modulus of 44.13 GPa in compression, and 45.37 GPa in tension, in very good agreement with the calculated value of 44.85 GPa.

The elastic moduli obtained for the nanowire samples indeed approach this value, particularly for the larger ligament diameters. The differences observed for the smaller ligament diameters can be attributed to the effects of the surface [69].

3.3.3 Onset of plasticity

The yield stress values were obtained, using the 0.2% offset criterion for the NP-Au samples and defect nucleation in the nanowire samples. The results are shown in Figs. 7a-b. Both show a strong tension/compression asymmetry in the onset of plasticity, which is more significant for the smaller ligament/nanowire diameters.

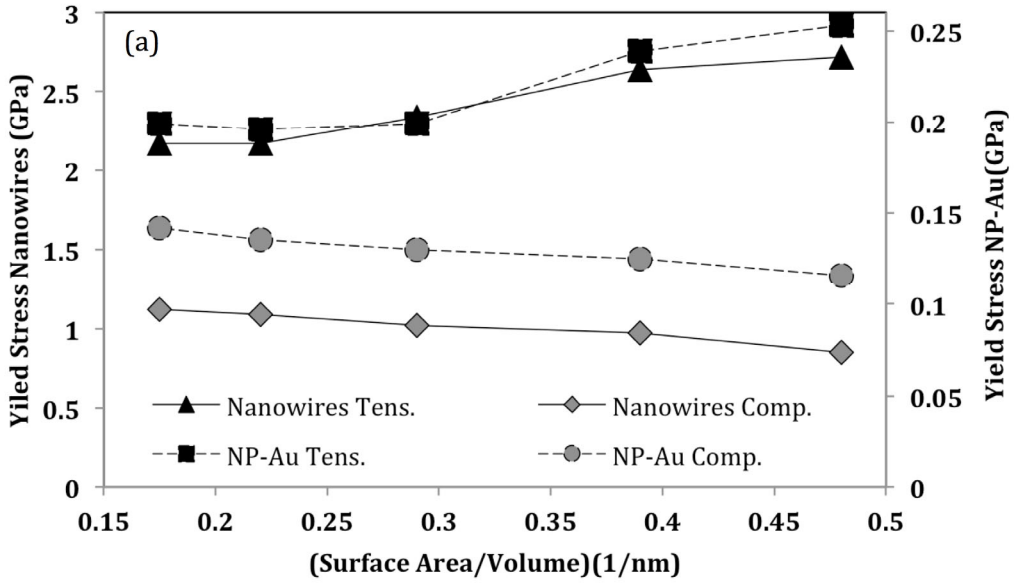

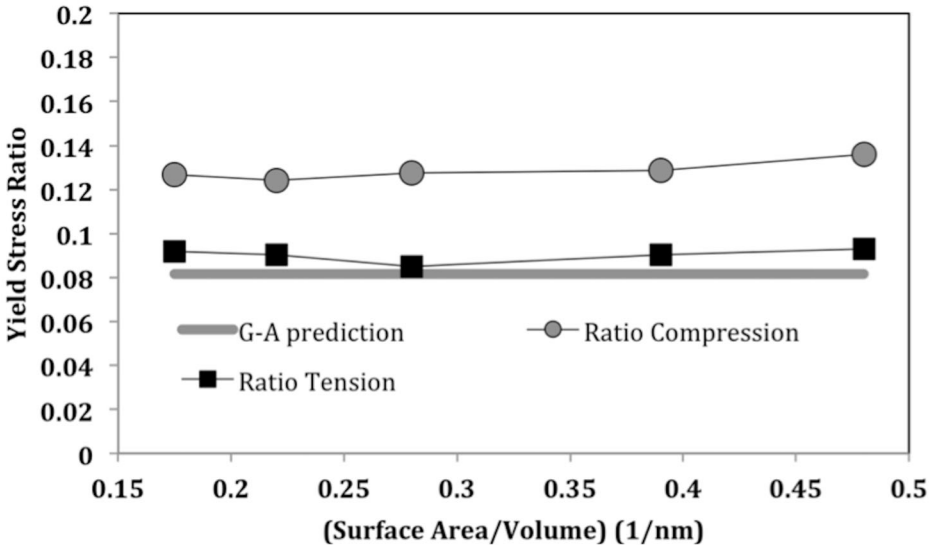

Figure 3-7: (a) Yield stress for all samples (b) Yield stress ratios of the NP-Au samples over the corresponding nanowires, and how they compare with the Gibson-Ashby prediction.

The Gibson-Ashby scaling relation for yield stress is:

$$\sigma = C_1 \sigma_s \left(\frac{\rho}{\rho_s}\right)^n \tag{6}$$

where σ_s is the yield stress for the solid, obtained from the nanowire deformation tests, (ρ/ρ_s) is the volume fraction of solid, n is (3/2), and C_1 is a constant expected to be about 0.3[48]. This predicts a ratio of the yield stress of the NP-Au to the nanowires of about 0.08. We observe ratios of about 0.1. Fig. 7b compares the ratios observed with the Gibson-Ashby predictions in tension and in compression.

3.3.4 Model for the Tension/Compression Asymmetry

The tension/compression asymmetry observed in the yield stress of our NP-Au samples and nanowires of small diameters is quite significant. This is believed to be due to the effects of the large surface area to volume ratios for small diameters and can be related to the observations of the stress states of the individual atoms at the surface and inside the ligaments.

This surface-induced internal stress, reported in Fig. 4 constitutes a possible explanation for the tension-compression asymmetry. During deformation, when there is an applied load, the additional stress is superimposed on the already existing compressive stress in the ligaments. Therefore a lower external load is required for yielding under compression than under tension, with the difference increasing for large surface area to volume ratios. Another reasoning can be based on energy arguments, since the plastic tensile elongation of a ligament increases its net external surface area A, while compression reduces A. This net energy change is also more significant for large surface area to volume ratios and favors plasticity under compression as opposed to tension [51]. In both cases, the effect of the free surface is to add a term to the yield stress that is directly proportional to the ligament/nanowire surface area to volume ratio. This surface-dependent term is positive for the case

of tension and negative for the case of compression.

In our previous work an expression was proposed for the yield stress that included such a term dependent on the inverse of the ligament diameter. In that work, only one ligament diameter was tested so the model could not be verified for a range of ligament diameters. Here, we propose a similar model to account for the present observations for ligament diameters from 5.5 to 14.4 nm. This is given below:

$$\sigma_y(d) = \sigma_0(d) + \sigma_{surf}(d) \tag{7a}$$

Where, σ_0 (d) is a term that is independent of the surface contribution. This term can be still size-dependent through the "smaller is stronger" effect. The term σ_0 (d) is expected to follow a dependence of $d^{-1/2}$ until it reaches a value of several GPa, close to the theoretical strength of the material. For the ligament sizes in the NP-Au we are considering, it can be assumed to be a constant.

The second term is a surface dependent term that varies as a function of the surface-area-to-volume ratio with a sign that is dependent on whether the sample is being deformed in compression or tension:

$$\sigma_s \begin{cases} -\frac{2Sf}{3V} & \text{(compression)} \\ \frac{2Sf}{3V} & \text{(tension)} \end{cases} \tag{7b}$$

In terms of the ligament or nanowire diameter this is:

$$\sigma_s \begin{cases} -\frac{\beta f}{d} & \text{(compression)} \\ \frac{\beta f}{d} & \text{(tension)} \end{cases} \tag{7c}$$

The factor ((2/3)(S/V)) is derived from the generalized surface treatment by J.W. Gibbs in his 1928 collected works [65].

Here, β is a geometrical factor, and f is the surface term. For cylindrical nanowires β = 8/3, whereas for our NP-Au samples we find β =1.7, based on our results for the surface area to volume ratio. From our calculations, this term seems consistent with the surface stress (see table 2). Others have argued that the surface energy alone may be the main contributor, and have provided compelling arguments to this claim [70]. The issue can be addressed by varying the surface stress independently from the surface energy through modifications of the EAM potentials. This will be the focus of future work.

Because the surface term is of equal magnitude and opposite sign for tension and compression, the term σ_0(d) can be obtained simply from averaging the values of the yield strength in tension and in compression.

A least squares fitting algorithm was used to find the best-fit value for the terms in eq. 7. The performance of the model is shown in Figs. 8a and b for the NP-Au and nanowires, respectively. The fitting parameter values obtained are shown in Table 1. The comparison of the model and the

simulation results shown in Fig. 8 indicates that the model captures the essential features of our observations. For the nanoporous samples, the value of the surface-independent term was found to be the same under tension and under compression. For the nanowires, the values of this term under compression were slightly lower than those in tension, discussed in greater detail in the discussion section. The ratios of the model parameters for NP-Au to nanowires observed in the model parameters are around 0.1, of the same order as the Gibson-Ashby ratio expected for the NP-Au structures, which is around 0.08.

Figure 8c shows the tension-compression asymmetry ratios observed as a function of the ligament size. For both types of samples, the ratios are significant for the small sizes and decrease as the sizes increase, as expected, and consistent with previous work [28].

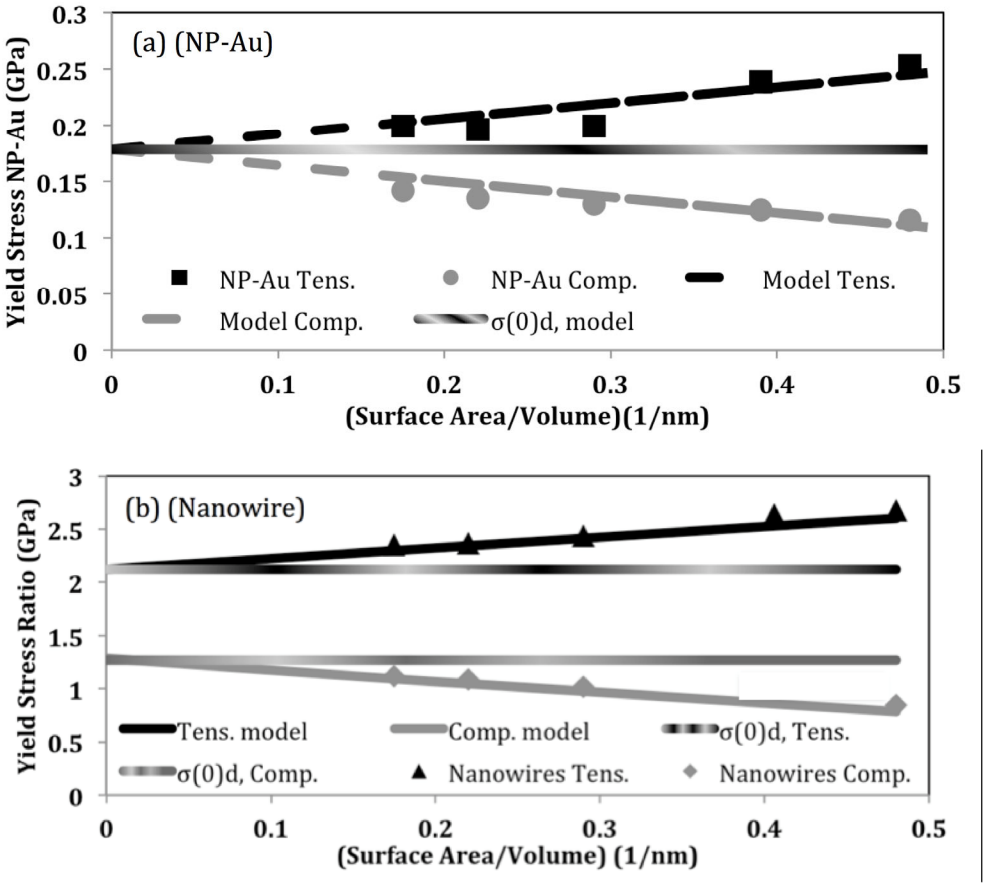

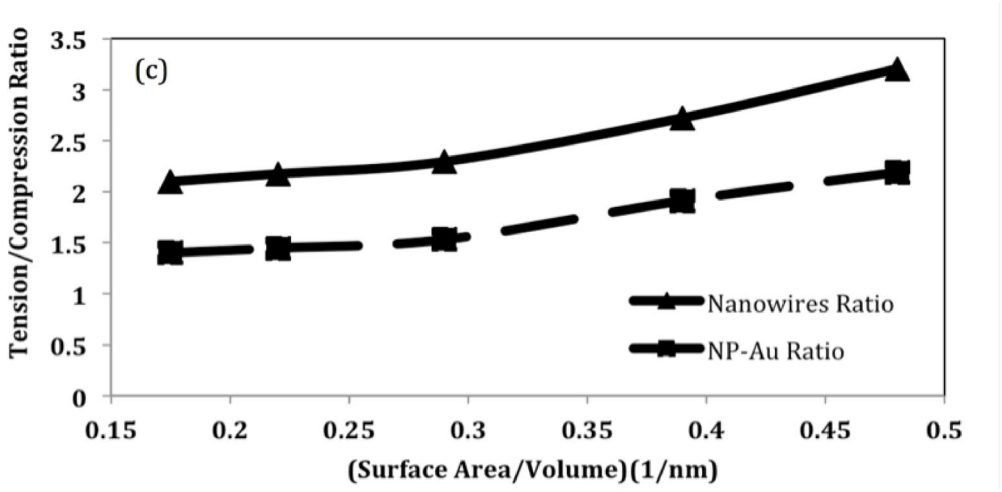

Figure 3-8: Analytical model for the observed yield stresses. (a) NP-Au samples yield stress data and model, (b) nanowire yield stress data and model, and (c) tension/compression asymmetry ratios.

Table3-2: Fitting Parameters of the Model Describing the Observed Yield Behavior

	Scaled with Gibson-Ashby relation
f, Nanoporous (J/m^2) (G-A scaled)	2.04
f, Nanowires (J/m^2)	1.51
σy_0, Nanoporous (GPa) (G-A scaled)	1.734
σy0, Nanowires, Tens. (GPa)	2.121
σy0, Nanowires, Comp. (GPa)	1.267

Table 3-2: Calculated Values for Surface Stress and Energy, respectively.

	Values in J/m^2
Surface term from internal stress in np sample	1.48

Surface term from internal stress in nanowires	1.21
Surface term from np model and G-A scaling	2.04
Surface term from nanowire model	1.51
Foiles potential (100) surface energy	0.918
Foiles potential (110) surface energy	0.980
Foiles potential (111) surface energy	0.790
Foiles potential (100) surface stress	1.279
Foiles potential (110) surface stress	1.324
Foiles potential (111) surface stress	1.313

3.3.5 Deformation mechanisms.

The basic deformation mechanism for the NP-Au structures was found to be dislocation activity. Figure 9 shows the dislocations found in the samples after 10% deformation in both compression and tension. For both tension and compression, the mechanism is the same. The dislocations are mostly Shockley partial dislocations that originate at the surfaces of the ligaments. As these dislocations move within the ligaments they generate stacking faults that are also seen in Figure 9.

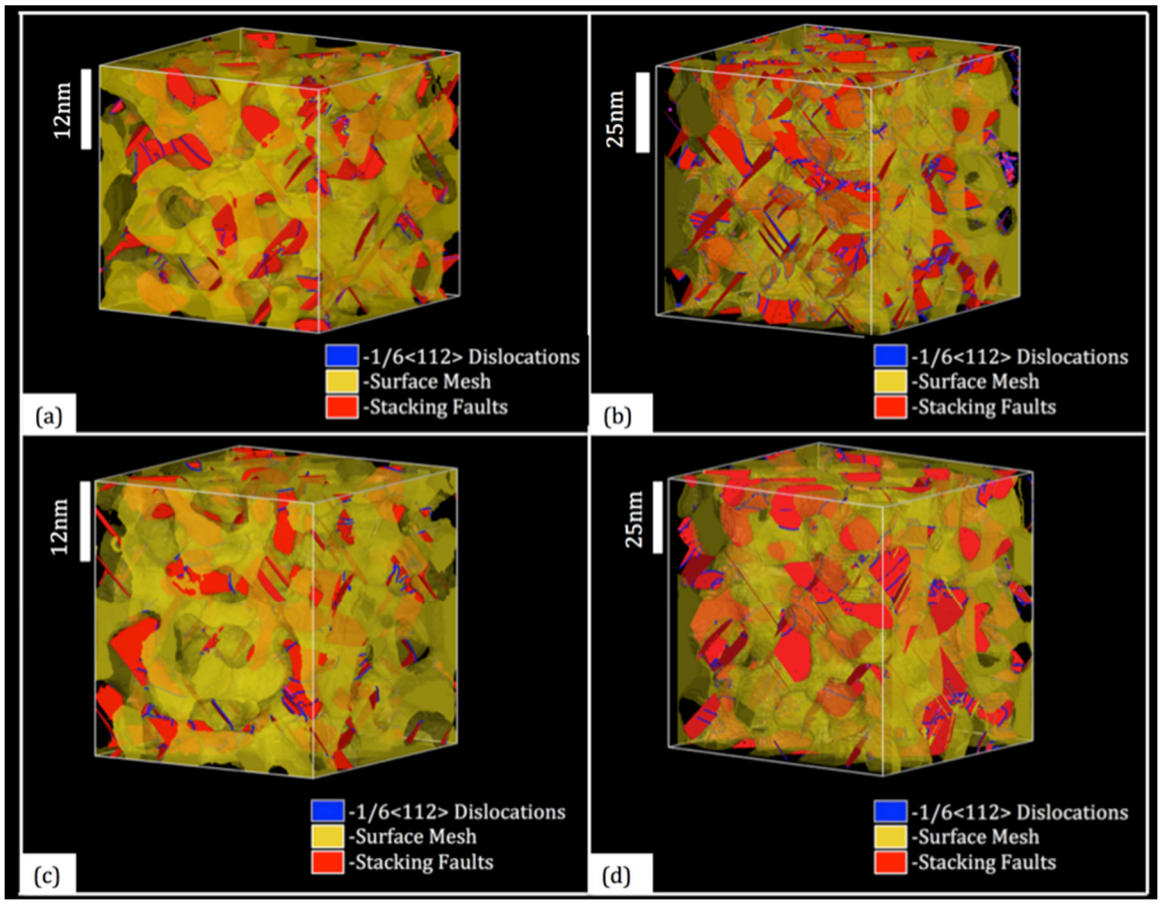

Figure 3-9: A visual representation of dislocation motion and stacking fault formation in compression and tension for the 5.5 nm ligament diameter NP-Au lattice ((a) and (c)), and the 11.9 nm ligament diameter NP-Au lattice ((b) and (d)). (COLOR ONLINE)

Residual dislocation densities for both tensile and compressive NP-Au samples were analyzed as a function of the ligament diameter. The results in Fig. 10 show the evolution of dislocation density as the strain is increased. Dislocation onset started earlier for the compressive samples than for the tensile samples, and the dislocation densities were larger in the samples under compression.

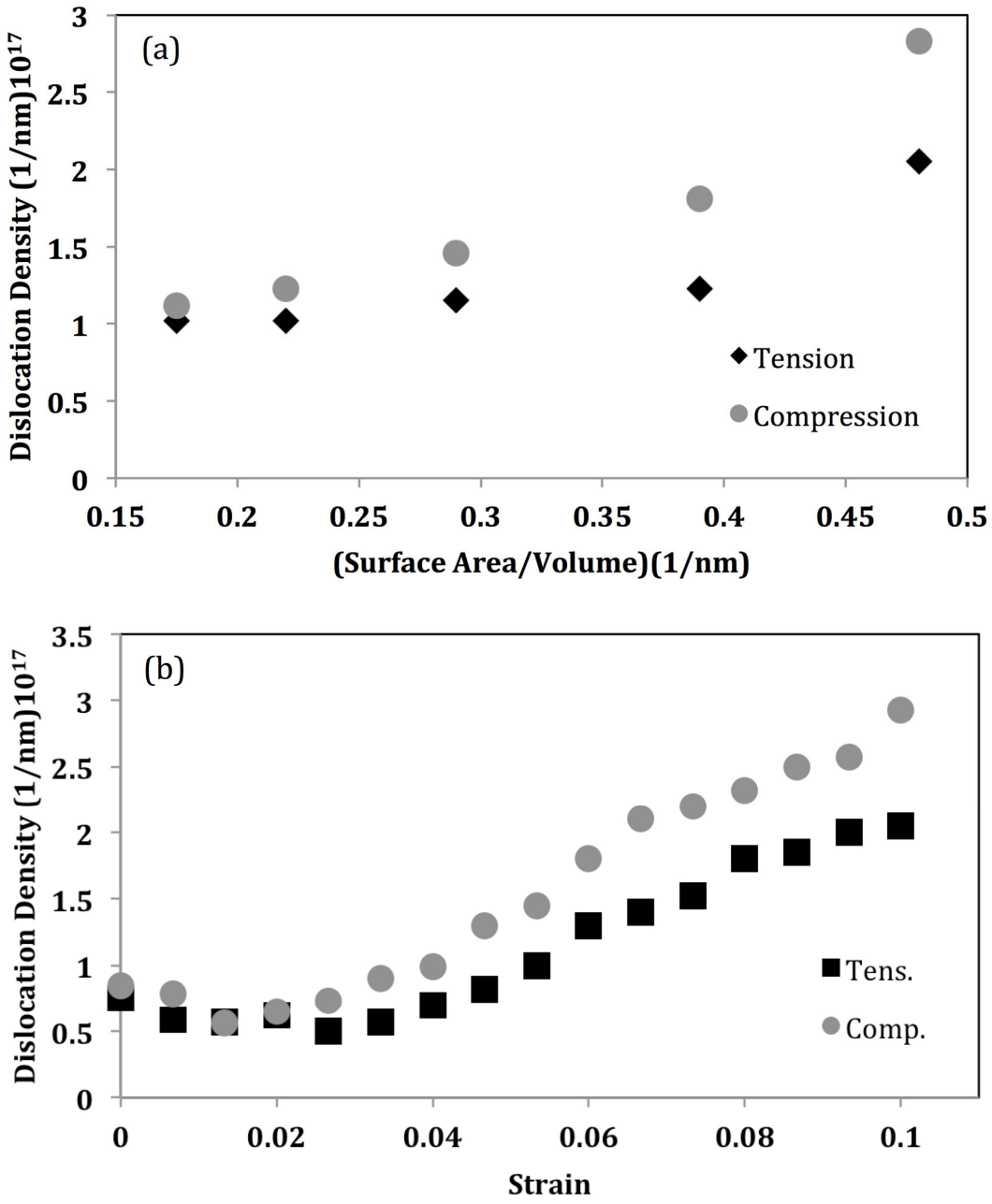

Figure 3-10: (a) Dislocation density as a function of ligament diameter at 10% strain for the 5.5nm sample. (b) Evolution of dislocation densities as a function of strain for a 5.5 nm ligament diameter NP-Au sample.

We also observed that dislocations nucleate at the surface of nanowires, as in previous work [71]. For the nanowires under tension, the deformation mechanism observed was very similar to that in the nanoporous ligaments, namely Shockley partials nucleating from the surface. For the nanowires under compression, twinning was observed as the primary deformation mechanism. This difference may explain why in the case of the nanowires when fitting our proposed model (eq. 7b) 2 separate values resulted for $\sigma_0(d)$ while only one was fit for the NP-Au samples. For both cases, there was only one value for $\sigma_{surf}(d)$, with different signs for tension and compression.

Recently Li and co-workers performed a systematic atomistic study of the energy barriers for surface dislocation nucleation in nanowires [69]. They demonstrated in detail how surface phenomena influence dislocation nucleation. They showed that the strength dependence on sample size is a result of the combined effects of the surface stress and the applied axial stress. Most importantly, they found that the surface effects are of opposite sign, depending on whether the applied stress is tensile or compressive. This is consistent with the basic assumption of our model above, namely the fact that the surface can have weakening or strengthening effects for compressive or tensile loading, respectively. Furthermore, they studied the local critical resolved stresses for dislocation nucleation as a function of nanowire size and found an inverse dependence on the nanowire diameter. This is also consistent with the model that we propose here to explain the tension/compression asymmetry observed in our samples.

We have shown that the atoms in the outermost surface layers are under tension. If this tensile stress affects nucleation, the opposite sign of the assymetry could be expected, yielding strengthening in compression and weakening in tension. This is contrary to what is observed. It is therefore critical to understand how the local stress state of atoms at and near the surface actually influence dislocation nucleation. For the outermost layer, we have found a tensile stress of several GPa, with no significant variation as a function of ligament size. The internal stress, on the other hand, which is depicted in Fig. 4, is dependent on ligament size, with a linear relationship with surface area to volume ratio. We specifically visualized the local stress in areas where dislocation nucleation was occurring, and analyzed the stress distribution prior to and after nucleation. An example of this analysis is shown in Fig. 11 for the sample with an 11.9 nm ligament diameter. The top row shows the stress map, where regions of high compressive stress tend to occur where ligaments are thinner, and regions of lower compressive stress occur when ligaments are thicker, consistent with the data and relation presented in Fig. 3. We see that dislocations prefer to nucleate in regions of high negative curvature, where regions high in compression in the interior tend to form, adjacent to the exterior atoms that are in a tensile state. This is shown in the center row of Fig. 11, where the stacking faults are visualized, indicating where Shockley partial dislocations nucleated. The arrangement of regions with higher interior Von Mises Stress seems to be critical in nucleating dislocations from the surface, inducing regions of local shear stress, optimal for the formation of Shockley partial dislocations. Dislocations in many cases nucleate from a point in the node or ligament with negative curvature, often corresponding to a point where the high internal Von Mises stress sits near the surface layer, also in a high state of stress.

The bottom row of Fig. 11 is a displacement map, indicating dislocation activity that includes both partial and full dislocations. In this visualization, we can also see the preference for dislocation activity starting from the regions of negative curvature. There is clearly more dislocation activity under compression than under tension, consistent with the fact that dislocation nucleation and the corresponding plastic deformation is easier under compression than under tension.

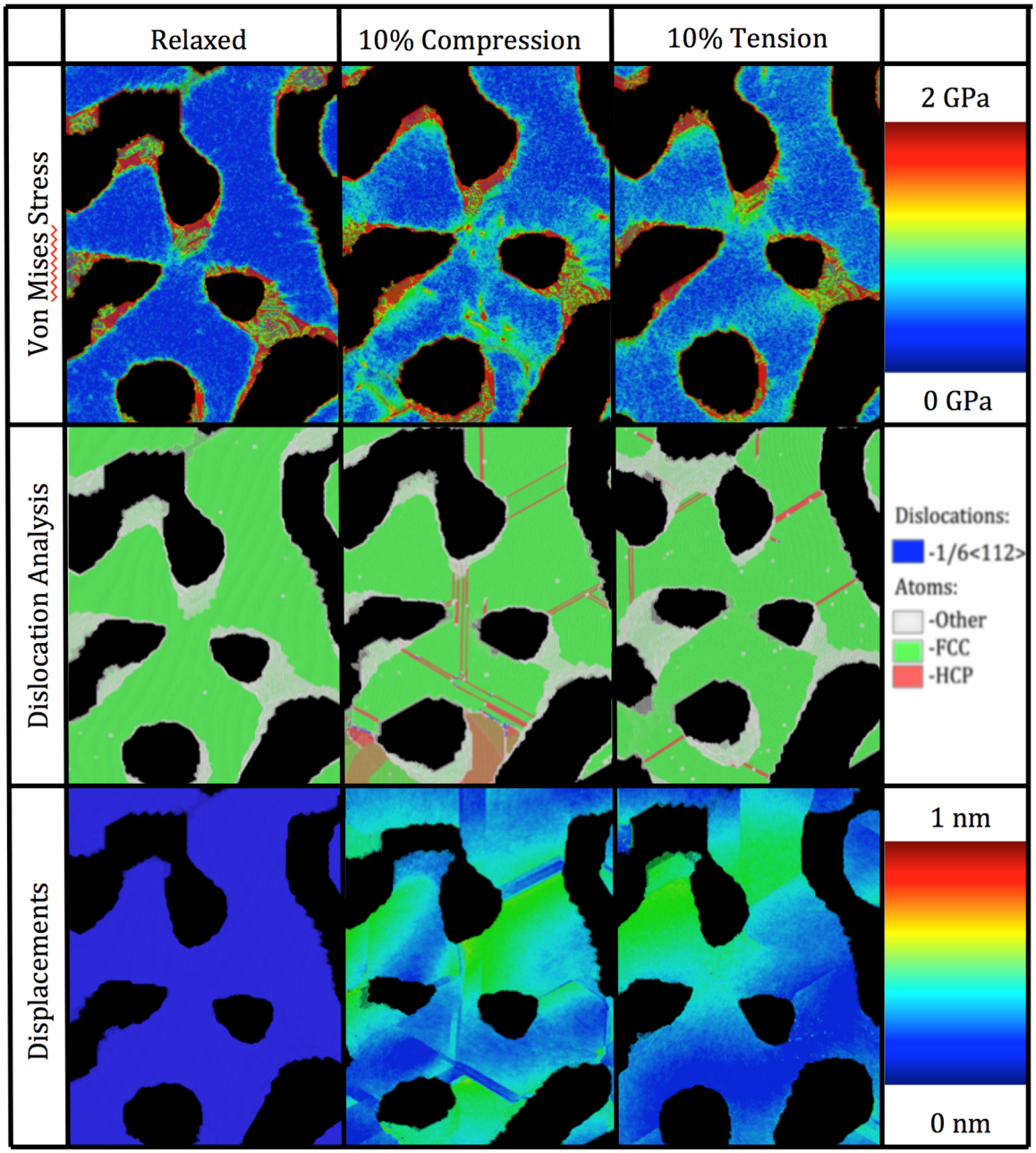

Figure 3-11: Stress state and dislocation activity in one ligament in the NP-Au sample with 11.9 nm ligament diameter. The top row is the visualization of individual atom stresses. The center row (centrosymmetry parameter) shows the stacking faults created as shockley partial dislocations travel across the ligament. The bottom row is the visualization of the atomic displacements showing plastic deformation.

3.4 Discussion

Experimental studies involving nanoindentation report average hardness values of around 150 MPa for NP-Au structures with ligament diameters between 10 nm and 100 nm [72-74]. Here we report values of the yield stresses from simulations that are of similar order of magnitude, indicating that the present atomistic simulations can indeed capture the basic characteristics of the deformation

process of NP-Au structures. We have utilized the simulations to check the validity of the G-A scaling relations for nano-sized NP-Au structures. The check was conducted by comparison with nanowires that have the same surface to volume ratios as the NP-Au structures, so that the nano-size and surface effects are similar in the solid wires and in the ligaments of the NP-Au structures. The results that we obtained for the NP-Au samples compare generally well with the Gibson-Ashby scaling predictions based on our corresponding nanowire results. The deviations that we observe from the G-A predictions are within 25% for both the values of the elastic modulus and the yield strength. Our results constitute the most direct check of the G-A predictions since the conditions of comparison are as similar as possible for the nanoporous samples and the nanowires. Some differences still remain, mostly due to the fact that in the case of the nanowires the deformation axis is always normal to the surface, whereas in the case of the nanoporous samples there is a distribution of angles between the surface normal and the deformation axis. In the case of the nanowires, the surface orientations represented may also be somewhat different for the ones in the nanoporous case. However, these differences result in relatively small deviations form the G-A predictions.

In addition, we have found that both the NP-Au samples and the nanowires present surface effects that result in a compressive internal stress of the ligament/nanowires linear with the inverse of the ligament/nanowire size. The effects of the surfaces on the overall behavior of the wires and NP-Au structures are significant for the small wire or ligament sizes. Most importantly, they are opposite in sign depending on whether the applied stress is tensile or compressive. The internal stresses due to the surfaces result in weakening of the smallest wires and NP-Au structures under compression and further strengthening under tension.

Multiplying the slopes of the trend lines for the data in Fig. 4 by (3/2) (the scaling factor for the relation given in terms of surface area to volume ratio), we can obtain estimates for the value of f based on internal stress. The results are given in the Table 2 below, along with the surface energy and surface stress for several surfaces, calculated for the EAM potential used in our simulations [7]. Table 2 also includes the value of the surface term obtained from our model for the tension/compression asymmetry in both the nanowires and the NP-Au samples. The surface term was obtained using the factor of ((2/3)(S/V)) from the equation above and, for the NP-Au sample, Gibson-Ashby scaling.

The detailed comparison with Gibson-Ashby scaling in the preset work was performed for one sample with solid volume fraction of 0.4, and varying ligament diameters. The present results therefore do not thoroughly test the validity of Gibson-Ashby scaling for other solid fractions. In fact, in a separate paper, we report results for similar samples of various volume fractions [75], and show that for lower solid fractions, the load is not carried uniformly by all ligaments which under compression results in significant deviations from the Gibson-Ashby scaling relations for lower solid fractions.

It is important here to note the recent work mentioned earlier by Luhrs et al. confirms experimentally the yield asymmetry discussed in this paper [47]. An important effect observed by Luhrs et al. is a change in Plastic Poisson's ratio as a function of ligament diameter under compression. In our samples, we also see an increase in plastic Poisson's ratio from 0.27 for our smallest ligament sample to 0.29 for our largest ligament samples at 10% compressive strain. Interestingly, we observe the

opposite effect under tension, with the plastic Poisson ratio decreasing from 0.34 to 0.23 as a function of ligament size.

The results of our simulations cannot clearly establish if the surface effect is governed by surface tension or surface stress. Simulations that can help address this issue could be performed using a series of interatomic potentials that specifically adjust the surface stress independent of the surface energy. This is beyond the scope of the present work, but is planned for the future.

Our results also do not address the exact atomistic mechanism by which dislocation emission from the surface is actually easier under compression. Our results have shown that the surface atoms are under tension, whereas the interior of the ligaments are under compression. It is possible that it is this gradient in stress values that helps in dislocation nucleation. This issue has recently been addressed for nanowires [69] and it has been shown that indeed dislocation nucleation is easier for smaller wires under compression, consistent with the findings of the present work.

3.5 Summary

We have presented a study of NP-Au where the effects of ligament diameter are observed via use of molecular dynamics. We have shown that there is a definite relation of internal stress to the size of individual ligaments, and this contributes to the possible formation of dislocations in NP-Au samples. Furthermore, and perhaps most profoundly, there is a pronounced asymmetry between the yield stress values for both nanowire samples and NP-Au samples, which decreases with ligament diameter. We have shown that this asymmetry can be modeled quite accurately based on a surface contribution term. On the basis of the present results, we cannot definitively state whether this term is related to the surface energy or the surface stress and this will be the focus of future work. Furthermore, we have observed that dislocations, which appear to be the primary mode of deformation, seem to nucleate at regions of high curvature, where large compressive stresses are close to high tensile stress on the surface. Finally, we note that dislocation densities seem to be higher for smaller ligament diameter samples, and for samples subjected to tension.

3.6 **Acknowledgements and Funding Sources**:

The authors wish to acknowledge the Virginia Tech Advanced Research Computing Facilities and specifically the Blueridge computing cluster for providing both the computational time and the memory space to perform the simulations referred to in this text. We wish also to acknowledge the support from our funding source, NSF DMREF grant number 153396

3.7 References:

[1] N. Badwe, X.Y. Chen, K. Sieradzki, Mechanical properties of nanoporous gold in tension, Acta Materialia 129 (2017) 251-258.
[2] T.J. Balk, C. Eberl, Y. Sun, K.J. Hemker, D.S. Gianola, Tensile and Compressive Microspecimen Testing of Bulk Nanoporous Gold, Jom 61(12) (2009) 26-31.
[3] A.M. Hodge, J.R. Hayes, J.A. Caro, J. Biener, A.V. Hamza, Characterization and mechanical behavior of nanoporous gold, Adv. Eng. Mater. 8(9) (2006) 853-857.
[4] J. Biener, A.M. Hodge, A.V. Hamza, L.M. Hsiung, J.H. Satcher, Nanoporous Au: A high yield strength material, Journal of Applied Physics 97(2) (2005) 4.
[5] A.M. Hodge, J. Biener, J.R. Hayes, P.M. Bythrow, C.A. Volkert, A.V. Hamza, Scaling equation for yield strength of nanoporous open-cell foams, Acta Materialia 55(4) (2007) 1343-1349.
[6] N.J. Briot, T.J. Balk, Developing scaling relations for the yield strength of nanoporous gold, Philosophical Magazine 95(27) (2015) 2955-2973.
[7] N.J. Briot, T. Kennerknecht, C. Eberl, T.J. Balk, Mechanical properties of bulk single crystalline nanoporous gold investigated by millimetre-scale tension and compression testing, Philosophical Magazine 94(8) (2014) 847-866.
[8] M. Buerckert, N.J. Briot, T.J. Balk, Uniaxial compression testing of bulk nanoporous gold, Philosophical Magazine 97(15) (2017) 1157-1178.
[9] D.A. Crowson, D. Farkas, S.G. Corcoran, Mechanical stability of nanoporous metals with small ligament sizes, Scripta Materialia 61(5) (2009) 497-499.
[10] D. Farkas, A. Caro, E. Bringa, D. Crowson, Mechanical response of nanoporous gold, Acta Mater. 61(9) (2013) 3249-3256.
[11] M. Hakamada, M. Mabuchi, Mechanical strength of nanoporous gold fabricated by dealloying, Scripta Materialia 56(11) (2007) 1003-1006.
[12] J. Jiao, N. Huber, Deformation mechanisms in nanoporous metals: Effect of ligament shape and disorder, Computational Materials Science 127 (2017) 194-203.
[13] E.T. Lilleodden, P. Voorhees, Characterization of Dealloyed Nanostructures MRS Bull. 43(1) (2018)
[14] J. Erlebacher, M.J. Aziz, A. Karma, N. Dimitrov, K. Sieradzki, Evolution of nanoporosity in dealloying, Nature 410(6827) (2001) 450-453.
[15] Q. Chen, Y. Ding, M.W. Chen, Nanoporous Metal by Dealloying for Electrochemical Energy Conversion and Storage, MRS Bull. 43(1) (2018).
[16] X.L. Ye, N. Lu, X.J. Li, K. Du, J. Tan, H.J. Jin, Primary and Secondary Dealloying of Au(Pt)-Ag: Structural and Compositional Evolutions, and Volume Shrinkage, J. Electrochem. Soc. 161(12) (2014) C517-C526.
[17] H.J. Jin, D. Kramer, Y. Ivanisenko, J. Weissmuller, Macroscopically strong nanoporous pt prepared by dealloying, Adv. Eng. Mater. 9(10) (2007) 849-854.
[18] I. McCue, A. Karma, J. Erlebacher, Pattern Formation During Electrochemical and Liquid Metal Dealloying, MRS Bull. 43(1) (2018).
[19] J.F. Rodriguez-Nieva, C.J. Ruestes, Y. Tang, E.M. Bringa, Atomistic simulation of the mechanical properties of nanoporous gold, Acta Materialia 80 (2014) 67-76.
[20] H.J. Jin, L. Kurmanaeva, J. Schmauch, H. Rosner, Y. Ivanisenko, J. Weissmuller, Deforming nanoporous metal: Role of lattice coherency, Acta Materialia 57(9) (2009) 2665-2672.

[21] L. Luhrs, C. Soyarslan, J. Markmann, S. Bargmann, J. Weissmuller, Elastic and plastic Poisson's ratios of nanoporous gold, Scripta Materialia 110 (2016) 65-69.
[22] C.J. Ruestes, D. Farkas, A. Caro, E.M. Bringa, Hardening under compression in Au foams, Acta Materialia 108 (2016) 1-7.
[23] B. Roschning, N. Huber, Scaling laws of nanoporous gold under uniaxial compression: Effects of structural disorder on the solid fraction, elastic Poisson's ratio, Young's modulus and yield strength, Journal of the Mechanics and Physics of Solids 92 (2016) 55-71.
[24] G. Pia, M. Carta, F. Delogu, Nanoporous Au foams: Variation of effective Young's modulus with ligament size, Scr. Mater. 144 (2018) 22-26.
[25] J. Diao, K. Gall, M.L. Dunn, Yield Strength Asymmetry in Metal Nanowires, Nano Letters 4(10) (2004) 1863-1867.
[26] J.K. Diao, K. Gall, M.L. Dunn, J.A. Zimmerman, Atomistic simulations of the yielding of gold nanowires, Acta Materialia 54(3) (2006) 643-653.
[27] W. Zhang, T. Wang, X. Chen, Effect of surface stress on the asymmetric yield strength of nanowires, J. Appl. Phys. 103(12) (2008) 123527.
[28] C.R. Weinberger, W. Cai, Plasticity of metal nanowires, J. Mater. Chem. 22(8) (2012) 3277-3292.
[29] L. Lührs, B. Zandersons, N. Huber, J. Weissmüller, Plastic Poisson's Ratio of Nanoporous Metals: A Macroscopic Signature of Tension–Compression Asymmetry at the Nanoscale, Nano Letters 17(10) (2017) 6258-6266.
[30] L.J. Gibson, M.F. Ashby, Cellular Solids: Structure and Properties, 2 ed., Cambridge University Press, Cambridge, UK, 1997.
[31] L.J. Gibson, M.F. Ashby, The mechanics of three-dimensional cellular materials, Proceedings of the Royal Society of London A: Mathematical, Physical and Engineering Sciences, The Royal Society, 1982, pp. 43-59.
[32] L.J. Gibson, M.F. Ashby, Cellular Solids: Structure and Properties, 2 ed., Cambridge University Press, Cambridge, 1997.
[33] H.-J. Jin, J. Weissmüller, D. Farkas, Mechanical response of nanoporous metals: A story of size, surface stress, and severed struts, 43(1) (2018).
[34] J.R. Greer, W.D. Nix, Nanoscale gold pillars strengthened through dislocation starvation, Physical Review B 73(24) (2006).
[35] R. Dou, B. Derby, Deformation mechanisms in gold nanowires and nanoporous gold, Philosophical Magazine 91(7-9) (2011) 1070-1083.
[36] R. Xia, R.N. Wu, Y.L. Liu, X.Y. Sun, The Role of Computer Simulation in Nanoporous Metals-A Review, Materials 8(8) (2015) 5060-5083.
[37] E.A. Holm, S.M. Foiles, E.R. Homer, D.L. Olmsted, Comment on "Toward realistic molecular dynamics simulations of grain boundary mobility" by Zhou and Mohles, Scripta Materialia 66(9) (2012) 714-716.
[38] J.K. Diao, K. Gall, M.L. Dunn, Atomistic simulation of the structure and elastic properties of gold nanowires, Journal of the Mechanics and Physics of Solids 52(9) (2004) 1935-1962.
[39] X.-Y. Sun, G.-K. Xu, X. Li, X.-Q. Feng, H. Gao, Mechanical properties and scaling laws of nanoporous gold, J. Appl. Phys. 113(2) (2013) 023505.
[40] K. Kolluri, M.J. Demkowicz, Coarsening by network restructuring in model nanoporous gold, Acta Materialia 59(20) (2011) 7645-7653.
[41] A.C. To, S.F. Li, Perfectly matched multiscale simulations, Phys. Rev. B 72(3) (2005) 8.

[42] B.-N.D. Ngô, A. Stukowski, N. Mameka, J. Markmann, K. Albe, J. Weissmüller, Anomalous compliance and early yielding of nanoporous gold, Acta Materialia 93(0) (2015) 144-155.
[43] D.A. Crowson, D. Farkas, S.G. Corcoran, Geometric relaxation of nanoporous metals: The role of surface relaxation, Scripta Materialia 56(11) (2007) 919-922.
[44] S. Plimpton, FAST PARALLEL ALGORITHMS FOR SHORT-RANGE MOLECULAR-DYNAMICS, Journal of Computational Physics 117(1) (1995) 1-19.
[45] S.M. Foiles, M.I. Baskes, M.S. Daw, Embedded-Atom-Method Functions for the Fcc Metals Cu, Ag, Au, Ni, Pd, Pt, and Their Alloys, Physical Review B 33(12) (1986) 7983-7991.
[46] K.F. Joshua Stuckner, Ian McCue, Michael J. Demkowicz , Mitsuhiro Murayama AQUAMI: An open source Python package and GUI for the automatic quantitative analysis of morphologically complex multiphase materials, Computational Materials Science 139 (2017) 320-329.
[47] A. Stukowski, K. Albe, Extracting dislocations and non-dislocation crystal defects from atomistic simulation data, Model. Simul. Mater. Sci. Eng. 18(8) (2010) 13.
[48] A. Stukowski, K. Albe, Extracting dislocations and non-dislocation crystal defects from atomistic simulation data, Modelling and Simulation in Materials Science and Engineering 18(8) (2010).
[49] J.W. Gibbs, Scientific Papers of Josiah Willard Gibbs, Volume 1, Solr Books, Skokie, Il, USA, 1928.
[50] J. Weissmüller, J.W. Cahn, Mean stresses in microstructures due to interface stresses: A generalization of a capillary equation for solids, Acta Materialia 45(5) (1997) 1899-1906.
[51] J. Weissmüller, H.L. Duan, D. Farkas, Deformation of solids with nanoscale pores by the action of capillary forces, Acta Materialia 58(1) (2010) 1-13.
[52] K.M. Knowles, P.R. Howie, The Directional Dependence of Elastic Stiffness and Compliance Shear Coefficients and Shear Moduli in Cubic Materials, Journal of Elasticity 120(1) (2015) 87-108.
[53] Q.-J. Li, B. Xu, S. Hara, J. Li, E. Ma, Sample-size-dependent surface dislocation nucleation in nanoscale crystals, Acta Materialia 145 (2018) 19-29.
[54] N. Mameka, J. Markmann, J. Weissmüller, On the impact of capillarity for strength at the nanoscale, Nature Communications 8(1) (2017) 1976.
[55] B. Hyde, H.D. Espinosa, D. Farkas, An atomistic investigation of elastic and plastic properties of Au nanowires, Jom 57(9) (2005) 62-66.
[56] Y.C. Kim, E.J. Gwak, S.M. Ahn, J.I. Jang, H.N. Han, J.Y. Kim, Indentation size effect in nanoporous gold, Acta Materialia 138 (2017) 52-60.
[57] C.A. Volkert, E.T. Lilleodden, Size effects in the deformation of sub-micron Au columns, Philosophical Magazine 86(33-35) (2006) 5567-5579.
[58] J. Biener, A.M. Hodge, J.R. Hayes, C.A. Volkert, L.A. Zepeda-Ruiz, A.V. Hamza, F.F. Abraham, Size effects on the mechanical behavior of nanoporous Au, Nano Letters 6(10) (2006) 2379-2382.
[59] N. Beets, D. Farkas, Mechanical Response of Au Foams of Varying Porosity from Atomistic Simulations, JOM 70(10) (2018) 2185-2191.

Chapter 4: Fracture in Nanoporous Gold: an Integrated Computational and Experimental Study

Nathan Beets1*, Joshua Stuckner1, Mitsuhiro Murayama1, Diana Farkas1,

1 Department of Materials Science and Engineering, Virginia Tech
Holden Hall, 445 Old Turner St #213, Blacksburg, VA 24060

* Corresponding Author
email: bnathan2@vt.edu

4.0 Abstract

We present simulation/experimental integrated study examining crack propagation in nanoporous gold. We utilized a simulation technique that combines continuum fracture mechanics with molecular dynamics. We applied this to a large atomistic digital sample of nanoporous gold to implement mode-1 crack propagation. Crack propagation tests were also conducted on an experimental sample, prepared via chemical dealloying and observed via in-situ TEM microscopy. We observed cracks in both samples propagating by the same mechanisms of sequential individual ligament failure. A series of nanowire computational deformation tests were also conducted to understand individual ligament behavior, and how this influences the overall sample fracture. This iterative direct experiment/simulation comparison provides new insight into the failure response of nanoporous gold.

4.1. Introduction:

Nanoporous gold (NPG) is a multifunctional material with applications in targeted DNA sensing [1], actuation [2], chemical sensing [3, 4], radiation resistance [5, 6], impact absorption [7], device interconnects [8], and catalysis [9-12]. The material gains useful chemical properties from its foam structure comprised of randomly curving ligaments and a continuous network of nanoscale pores. Along with desirable chemical properties, the nanoporous structure causes the material to fracture easily. Individual ligaments at the crack surface undergo nanoscale plasticity but the strain is not shared by nearby ligaments leading to flow localization and brittle macroscale behavior. The mechanical behavior of NPG is also very sensitive to surface conditions, such as surface stress and oxidation [13-15]. Several experimental studies have been conducted to look at the fracture behavior of NPG, but the crack propagation and failure mechanisms remain unclear. Large-scale atomistic simulations can offer a unique insight by giving detailed thermodynamic and structure-property data atom-by-atom to help explain the behavior observed from a more fundamental perspective.

Ligament diameter has a major impact on the chemical and mechanical properties of the material. While closed porous lattices have been shown to be theoretically stronger, open porous systems are more interesting from an applications standpoint, and are easier to synthesize [16]. Many desirable properties such as catalytic activity and high specific surface area are most pronounced at ligament diameters of 30 nm or less [17]. In both compression and tension, samples with smaller ligament diameters have higher yield strengths [18, 19]. In compression, NPG is extremely ductile and undergoes significant hardening during deformation due to pore

densification [20, 21]. In tension, when the ligament diameter is less than about 220 nm the material becomes brittle and fractures with a single dominant crack and extreme flow localization [22, 23]. It is possible that macroscale brittleness results from small ligaments' inability to store strain-hardening defects such as dislocations, which leads to extreme flow localization where all the strain is confined to a local band [24, 25]. Post-fracture SEM images revealed that even after a macroscopically brittle fracture, individual ligaments experience nanoscale plasticity with significant necking and ductile elongation although the overall strain is only 1-2 ligament/pore widths [26, 27]. It remains unclear why a brittle single dominant crack is favored in smaller ligament samples compared to the ductile behavior of multiple crack failure in samples with larger ligaments. The exact nature of crack propagation through the porous material and the magnitude and precise location of the accompanying stress concentrations are not known.

The deformation behavior of NPG and other nanoporous metals involves a complex interplay between the deformation behavior of the nanoporous foam structure and that of the individual gold ligaments within the structure [27-31]. Plastic deformation behavior and ligament-by-ligament failure of the ligament structure of nanoporous metals can be understood in the context of the deformation of gold nanowires, as the ligament structure of nanoporous gold can be interpreted as a series of interconnected nanowires connected at nodes [15, 27, 32-35]. However, gold ligaments in NPG are often more curved than gold nanowires and have a random variation of ligament diameter across the length. The foam structure has often been compared to Gibson-Ashby foams but so far, applying Gibson-Ashby style scaling laws to NPG has been only moderately successful [32, 36-38]. The nanoporous structure involves several complications compared to Gibson-Ashby foams, with prominent surface effects of the nanoscale ligaments, a more complex random structure with curving ligaments of variable sizes, and dangling ligaments, which increase the solid fraction but do not contribute to load bearing [39]. Stress is applied to individual ligaments from their connecting nodes and numerical modeling suggests that the structure imparts primarily torsional and bending forces on the individual ligaments even when the overall sample is stressed in pure tension or compression [40]. Bending stresses create a strain gradient on NPG ligaments and lead to the formation of twin boundaries and stacking faults that are geometrically necessary to accommodate lattice rotation during bending [27]. NPG maintains the grain structure of the parent alloy, which is much larger than individual ligaments. The random orientation of ligaments within a single grain causes stress passed through the nodes to be applied to adjacent individual ligaments in different crystallographic directions. In FCC metals, dislocations travel on specific crystal planes and the fraction of stress resolved on those planes depends on the crystallographic loading direction based on the Schmid factor. Thus, adjacent ligaments will have different yield strengths and deformation behavior based solely on the orientation of the applied stress. After yielding, ductility and the types of defect structures formed during plastic deformation are also affected by the orientation of applied stress. Gold wires loaded in the <111> direction experience the highest ductility due to symmetry of the {111} slip planes, which reduces necking localization [41]. When loaded in the <110> direction, the shear stress resolved on the slip plane of the leading Shockley partial dislocation may be higher than that for the trailing partial leading to partial dislocations on adjacent {111} planes causing the formation of twins [42]. Twins can lead to a nanoscale brittle fracture in gold nanowires [43]. Loading in the <111> and <100> directions favor full dislocations and dislocation mediated slip without the formation of defects in gold nanowires.

Twin boundaries or stacking fault defects, whether formed by loading direction or bending forces, can block dislocations and cause strain hardening. When an individual ligament fails it connects two pores creating a large crack that increases stress concentration on neighboring sections of the foam structure [24]. Clearly there is a complex relationship between the deformation of the nanoporous structure and the individual ligaments with both affecting the other. Therefore, a complete picture of the fracture behavior requires the analysis of the deformation behavior of the individual ligaments as well as the overall foam structure.

Atomistic simulations have contributed to the current understanding of the deformation behavior of NPG, addressing deviations from the Gibson-Ashby expected scaling as well as tension/compression asymmetry [15-16, 20-21]. Atomistic studies combined with linear elastic fracture mechanics [44] have also been useful in understanding the fracture behavior of nanocrystaline metals [44-48]. The purpose of the present work is to apply these atomistic techniques, in combination with experiments, to the fracture of NPG. Our approach utilizes both the power and detail of high resolution TEM microscopy with the atom-by-atom physical detail of molecular dynamics. In this study, we performed in situ transmission electron microscopy (TEM) fracture experiments alongside a molecular dynamics (MD) fracture simulation on a digital sample with a similar morphology to observe the mechanical response of the material during crack propagation including the formation of defect structures and the location and magnitude of stresses. Using recent advances in computational power, our study utilizes simulated and experimental samples of similar ligament diameters and morphology. The atomistic studies included nanowire simulations to compare with the large scale computational sample. The behaviors of both experimental and computational samples are analyzed in terms of the ligament-by-ligament failure mechanisms. A series of simulations were also run to compare individual ligament behavior with simulated nanowires of similar sizes.

4.2. Materials And Methods

4.2.1 Computational Methods

Several methods have been proposed to generate computational samples with morphologies similar to those observed experimentally [49-51]. We employed a phase-field technique, as described in our previous work [15]. This technique can create morphologies with variable porosities. This method can create fully periodic samples, and has been shown to have very good morphological agreement with experimental samples [52, 53]. Using this technique we created a periodic morphology with 60% porosity, and dimensions of 60nm by 60 nm by 200 nm.

To fill the structure with atoms, we overlaid an FCC lattice with the desired lattice parameter (0.408 nm) and canonical orientation. The sample contained about 20 million atoms, with average ligament diameter of around 5.0 nm, and 60% porosity. This ligament diameter is somewhat less than the 10 nm average ligament diameter measured in our experimental sample (see section 2.2). This constraint is due to the limitations of available computational power. Our simulation sample has at least 5 ligaments per box length to allow for reasonable statistics as the crack advances. We also note that 5 nm is well above the stability threshold for gold nanowires and nanoporous structures [23]. For comparison to the failure behavior of individual ligaments,

nanowire samples were made in two different morphologies, cylindrical and hyperboloid. For each morphology, a different orientation of the lattice was applied with [100], [110], [111], and [112] crystal directions oriented along the nanowire axis. The sizes were chosen to match the ligaments in the NPG simulation sample. These allowed the analysis of any orientation dependence in the elastic/plastic response, and the ultimate failure conditions of the individual wires.

Molecular dynamics simulations were performed using LAMMPS [54]. The interatomic potential for Au used is that of Baskes and Foiles [55]. All the samples were relaxed at 300 K for 2 ns. The continuum solution for a Mode I semi-infinite crack (Equations 1 and 2 below) was used to introduce a crack with controlled stress intensity in the NPG digital sample. Each atom in the sample is displaced according to these equations.

$$u_x = \frac{K_I}{\mu}\sqrt{\frac{r}{2\pi}}\left[1 - 2\nu + \sin^2\left(\frac{\theta}{2}\right)\right]\cos\left[\frac{\theta}{2}\right] \quad (1)$$

$$u_y = \frac{K_I}{\mu}\sqrt{\frac{r}{2\pi}}\left[1 - 2\nu - \cos^2\left(\frac{\theta}{2}\right)\right]\sin\left[\frac{\theta}{2}\right] \quad (2)$$

Here, ux and uy are the displacement magnitudes, r and θ are the distance and angle from the crack tip being deformed, μ is the shear modulus ν is the Poisson ratio, KI is the mode I stress intensity factor. The way this formalism deformed the sample is shown schematically in Figure 1.

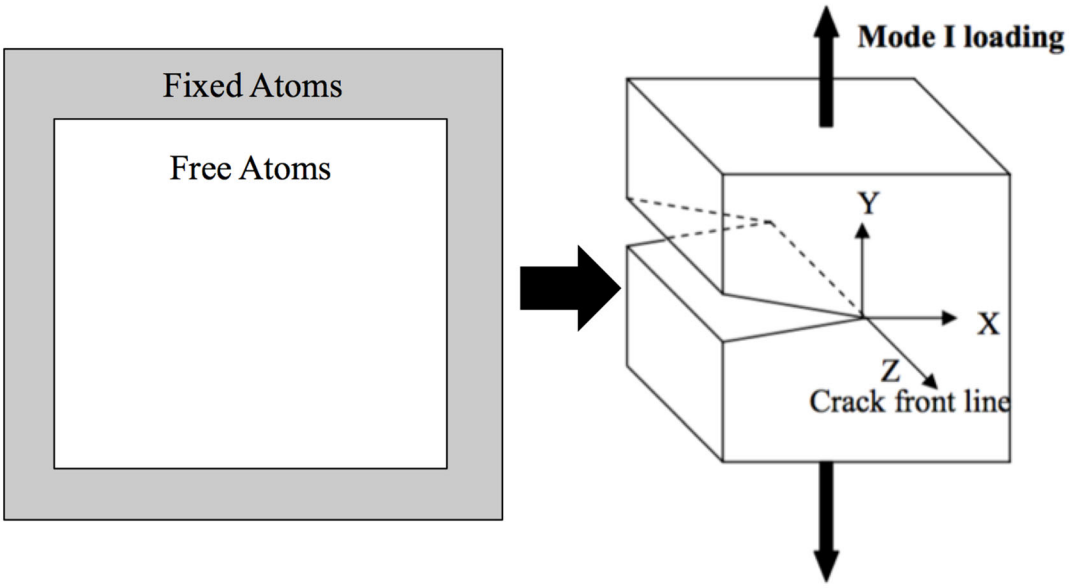

Figure 4-1: The setup for our combined continuum/molecular dynamics approach. An outer region of atoms is deformed by the equations of linear elastic fracture mechanics for a mode 1 crack up to a particular K value. The interior atoms are allowed to move according to the forces in molecular dynamics.

After the initial, purely continuum-based deformation of the sample, atoms in a thin layer around the sample perpendicular to the crack tip were fixed according to the above equations to control the total sample stress intensity. Molecular dynamics was performed on all atoms not contained in this region, so that near-tip mechanical behavior was governed by the MD formalism with the selected embedded atom interatomic potential. The critical stress intensity value was determined as the value for which the crack remains stable during relaxation without closing or advancing.

Since we are dealing with a nanoporous sample, some account for how the porous structure changes the shear modulus must be factored in for determining the stress tip intensity. Gibson and Ashby have shown that for macro-scale foams, equation 3 can be used to determine the elastic modulus based on the porosity of the lattice in question.

$$E = E_s \left(\frac{\rho}{\rho_s}\right)^2 \tag{3}$$

Theoretically, the same formalism should apply for the shear modulus of our material. To test this, we used the aforementioned phase-field method to create a cubic periodic nanoporous sample with side lengths 450 nm with the same volume fraction and ligament diameter as our large sample. We sheared this sample in the x, y, and z directions up to 1% strain at a strain rate of 3.0 × 108, and measured the shear modulus using the calculated stress values from the LAMMPS log file. The average of the modulus in the three directions was 4.87 GPa. Using a value for the shear modulus of gold of 27 GPa, the Gibson-Ashby correction gives us a value of 4.99 GPa. Since these values differ by only 2%, we can reasonably assume the Gibson-Ashby scaling relation applies for the shear modulus in our tip stress intensity calculations. By performing a uniaxial compression test for each cubic side, the Poisson ratio for our sample was calculated to be 0.36. We calculated the critical stress intensity of our sample to be 0.2 MPa$\sqrt{}$ m, and during the deformation, varied the stress intensity from 0.2 MPa$\sqrt{}$ m to 1.79 MPa$\sqrt{}$ m. This range of stresses was applied over a period of 30 ns. Visualization of the results was performed with the OVITO package, including the dislocation extraction algorithm (DXA)[56].

4.2.2 Experimental Methods

NPG samples were produced by free dealloying pieces of white gold leaf for 20 minutes in 70 vol. % nitric acid as described elsewhere [57]. The gold leaf sheets, which were about 300 nm thick and contained 65 at. % Ag, were purchased from W&B Gold Leaf, LLC. After dealloying, the NPG samples were rinsed in deionized water and placed directly onto a SATO Holder Duo (Mel-Build Co.), shown in Figure 2, which is capable of in situ TEM mechanical testing. The NPG samples contained about 5 at. % residual silver and had ligament diameters of 9.6 ± 4.0 nm as measured by AQUAMI [58]. Each sample was ion milled with a Leica TIC 3X ion mill until the samples were thinned to electron transparency. In situ mechanical testing was performed with an FEI Titan 300 S/TEM operated in TEM bright field mode at 300 kV. During tensile straining, video was recorded with a Gatan Orious SC200D camera at up to 10 frames per second.

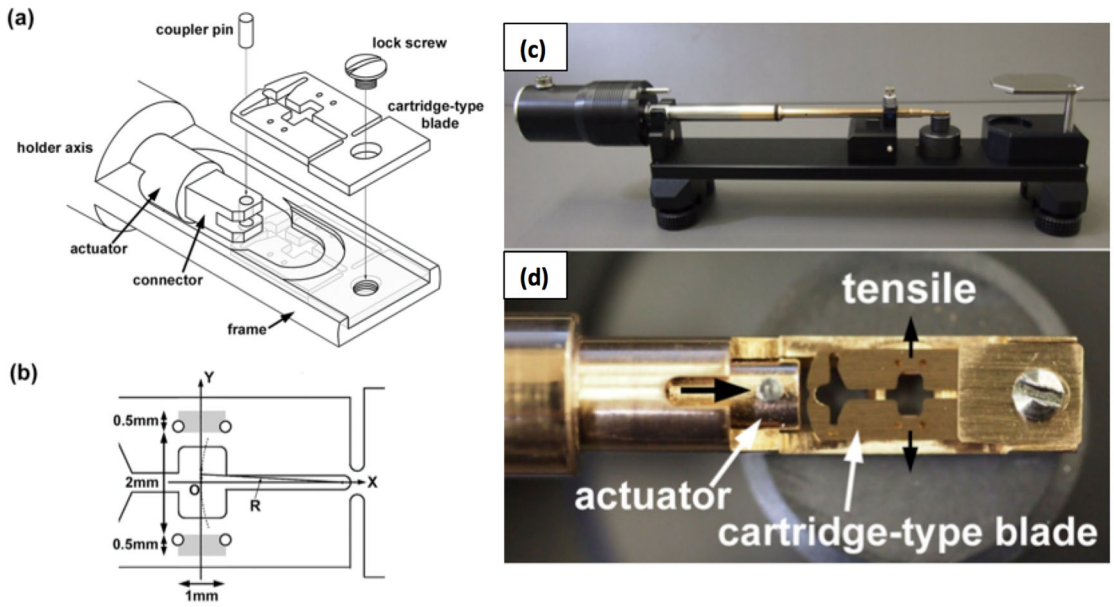

Figure 4-2: In situ TEM tensile deformation setup. (a) Schematic diagram of the holder apparatus with cartridge-type blade. (b) is a close op of said blade. (c) is the entire holder arm, and (d) is a picture of the cartridge-type blade with and indicator of the tensile force direction. The sample was placed on the gap between the two black arrows.
The structure can be compared to other samples compared via the same method, and a similar distribution of pores in pre-existing defects can be assumed.

4.3. Results

4.3.1 Experimental and simulated crack tip morphologies

In order to compare the atomistic simulation results with the experimental images obtained from TEM, the computational sample was visualized looking perpendicular to the crack front, allowing us to observe individual ligaments necking and failing and the overall crack propagation in the sample. The comparison of experiment and simulation is shown in Figure 3.

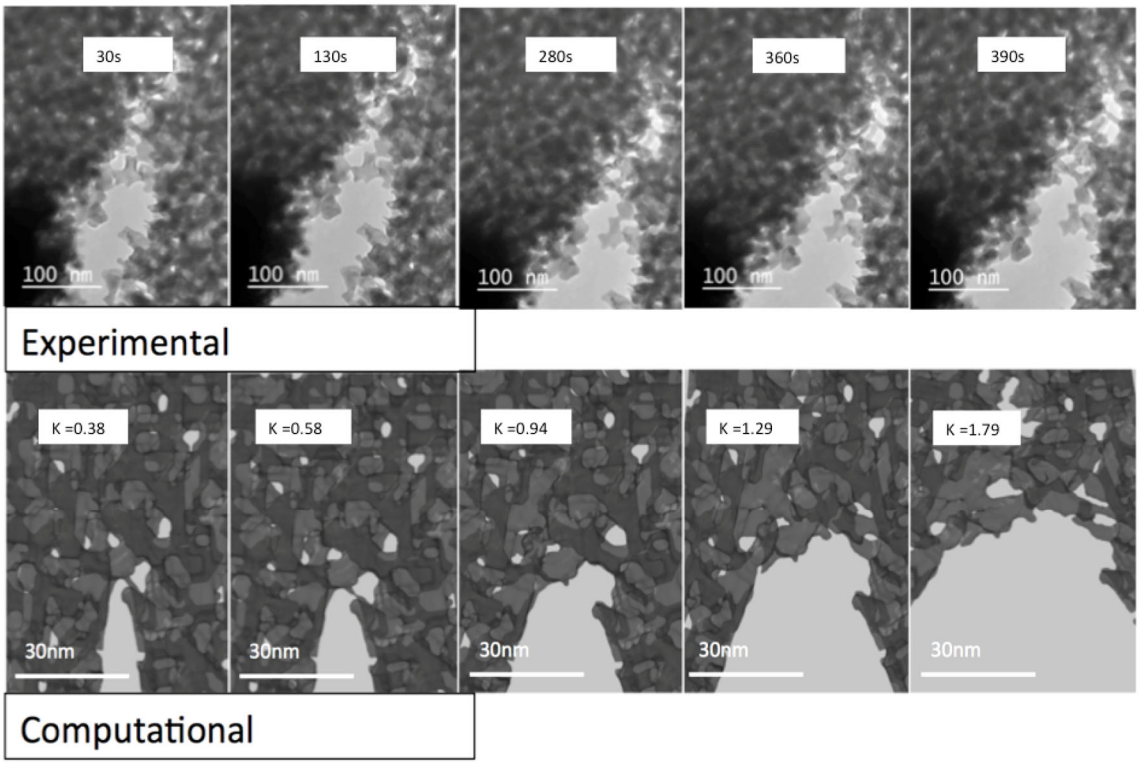

Figure 4-3: A comparison of the crack propagation in the sample observed in the TEM and in the computationally generated sample. For both, the crack front advances by ligaments necking and fracturing at the crack tip as the sample widens.

We found that the mechanisms of crack propagation, as well as the relative crack width in the computational and experimental sample were very similar. Ligaments at and near the crack tip necked and failed, while ligaments ahead of the crack tip thinned and weakened as the crack widened and the crack tip progressed. Propagation occurred as ligaments failed individually, distributing the majority of the load on to other ligaments further from the tip. Importantly, the crack front in neither sample visibly blunted, and propagation proceeded in a brittle manner with large strain localization. We observed individual ligament by ligament sequential failure and found that despite the difference in size and strain rate, the failure behavior of the simulated and experimental samples were nearly identical, as shown in Figure 4.

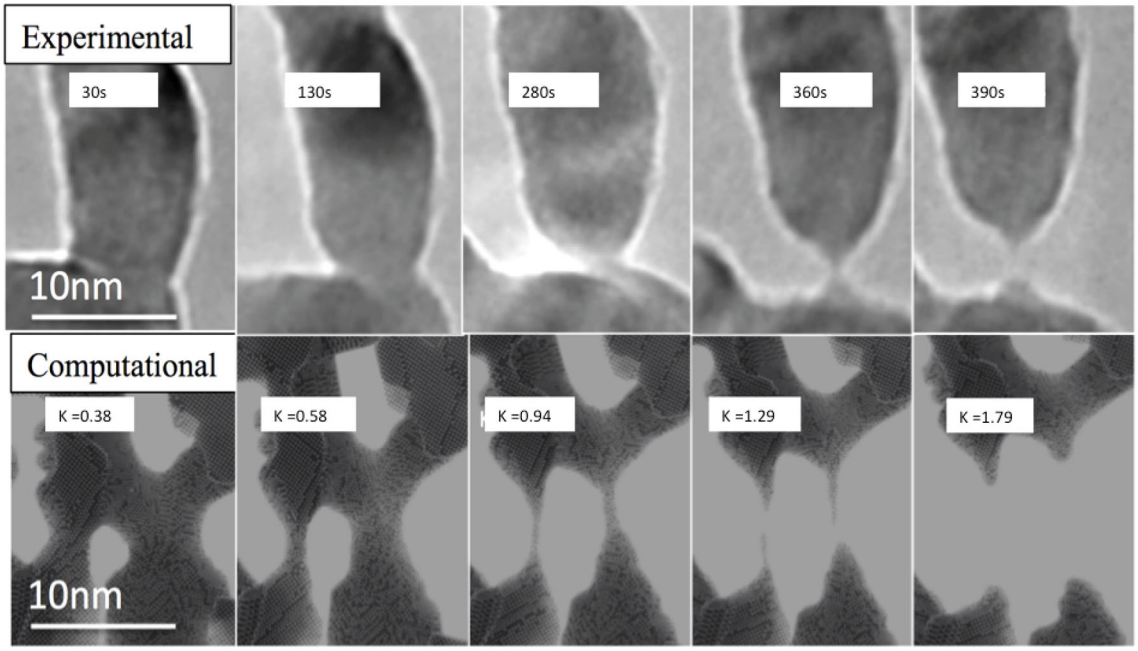

Figure 4-4: Individual ligament necking at the crack tip in both the computational and experimental sample proceeds by the same observed mechanisms. As ligaments are pulled in tension, they neck and elongate, until a single atom connects them. After fracture, capillary forces cause the previously completely connected ligaments to blunt.

Ligaments at the crack tip underwent elongation and necking, often forming a single-atom-bridge before pulling apart completely. Deformation and failure in both samples happened near the center in many of the ligaments (see supplemental videos SV11 and SV12). After complete failure, capillary forces took over, and the needle-like points of the separated atom-bridge blunted as the sample continued to deform. The ligament from the TEM sample in Figure 4 failed after significant localized necking. Initially the ligament was curved at a 90˚ angle and straightened in the tensile direction as the crack widened. The ligament experienced 30% elongation during the recording and had defect structures indicating that the ligament had undergone at least some plastic deformation before the start of recording. After the onset of necking, the ligament thinned rapidly in a narrow region. Deformation appeared to occur by dislocation mediated {111} slip on at least two slip planes. Defect structures were not formed in the necking region. The failure for the majority of the ligaments in both the computational and experimental samples was highly ductile. Not only are these results self-consistent, but also they validate what has been observed experimentally now for several years, namely macroscale brittleness is accompanied by nanoscale plasticity and ductile fracture of individual ligaments.

4.3.2 Crack propagation mechanisms

To analyze the details of crack propagation, we made four 12 nm slices through the 60 nm thick computational sample, perpendicular to the advancing front, and measured the tip position as a function of both slice position and total applied crack tip intensity. At the same time, we estimated the radius of curvature of the crack tip region for each slice and stress intensity value. This radius can help quantify the degree of blunting in the sample. Since this material is

essentially a mesh of interconnected nanowires with high capillary forces, and a very non-traditional crack front due to porosity, the radius of curvature should be seen as a semi-quantitative metric. Figure 5 shows how the sharpness of the crack tip varies during deformation for each of the slices considered.

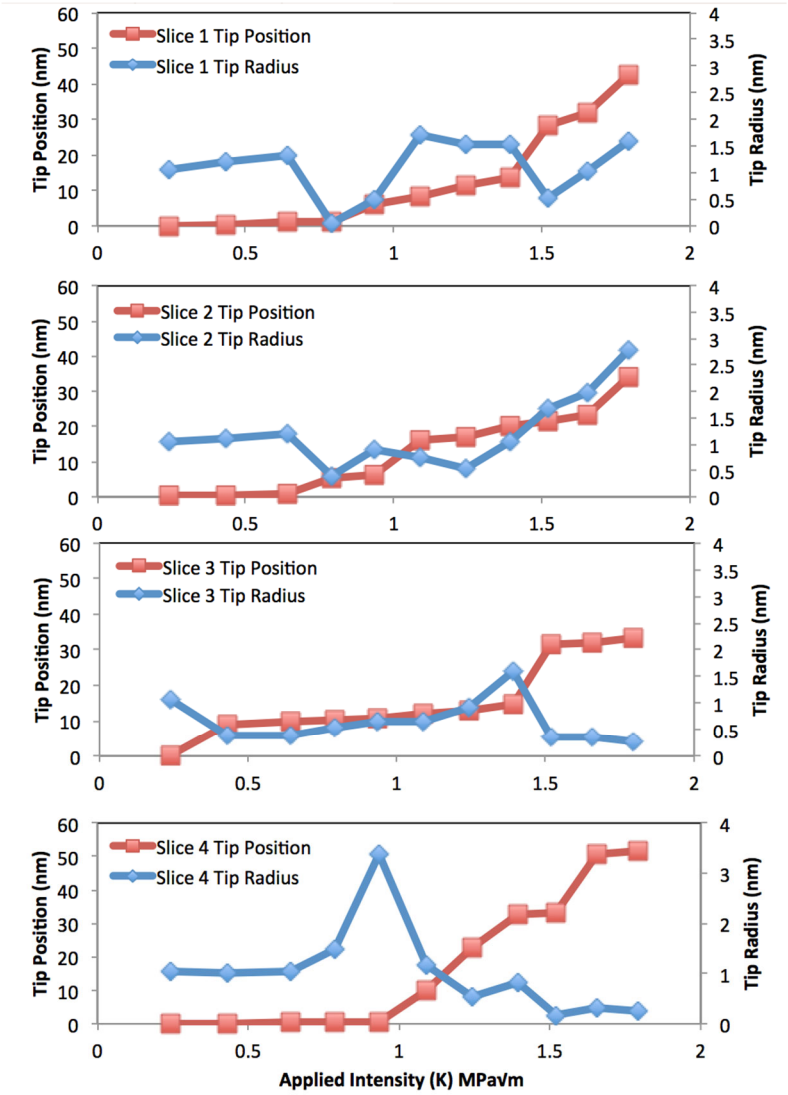

Figure 4-5: Tip position and measured tip radius vs. applied crack tip intensity for four different slices taken through the sample. (COLOR ONLINE)

Figure 5 also shows the crack position vs. the applied tip intensity. Correlating the two overlaid trends, we see that each time the radius of curvature drops significantly, there is a corresponding crack advance. This was seen most drastically in slice 4 at K = 0.94, slice 2 at K = 0.63, and slice 1 at 0.63. At these points, the ligaments at the crack tip were being elongated plastically, and in the process arrested tip advancement. At the next snapshot, these ligaments failed entirely, and the crack tip proceeded to the next ligament, beginning the process again. The correlation between tip advancement and the corresponding variation in the magnitude of radius decrease during deformation is clear but not perfect. This may be due to the effects of individual ligament orientation and morphology. Furthermore, since we were performing these

measurements using a two-dimensional projection of three-dimensional data, ligaments at the crack tip were not always oriented perpendicular to the tip plane and roughly in line with the tensile stress direction. Consequently, the relative degree of torsion vs. shear vs. tension for each ligament at a particular point in the deformation process varied, which in turn altered the number and type of defects during deformation. We can speculate that torsion is a significant contributing mechanism, but we cannot say for sure [41]. However, the fact that a common deformation trend was observed graphically, which can be correlated to a specific and consistently similar physical process (ligament elongation brought about by tensile loading), shows that this is a significant mechanism of crack front propagation, even if there are other factors to consider.

We also analyzed the variation in tip position along crack front by plotting the minimum, maximum and average position as a function of applied tip intensity. This is shown in Figure 6.

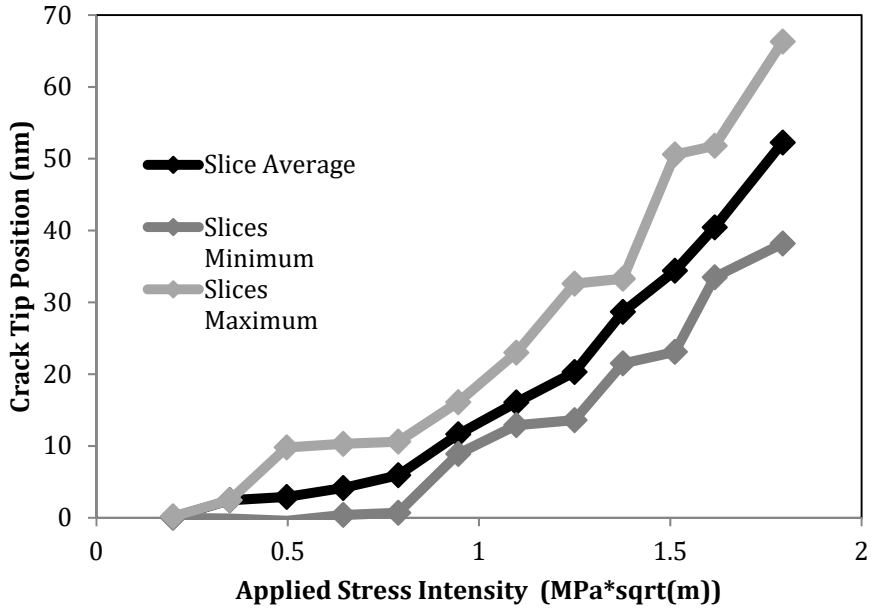

Figure 4-6: Crack tip position measured from the four slides by three metrics – total slice average, maximum position, and minimum position. Tip position deepens into the sample as applied stress tip intensity increases.

The variation in crack tip position observed along the crack front is 10 to 30 nm, that is on the order of a few ligaments sizes. This is consistent with the propagation mechanism dominated by the failure of individual ligaments.

4.3.3 Individual Ligament Deformation Mechanisms.

Next, we analyzed the individual deformation mechanisms in several selected ligaments that failed. Using the OVITO visualization package, we identified twin boundaries and stacking faults, as well as the dislocations responsible for such defects. An example is shown in Figure 7.

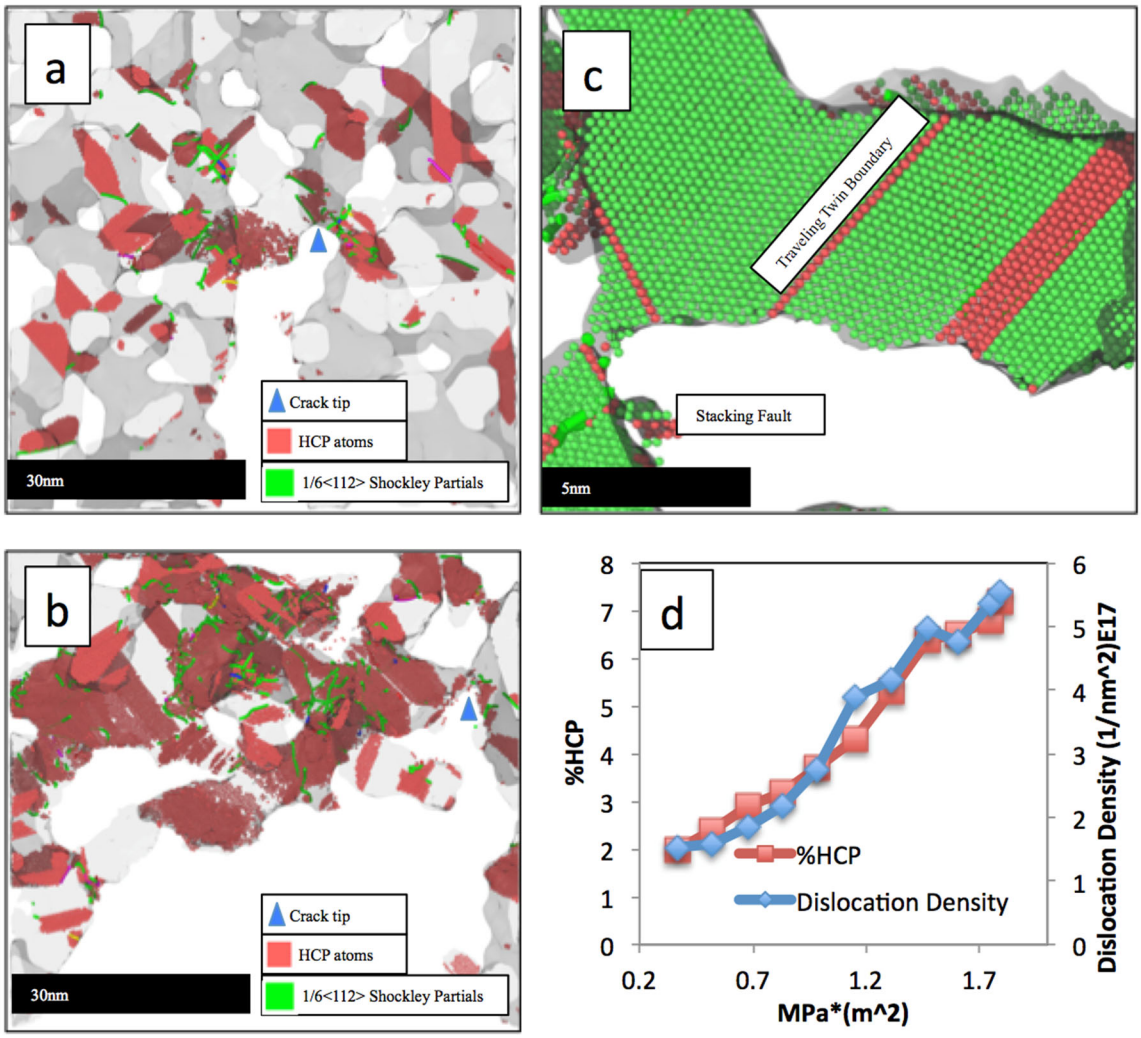

Figure 4-7: An analysis of the deformation mechanisms near the crack tip. (a) Stacking faults and dislocations formed just ahead of the crack tip at K = 0.51. (b) Same as above but at K = 1.20. (c) Formation of twin boundaries, stacking faults, and partial dislocations, indicating modes of bending and shear as well as tension. (d) The increase in both dislocation density and percentage of HCP atoms as a function of applied tip intensity.

Looking at the defect structure around the crack tip, we found that nucleation of Shockley partial dislocations from the surfaces is the most common type of deformation mechanism, with associated stacking faults (Figures 7a and 7b). Migrating twin boundaries are also present, as shown in Figure 7c. Figure 7d shows the percentage of HCP atoms for the whole sample as a function of time, along with the dislocation density of the entire sample. The common trend in dislocation density and HCP atoms shows that dislocations emitted very early during deformation are still present later on. Figure 8 shows the comparison of the planar faults observed in the simulation with the experiment. The variety of line defects here is consistent with bending tests performed on nanowires by several other groups [42, 59]. Due to the profusion of these defects near a crack tip, we expected a significant amount of strain hardening near the tip for these structures, which would dissipate the stress (and hence the deformation) deeper into the sample as controlled fracture proceeded. TEM experiments and simulation

results showed similar behavior, with an observed profusion of line defects with planar trailing HCP planes, nucleating from atomic steps on the surface, often coming from highly curved regions, which act as stress concentrators. As the deformation proceeded, some ligaments bent and realigned leading to a crystallographic misorientation within the bent ligaments. This misorientation arrested dislocation propagation and elimination at the opposite surface, and lead to dislocation pileup, as well as stacking fault saturation. This behavior is very similar in the experimental and computational samples, and lead to some strain hardening around the crack tip, as can be seen in Figure 8.

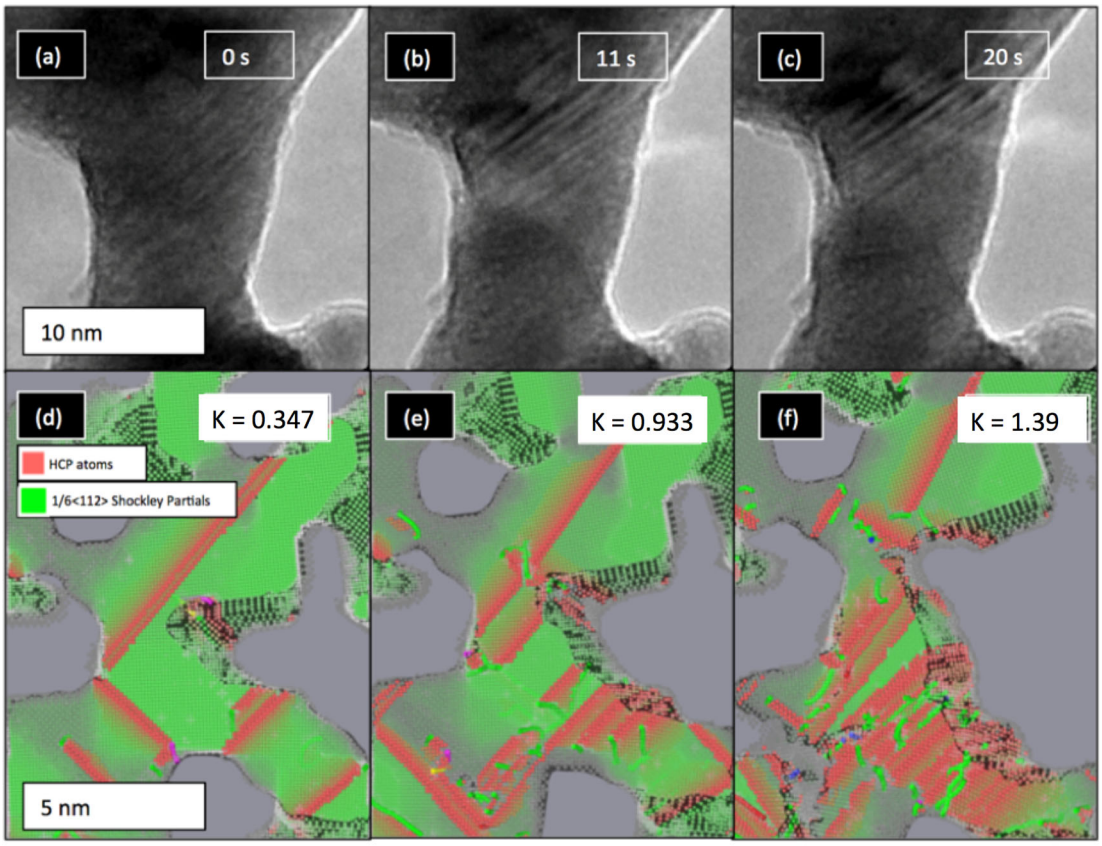

Figure 4-8: Comparison of defect structure for a single ligament during failure for the experimental and computational samples. We see lattice warping and re-orientation, bending at the nodes, as well dislocation entanglement and blocking by stacking faults and twin boundaries. (COLOR ONLINE)

4.3.4: Effects of ligament shape and orientation

The majority of ligaments in both computational and experimental samples deformed plastically after experiencing significant strain of up to 100% or more. However, some experimental ligaments failed after less than 40% strain and there was a large degree of variance. To see whether this was an effect of crystalline orientation, we created a series of cylindrical nanowires with the same average diameter as the ligaments that failed during crack propagation in the computational nanoporous sample. Each was relaxed and deformed in tension at a constant strain rate of 3.0 × 108 s-1 to total failure of the ligament. To study the effects of ligament

shape, we also created a series of hyperboloid-shaped ligaments with the same four crystalline orientations as the cylindrical nanowires and deformed in tension. This was motivated by the observation that in both the computational and experimental samples, failure most often occurred at the thinnest points in the ligaments, in places that were morphologically similar to hyperboloids. The hyperboloids created for testing purposes had the same minimum width as the average minimum width of the wires we were studying. Yield and failure conditions as well as fracture toughness for the nanowires of various orientations and two different shapes are given in Table 1.

Table 4-1: Failure data for cylindrical and hyperboloid nanowires. All wires 8.1 nm long with a diameter of 3.1 nm for the cylinders and 3.1 to 4.18 nm for hyperboloids. Toughness computed as the area under the stress-strain curve.

Crystalline Orientation	Width at thinnest Point	Yield Stress (GPa)	Elongation (nm)	Aspect Ratio	Failure strain	Toughness (GJ/m^3)
Cylindrical						
[100]	3.1	2.5	6.5	2.6	1.06	1.88
[110]	3.1	2.5	5.1	2.6	0.53	0.84
[111]	3.1	3.7	8	2.6	1.63	2.51
[112]	3.1	3.4	5.6	2.6	1.12	2.43
Hyperboloid						
[100]	3.1	4.1	2.6	2.6	0.49	0.99
[110]	3.1	5.5	5.5	2.6	1.06	3.68
[111]	3.1	3.8	3.2	2.6	0.73	1.12
[112]	3.1	5.1	3.8	2.6	0.47	1.44

The yield stress for cylindrical nanowires ranges from 2.5 to 3.7 GPa and from 3.8 to 5.1 GPa for hyperboloid nanowires. Failure strains range from 0.47 to 1.63 for cylindrical nanowires and from 0.43 to 1.03 for hyperboloid wires. There is a significant difference between cylindrical and hyperboloid wire failure conditions, with the hyperboloids typically failing at higher stresses and lower strains. Deformation response curves used to derive these values can be found in supplemental Figure S1a and S1b. Table 1 also includes the values observed for the toughness of each nanowire case, computed as the area under the stress-strain curve.

For comparison, Table 2 shows the local failure conditions of five selected ligaments that fail in our NPG digital sample. Local failure stresses were observed to range from 3.9 to 5.2 GPa and the local ligament failure strains varies from 0.26 to 0.75. Local stresses and strains were computed for each one of these ligaments by isolating the ligament atoms and computing stress and strain as given by only the atoms within the ligament, projected in the direction of deformation. The local deformation response for these selected ligaments is shown in supplemental Figure S3. The observed failure conditions of the ligaments in the NPG digital sample are closer in value to the hyperboloid nanowires than to cylindrical wires. This finding is consistent with the fact that actual shape of the ligaments in the NPG sample is more akin to the hyperboloids than to the cylindrical wires.

Table 4-2: Failure behavior of selected individual ligaments in the digital nanoporous sample. Toughness computed as the area under the local stress-strain curve corresponding to the individual ligament.

Ligament Number	Crystalline orientation*	Width at thinnest point	Yield stress (GPa)	Elongation (nm)	Aspect ratio	Failure strain	Toughness (GJ/m^3)
1	[14-1]	2.5	3.6	1.5	2.2	0.26	0.55
2	[0-11]	4.1	4.1	3.2	1.7	0.46	0.61
3	[121]	3.3	4.5	4.8	1.9	0.63	1.23
4	[110]	3.1	3.9	1.7	1.8	0.43	0.58
5	[111]	1.9	5.2	2.1	2.0	0.75	0.88

*Orientations measured within about 10 degrees.

We studied the distribution of both hydrostatic and Von Mises stress inside the different morphologies for a single orientation <110>. Because of capillary action the surface atoms will most commonly be in a state of tension, and the interior atoms will be in a state of compression. To quantify the dependence of this compressive stress state on the position along the ligament, we took slices through the sample perpendicular to the ligament axis 5 nm thick, and calculated the Von Mises and average stress for each slice, only using the interior atoms. The results are plotted in Figure 9.

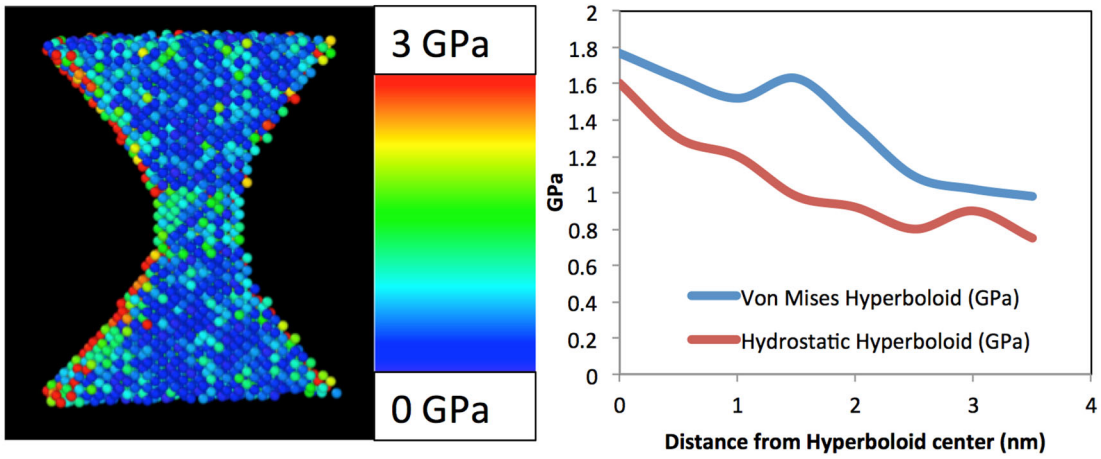

Figure 4-9: Distribution of hydrostatic and von mises stress on the interior atoms of the computational hyperboloid wire prior to any deformation.

There are some residual surface atoms far from the hyperboloid center with high hydrostatic stress, but these residual surface atoms constitute less than 9 percent of the surface, and less than 3 percent of the sample overall, so their effect on the stress averages as a function of distance from hyperboloid center is marginal. The distribution of stresses of individual atoms at the surface is stochastic. Cross sectional averages indicate that the stress is highest at the center. The statistical variation is quite large, meaning that there may be individual atoms with high stresses far from the thinnest point.

As expected, the stresses have a maximum for the thinnest part of the hyperboloid. This demonstrates that the internal ligament stress has a strong local dependence on both the ligament thickness and shape. Consequently, we can expect more brittle failure from ligaments with large morphology variations, as there will be more points in the lattice with these thin, highly stressed regions. In fact, such regions in the lattice where concentrations of high stress are observed can be expected to be where ligaments will usually fail. Given that nanoporous structures are often represented as networks of nanowires, the observation and measurement of these wires' stress state dependence on both orientation and morphology is an important tool for predicting failure locations and mechanisms.

In fact, a ligament was observed to fail in a brittle manner in the experimental sample in a similar manner to the simulated nanowires and hyperboloids. The experimental ligament, shown in Figure 10, formed significant twin or stacking fault defects perpendicular to the strain direction prior to a sudden nanoscale brittle fracture. This behavior was not predicted to occur in individual NPG ligaments, although gold nanowires with twin defects can undergo brittle fracture [31]. Looking at the deformation in our simulated NPG sample, we were able to identify a specific ligament that deformed nearly identically to the ligament observed in the experimental sample, as shown in Figure 10. As the crack tip continued to progress behind it, twin boundaries nucleated perpendicular to the axis of the ligament until failure. The crystalline orientation of this particular ligament was approximately (100), and Figure 10 includes the hyperboloid and cylindrical wire deformation behavior, for comparison.

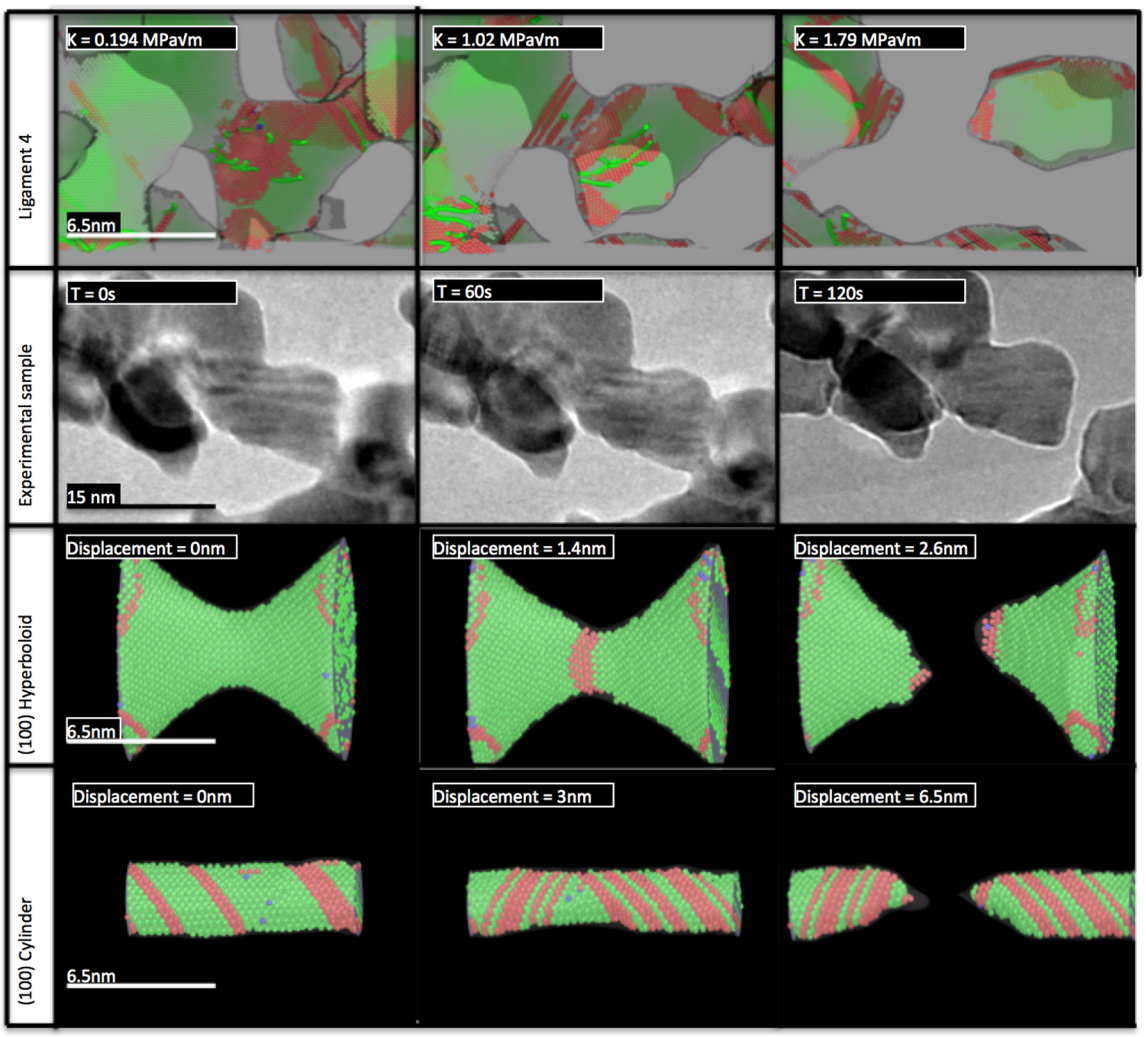

Figure 4-10: Comparison of the failure of a ligament in the experimental sample (top) with that of a ligament in the digital NPG sample (second row) and that of nanowires with hyperboloid (third row) and cylindrical (bottom) shapes.

Hyperboloid wire failure generally occurs at a smaller elongation than the cylindrical wire of the same orientation and minimum diameter. Both crystalline orientation and ligament shape play a major role in the deformation behavior of these nanoporous structures. The comparison shown in Figure 10 shows reasonable agreement between simulation and experiment and indicates that the failure of individual ligaments compares better to that of hyperboloid wires than cylindrical ones. This helps put our results in the context of hyperboloid nanowire deformation.

In fact, TEM analysis showed planar defects approximately perpendicular to the ligament axis, nearly identical to the phenomena observed in the computational sample. This lends credence to the results from individual wires showing that there is a major dependence of failure behavior on crystalline orientation. Even though ligaments in the nanoporous structure are not placed purely in uniaxial tension, the tests performed on the wires and hyperboloids serves a benchmark to show how ligament-by-ligament failure is affected by both morphology and crystalline orientation.

We compared the behavior of the ligaments that failed during deformation of the NPG digital sample to the deformation of nanowires; specifically, the yield and failure points and the maximum ligament elongation. These values are given in Table 2, where we report the failure conditions for the ligaments near the crack tip that are labeled in Figure 11. The observed values depend on the crystallographic orientation of the ligaments and are comparable to those found in the corresponding hyperboloid nanowires, as given in Table 1. Additional visualization of how the different morphologies and orientations of wires deformed is included in videos SV3 to SV10 in the supplemental information section.

4.3.5 Stress development ahead of the crack tip

Our results up to this point indicate that the dominant mechanism of crack propagation is the sequential failure of individual ligaments at the crack tip. To further understand this mechanism, we also analyzed the stress distributions further away from the crack tip. We calculated the Von Mises stress for each atom in the interior of the ligaments, and found that the first ligaments to neck during deformation contained atomic regions with stress values of 1.5 GPa and higher. Before the onset of significant measurable necking, each ligament first had a critical number of atoms with stress higher than 1.5 GPa. Not surprisingly, these high stress regions were most commonly found at the thinnest points in the ligament structure. By mapping individual ligaments that necked and ruptured, we investigated whether stress localization can serve as a predictor of where the ligaments will eventually fracture. Figure 11 shows the evolution of the crack, with ligaments that were observed to fail indicated.

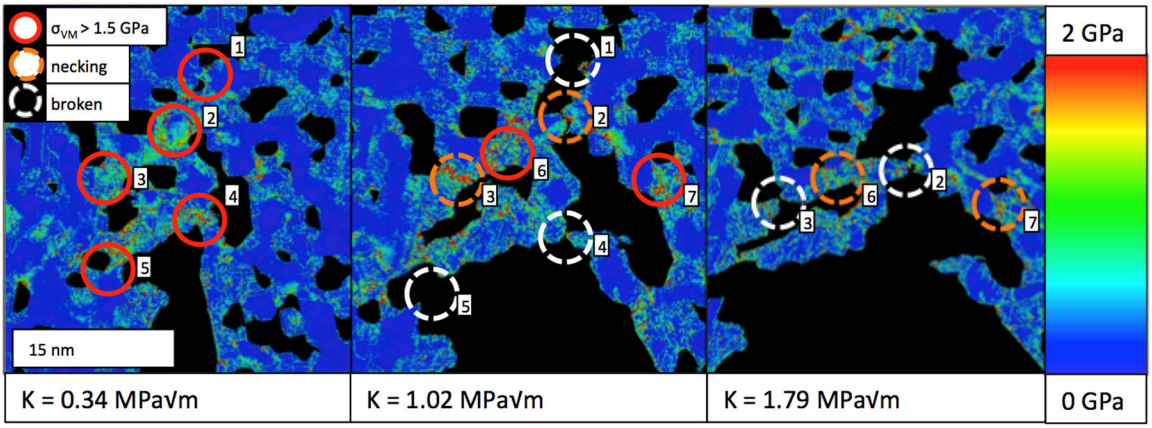

Figure 4-11: Distribution of Von Mises stress around ligaments for different levels of deformation, and the evolution of ligament failure over time. Regions with clusters of atoms with high Von Mises stress are circled in red, and their necking and eventual failure monitored until the end of the simulation. (COLOR ONLINE)

We examined the stress distribution ahead of the crack tip to determine whether this distribution could be linked to the observed ligament failure. By deleting atoms ahead of the crack tip with stresses below 1.5 GPa, we see that early on, the proportion of ligaments with this critical stress is limited to a small area within 5 nm of the crack tip. However, as deformation proceeded, these critical stress regions extended to up to 30 nm around the crack tip, only very roughly resembling the typical shape of a continuum stress field for a Mode I crack. We also looked at the

distribution of total differential atomic displacements ahead of the crack tip. Differential atomic displacements are calculated using the predictions from linear elastic fracture mechanics as a reference, thus the differential displacements indicate deviations from the predictions of linear elastic fracture mechanics, and can be attributed mostly to crack tip plasticity. Figure 12 (a-c) shows the distribution of atoms with Von Mises stresses great than 1.5 GPa. In Figure 12 (d-f) the differential displacement maps are overlaid to the Von Mises stress maps.

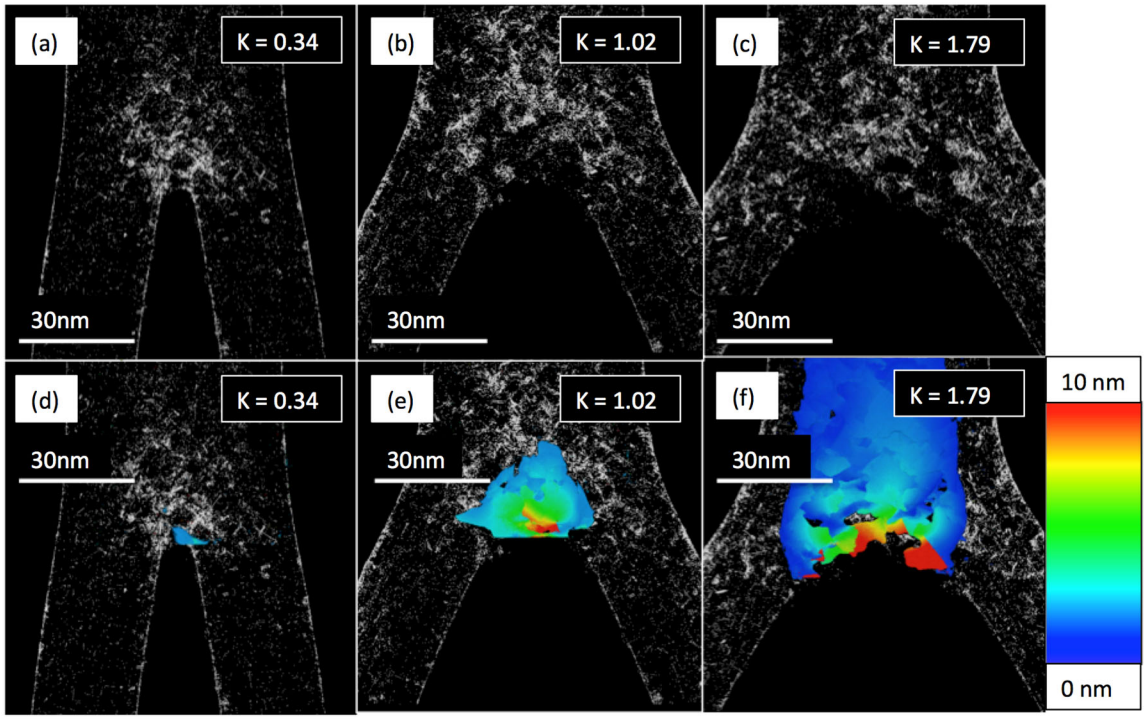

Figure 4-12: Atomic displacement magnitude trends compared with the distribution of Von Mises stress. The top row of images (a-c) show the structure with atoms with an atom-by-atom stress intensity below 1.5 GPa deleted, leaving only highly stressed atoms. The second row (d-f) shows the displacement magnitude profile, corrected for the displacement predictions from linear elastic fracture mechanics, with atoms with a corrected displacement of less than 2 nm having been deleted. (COLOR ONLINE)

The distribution of ligament displacements inside the sample, seen in Figure 12 (d-f) shows that the behavior near the crack tip is significantly different than what is predicted from the continuum solution. This agrees with the experiments, where permanent plastic deformation was observed up to about 100 nm from the crack tip. A relatively large region of the nanoporous structure is stressed around the crack tip during crack propagation. The strain was localized in specific ligaments ahead of the crack, determining the path of the propagating crack. This strong stress localization caused necking and eventual failure of the ligament while many nearby ligaments still presented low strains [60].

4.4. Discussion:

Modeling of fracture in complex materials such as NPG requires accurate atomistic potentials to simulate crack tip progression as well as consideration of the microstructural complexity within

the plastic zone. This includes description of dislocations and their interactions with free surfaces. Multiscale models which combine atomistics with continuum models have already proven their utility for the case of nanocrystals [61]. In this paper we explored the application to nanoporous materials of coupled atomistic modeling of fracture with displacement constraints taken from continuum theory. Molecular dynamics is used to examine the details of crack tip plastic response. The boundary conditions applied in our approach enable us to examine the response to loading, building on the numerical models that have been proposed in continuum and atomistic domains [62, 63]. We have established a linkage between continuum and atomistic techniques by applying linear elastic fracture mechanics methods away from the crack tip, while the tip response was determined by the interatomic potentials used in atomistic simulation, and comparing these results to a purely linear elastic fracture mechanics solution.

The effects of possible additional stresses were not considered in the simulation. We expect that the main effect is due to the stresses due to capillary forces in the nano-sized ligaments, which are included in the simulation. [36][64].

Our simulation does not include grain boundaries. This makes it easier to identify the basic fracture mechanisms that are specific to nanoporous materials, namely the effects of a large amount of free surface and the structure formed by a network of ligaments. Furthermore, intra-granular brittleness is the main issue that needs to be addressed for practical use of these materials. In most cases, the cracks propagate in an intra-granular fashion and the grain boundaries appear irrelevant for the failure [65].

Void-like defects were observed from TEM analysis, and their character and effects on deformation were discussed in a previous paper [60]. Dislocations, stacking faults, twin boundaries, and other plane and line defects were not present in significant amounts. A typical 10 nm diameter ligament often contained 1-2 voids (typically 1-3 nm in diameter) and were often free of other defects, which is not atypical compared to those discussed elsewhere created via the same methodology [66]. We expect that the contribution from these defects specifically on mechanical behavior to be significantly less than the contributions from the large amount of free surface, and they were not included in the simulated sample.

The values of the applied stress intensity K could not be measured with our experimental method and therefore we cannot establish a clear correspondence between K in the simulation and time in the experiments. Crack tip radius can also be used as a metric of correspondence between the experimental and computational samples. As Figure 5 shows, the tip radius of curvature in the simulated sample reaches about 3.5 nm. Snapshots from the experimental sample show radii of curvature reaching about 10nm. Considering that ligaments in the experimental sample were on average around twice the diameter and length of ligaments from the computational sample, we can say that the behavior of these samples was comparable.

We can't easily separate the role of individual deformation modes (such as torsion, shear, and tension) in crack tip propagation. We can say that lattice warping and mismatch (see Figure 8) point to a degree of torsion, consistent with the conclusions by Jiao and Huber [41] that greater disorder and randomness in the morphology would lead to torsion being a greater contributing mechanism. Ligaments that were observed to fail undergo significant tension prior to fracture,

and tension is a good baseline for understanding mechanical behavior in the context of simulated nanowire deformation.

Because the crack tip region is treated in a fully atomistic manner, our simulations take into account the effects of the large amount of free surface that is present in NPG. A limitation of our method is that surface condition effects such as oxidation are not included in our simulations. Another common limitation of atomistic simulations is the very fast time scales. In this regard, we point out that Badwe [67] did not find significant effects of oxidation state in the fracture response of nanoporous samples. Sun et al [68] found that NPG structures can support crack propagation at speeds of over 100 m/s. This can be compared with the rates of crack advance used in our present simulations, which are about 1 m/s. That means that the crack velocities given by our simulation method are not unrealistically fast, compared with experiments. On the contrary, they are slower than those found in dynamic crack experiments.

Using currently available computational resources, the sample and deformation method presented in this paper can replicate experimentally observed fracture mechanisms. Our computations show morphology changes around the tip that are similar to those in an experimental sample being deformed under similar conditions. Video 2 in the supplemental information can be compared directly to supplemental video 2 in the study conducted by Stuckner et al. [69] which has greater detail on the same experimental sample studied in this paper. The general fracture behavior was morphologically comparable, and the mechanisms of that failure were practically identical.

Tip advancement is very non-uniform, depending on the location along the crack front, and the failure of ligaments (the primary method of crack tip advancement) seems to be dependent on the size, orientation, and shape of the ligaments in the initial morphology.

Our results indicate that crack front propagation in nanoporous gold can be understood in the context of individual nanowire deformation (see Tables 1 and 2). We have shown that orientation and morphology can play a critical role in the stress and elongation observed at fracture. We have also observed that depending on the crystallographic orientation, deformation behavior was subtly different from sample to sample. Most wires and hyperboloids will form single atom bridges after twin boundary formation and dislocation nucleation from the surface, but the energy and strain needed to do so seems to vary among different orientations and morphologies, as evidenced by the deformation response (supplemental Figures S1 and S2). The differences among orientation morphologies can be seen in Videos 3-10 in the supplemental information. Most nanowire studies report similar behavior in both simulations [70-72] and experimental work [73-76]. These studies include various orientations [71, 77, 78]. Effects of wire diameter have also been studied [79, 80].

Besides agreement with experiments described here, our simulation results agree very well with other experimental studies. Biener, Hamza and Hodge [81] examined fracture surfaces of NPG and showed macroscopically brittle fracture. However, other experimental studies showed that during tensile deformation, ligaments can fracture through plastic instability but the strain is typically confined to the ligaments located in the propagation direction of the crack. Brittle fracture in heavily deformed individual ligaments has been observed in several studies. For

example, Briot et al. reported very low fracture toughness in agreement with the macroscopic brittleness of nanoporous gold, but found that this is due to the localization of deformation to a narrow zone of ligaments, which individually exhibit significant plasticity and necking [82]. Liu and co-workers reported in situ observations of the deformation and failure of dealloyed nanoporous gold by utilizing the state-of-the art aberration-corrected transmission electron microscopy and fast direct electron detection camera [24]. Our present study is consistent with their results regarding the plastic instability (necking) in individual ligaments. We observe twin and stacking fault formation that is nearly identical to what they recorded experimentally. Specifically, SV1 in our supplementary information shows nanotwins and stacking faults formed by partial dislocations that are nearly identical to what they have observed, despite our samples having a smaller average ligament diameter. Figures 12 and 8 from their paper [24] can be directly compared with (a) ligament failure and (b) twin formation in SV1 and Figure 7c, and Figure 8, (d-f) respectively. Ligament thinning in our sample leads to the formation of single atom bridges, which is exactly what they observe. It is possible that this continuous dislocation nucleation and annihilation at opposite surface causes the plastic instability. This provides additional support for the ability of our simulation method to replicate experimental results.

In addition to the qualitative comparison, while the critical stress intensity (K) was not measured experimentally in the preset work, two studies conducted independently by Sun et al. [68] and Briot et al. [82] report measured static stress intensity values of 0.2 MPa$\sqrt{}$m, and 0.16 MPa$\sqrt{}$m. These are in agreement with the critical stress tip intensity of 0.2 MPa$\sqrt{}$m found for our sample.

4.5. Conclusions:

We have shown in this study that experimental fracture of nanoporous gold can be replicated with reasonable accuracy in a parallel molecular dynamics computing environment. The overall sample failure is given by the failure of individual ligaments. We have shown that ligament strength is highly dependent on orientation and morphology, and that the progression of ligaments that fail can be determined by the internal stress distribution. Both experiments and simulations show that the crack front in nanoporous gold advances by weakening the ligaments ahead of the tip that eventually neck and fail explaining why sudden, brittle fracture is commonly observed. The computed critical stress intensity agrees well with experimental values, representing macroscopically brittle behavior while large deformation is observed in individual ligaments in the crack tip region.

4.6 Acknowledgements

This work was supported by the National Science Foundation, DMREF program, numbers 1533969 and 1533557. The authors acknowledge of the resources of the Virginia Tech Advanced Research Computing Center, and the Nanoscale Characterization and Fabrication Laboratory at Virginia Tech.

4.7 References:

[1] K. Hu, D. Lan, X. Li, S. Zhang, Electrochemical DNA biosensor based on nanoporous gold electrode and multifunctional encoded DNA-Au bio bar codes, Analytical Chemistry 80(23) (2008) 9124-9130.
[2] J. Biener, a. Wittstock, L.a. Zepeda-Ruiz, M.M. Biener, V. Zielasek, D. Kramer, R.N. Viswanath, J. Weissmüller, M. Bäumer, a.V. Hamza, Surface-chemistry-driven actuation in nanoporous gold, Nature materials 8(1) (2009) 47-51.
[3] Z. Liu, J. Du, C. Qiu, L. Huang, H. Ma, D. Shen, Y. Ding, Electrochemical sensor for detection of p-nitrophenol based on nanoporous gold, Electrochemistry Communications 11(7) (2009) 1365-1368.
[4] F. Meng, X. Yan, J. Liu, J. Gu, Z. Zou, Nanoporous gold as non-enzymatic sensor for hydrogen peroxide, Electrochimica Acta 56(12) (2011) 4657-4662.
[5] C. Anders, E.M. Bringa, H.M. Urbassek, Sputtering of a metal nanofoam by Au ions, Nuclear Instruments and Methods in Physics Research Section B: Beam Interactions with Materials and Atoms 342 (2015) 234-239.
[6] C.J. Ruestes, C. Anders, E.M. Bringa, H.M. Urbassek, Nanoindentation tests of heavy-ion-irradiated Au foams—molecular dynamics simulation, J. Appl. Phys. 123(22) (2018) 225903.
[7] C. Anders, E.M. Bringa, H.M. Urbassek, Crater production by energetic nanoparticle impact on Au nanofoams, Appl. Phys. Lett. 108(11) (2016) 113108.
[8] K. Mohan, N. Shahane, R. Liu, V. Smet, A. Antoniou, A Review of Nanoporous Metals in Interconnects, JOM 70(10) (2018) 2192-2204.
[9] V. Zielasek, B. Jürgens, C. Schulz, J. Biener, M.M. Biener, A.V. Hamza, M. Bäumer, Gold catalysts: Nanoporous gold foams, Angewandte Chemie - International Edition 45(48) (2006) 8241-8244.
[10] K.M. Kosuda, A. Wittstock, C.M. Friend, M. Bäumer, Oxygen-mediated coupling of alcohols over nanoporous gold catalysts at ambient pressures, Angewandte Chemie - International Edition 51(7) (2012) 1698-1701.
[11] J. Snyder, T. Fujita, M.W. Chen, J. Erlebacher, Oxygen reduction in nanoporous metal-ionic liquid composite electrocatalysts, Nature materials 9(11) (2010) 904-7.
[12] M. Haruta, T. Kobayashi, H. Sano, N. Yamada, Novel Gold Catalysts for the Oxidation of Carbon Monoxide at a Temperature far Below 0 °C, Chemistry Letters 16(2) (1987) 405-408.
[13] N. Gunkelmann, E.M. Bringa, Y. Rosandi, Molecular Dynamics Simulations of Aluminum Foams under Tension: Influence of Oxidation, The Journal of Physical Chemistry C 122(45) (2018) 26243-26250.
[14] N. Abdolrahim, D.F. Bahr, B. Revard, C. Reilly, J. Ye, T.J. Balk, H.M. Zbib, The mechanical response of core-shell structures for nanoporous metallic materials, Philos. Mag. 93(7) (2012) 736-748.
[15] N. Beets, D. Farkas, Mechanical Response of Au Foams of Varying Porosity from Atomistic Simulations, JOM 70(10) (2018) 2185-2191.
[16] C.J. Ruestes, E.M. Bringa, A. Stukowski, J.F. Rodríguez Nieva, G. Bertolino, Y. Tang, M.A. Meyers, Atomistic simulation of the mechanical response of a nanoporous body-centered cubic metal, Scr. Mater. 68(10) (2013) 817-820.
[17] X. Lang, S. Arai, P. Guan, Y. Ishikawa, T. Fujita, N. Tanaka, M. Chen, L. Zhang, A. Hirata, J. Erlebacher, T. Tokunaga, K. McKenna, Y. Yamamoto, Y. Yamamoto, N. Asao, Atomic origins of the high catalytic activity of nanoporous gold, Nature Materials 11(9) (2012) 775-780.
[18] C.A. Volkert, E.T. Lilleodden, D. Kramer, J. Weissmüller, Approaching the theoretical strength in nanoporous Au, Appl. Phys. Lett. 89(6) (2006).

[19] T.J. Balk, C. Eberl, Y. Sun, K.J. Hemker, D.S. Gianola, Tensile and compressive microspecimen testing of bulk nanoporous gold, Jom 61(12) (2009) 26-31.
[20] C.J. Ruestes, D. Farkas, A. Caro, E.M. Bringa, Hardening under compression in Au foams, Acta Mater. 108 (2016) 1-7.
[21] D. Farkas, J. Stuckner, R. Umbel, B. Kuhr, M. J. Demkowicz, Indentation response of nanoporous gold from atomistic simulations, Journal of Materials Research 33 (2018) 1-9.
[22] R. Li, K. Sieradzki, Ductile-brittle transition in random porous Au, Physical Review Letters 68(8) (1992) 1168-1171.
[23] N. Badwe, X. Chen, K. Sieradzki, Mechanical properties of nanoporous gold in tension, Acta Mater. 129 (2017) 251-258.
[24] P. Liu, X. Wei, S. Song, L. Wang, A. Hirata, T. Fujita, X. Han, Z. Zhang, M. Chen, Time-resolved atomic-scale observations of deformation and fracture of nanoporous gold under tension, Acta Mater. 165 (2019) 99-108.
[25] W.C. Li, T.J. Balk, Effects of substrate curvature on dealloying of nanoporous thin films, Scr. Mater. 61(12) (2009) 1125-1128.
[26] J. Biener, A.M. Hodge, A.V. Hamza, Microscopic failure behavior of nanoporous gold, Appl. Phys. Lett. 87(12) (2005) 1-3.
[27] R. Dou, B. Derby, Deformation mechanisms in gold nanowires and nanoporous gold, Philos. Mag. 91(7-9) (2011) 1070-1083.
[28] R. Liu, A. Antoniou, A relationship between the geometrical structure of a nanoporous metal foam and its modulus, Acta Materialia 61(7) (2013) 2390-2402.
[29] R. Liu, J. Gruber, D. Bhattacharyya, G.J. Tucker, A. Antoniou, Mechanical properties of nanocrystalline nanoporous platinum, Acta Materialia 103 (2016) 624-632.
[30] R. Liu, S. Pathak, W.M. Mook, J.K. Baldwin, N. Mara, A. Antoniou, In situ frustum indentation of nanoporous copper thin films, International Journal of Plasticity 98 (2017) 139-155.
[31] Y. Lu, J. Song, J.Y. Huang, J. Lou, Fracture of Sub-20nm Ultrathin Gold Nanowires, Advanced Functional Materials 21(20) (2011) 3982-3989.
[32] J. Biener, A.M. Hodge, J.R. Hayes, C.A. Volkert, L.A. Zepeda-Ruiz, A.V. Hamza, F.F. Abraham, Size Effects on the Mechanical Behavior of Nanoporous Au, Nano Letters 6(10) (2006) 2379-2382.
[33] N.J. Briot, T.J. Balk, Developing scaling relations for the yield strength of nanoporous gold, Philos. Mag. 95(27) (2015) 2955-2973.
[34] X.-Y. Sun, G.-K. Xu, X. Li, X.-Q. Feng, H. Gao, Mechanical properties and scaling laws of nanoporous gold, J. Appl. Phys. 113(2) (2013) 023505.
[35] H. Liu, L. He, N. Abdolrahim, Molecular dynamics simulation studies on mechanical properties of standalone ligaments and networking nodes, a connection to nanoporous material, Model. Simul. Mater. Sci. Eng. 26(7) (2018) 075001.
[36] N. Beets, D. Farkas, S. Corcoran, Deformation mechanisms and scaling relations in the mechanical response of nano-porous Au, Acta Materialia 165 (2019) 626-637.
[37] L.J. Gibson, M.F. Ashby, The Mechanics of Three-Dimensional Cellular Materials, Proceedings of the Royal Society of London. Series A, Mathematical and Physical Sciences 382(1782) (1982) 43-59.
[38] B. Roschning, N. Huber, Scaling laws of nanoporous gold under uniaxial compression: Effects of structural disorder on the solid fraction, elastic Poisson's ratio, Young's modulus and yield strength, Journal of the Mechanics and Physics of Solids 92 (2016) 55-71.

[39] N. Mameka, K. Wang, J. Markmann, E.T. Lilleodden, J. Weissmüller, Nanoporous Gold—Testing Macro-scale Samples to Probe Small-scale Mechanical Behavior, Mater. Res. Lett 4(1) (2016) 27-36.
[40] K. Hu, M. Ziehmer, K. Wang, E.T. Lilleodden, Nanoporous gold: 3D structural analyses of representative volumes and their implications on scaling relations of mechanical behaviour, Philos. Mag. 96(32-34) (2016) 3322-3335.
[41] J. Jiao, N. Huber, Deformation mechanisms in nanoporous metals: Effect of ligament shape and disorder, Comput. Mater. Sci. 127 (2017) 194-203.
[42] G. Cao, J. Wang, K. Du, X. Wang, J. Li, Z. Zhang, S.X. Mao, Superplasticity in Gold Nanowires through the Operation of Multiple Slip Systems, Advanced Functional Materials 28(51) (2018) 1-8.
[43] H. Zheng, A. Cao, C.R. Weinberger, J.Y. Huang, K. Du, J. Wang, Y. Ma, Y. Xia, S.X. Mao, Discrete plasticity in sub-10-nm-sized gold crystals, Nature Communications 1 (2010) 144.
[44] A. Latapie, D. Farkas, Molecular dynamics investigation of the fracture behavior of nanocrystalline α-Fe, 2004.
[45] D. Farkas, H. Van Swygenhoven, P.M. Derlet, Intergranular fracture in nanocrystalline metals, Physical Review B 66(6) (2002) 060101.
[46] D. Farkas, S. Van Petegem, P.M. Derlet, H. Van Swygenhoven, Dislocation activity and nano-void formation near crack tips in nanocrystalline Ni, Acta Mater. 53(11) (2005) 3115-3123.
[47] V. Shastry, D. Farkas, Molecular statics simulation of fracture in -iron, Model. Simul. Mater. Sci. Eng. 4(5) (1996) 473-492.
[48] D. Farkas, Fracture Resistance of Nanocrystalline Ni, Metallurgical and Materials Transactions A 38(13) (2007) 2168-2173.
[49] K. Kolluri, M.J. Demkowicz, Coarsening by network restructuring in model nanoporous gold, Acta Mater. 59(20) (2011) 7645-7653.
[50] A.C. To, S. Li, Perfectly matched multiscale simulations, Physical Review B 72(3) (2005) 035414.
[51] B.-N.D. Ngô, A. Stukowski, N. Mameka, J. Markmann, K. Albe, J. Weissmüller, Anomalous compliance and early yielding of nanoporous gold, Acta Mater. 93 (2015) 144-155.
[52] D.A. Crowson, D. Farkas, S.G. Corcoran, Mechanical stability of nanoporous metals with small ligament sizes, Scripta Materialia 61(5) (2009) 497-499.
[53] D.A. Crowson, D. Farkas, S.G. Corcoran, Geometric relaxation of nanoporous metals: The role of surface relaxation, Scr. Mater. 56(11) (2007) 919-922.
[54] S. Plimpton, Fast Parallel Algorithms for Short-Range Molecular Dynamics, Journal of Computational Physics 117(1) (1995) 1-19.
[55] S.M. Foiles, M. I. Baskes, M. Daw, Embedded-atom-method functions for the fcc metals Cu, Ag, Au, Ni, Pd, Pt, and their alloys, 1986.
[56] A. Stukowski, Visualization and analysis of atomistic simulation data with OVITO–the Open Visualization Tool, Modeling and Simulation in Materials Science and Engineering 18(015012) (2009).
[57] J. Erlebacher, M.J. Aziz, a. Karma, N. Dimitrov, K. Sieradzki, Evolution of nanoporosity in dealloying, Nature 410(6827) (2001) 450-453.
[58] J. Stuckner, K. Frei, I. McCue, M.J. Demkowicz, M. Murayama, AQUAMI: An open source Python package and GUI for the automatic quantitative analysis of morphologically complex multiphase materials, Computational Materials Science 139 (2017) 320-329.

[59] S. Koh, H. Lee, Molecular dynamics simulation of size and strain rate dependent mechanical response of FCC metallic nanowires, 2006.
[60] J. Stuckner, M. Murayama, Mechanical properties of nanoporous gold subjected to tensile stresses in real-time, sub-microscopic scale, Journal of Materials Science (2019).
[61] G. Bertolino, M. Ruda, D. Farkas, Fracture resistance of textured polycrystalline Zr: A simulation study, Computational Materials Science 162 (2019) 304-313.
[62] S.J. Zhou, D.M. Beazley, P.S. Lomdahl, B.L. Holian, Large-scale molecular dynamics simulations of three-dimensional ductile failure, Physical Review Letters 78(3) (1997) 479-482.
[63] M.J. Buehler, A. Hartmaier, H.J. Gao, M. Duchaineau, F.F. Abraham, Atomic plasticity: description and analysis of a one-billion atom simulation of ductile materials failure, Computer Methods in Applied Mechanics and Engineering 193(48-51) (2004) 5257-5282.
[64] J. Weissmüller, H.L. Duan, D. Farkas, Deformation of solids with nanoscale pores by the action of capillary forces, Acta Mater. 58(1) (2010) 1-13.
[65] N. Mameka, K. Wang, J. Markmann, E. Lilleodden, J. Weissmüller, Nanoporous Gold—Testing Macro-scale Samples to Probe Small-scale Mechanical Behavior, 2015.
[66] H. Rösner, S. Parida, D. Kramer, C.A. Volkert, J. Weissmüller, Reconstructing a Nanoporous Metal in Three Dimensions: An Electron Tomography Study of Dealloyed Gold Leaf, Advanced Engineering Materials 9(7) (2007) 535-541.
[67] N. Badwe, Fracture of Nanoporous Gold, Materials Science and Engineering, Arizona State University, Arizona State University, 2014, p. 111.
[68] S.F. Sun, X.Y. Chen, N. Badwe, K. Sieradzki, Potential-dependent dynamic fracture of nanoporous gold, Nature Materials 14(9) (2015) 894-+.
[69] J. Stuckner, M. Murayama, Mechanical properties of nanoporous gold subjected to tensile stresses in real-time, sub-microscopic scale, Journal of Materials Science 54(18) (2019) 12106-12115.
[70] H. Park, W. Cai, D. Horacio, H. Huang, Mechanics of Crystalline Nanowires, MRS bulletin / Materials Research Society 34 (2009) 178.
[71] H.S. Park, K. Gall, J.A. Zimmerman, Deformation of FCC nanowires by twinning and slip, Journal of the Mechanics and Physics of Solids 54(9) (2006) 1862-1881.
[72] H. Park, J. Zimmerman, Modeling Inelasticity and Failure in Gold Nanowires, Physical Review B 72 (2005) 054106.
[73] E.Z. da Silva, A.J.R. da Silva, A. Fazzio, How do gold nanowires break?, Physical Review Letters 87(25) (2001).
[74] V. Rodrigues, D. Ugarte, Real-time imaging of atomistic process in one-atom-thick metal junctions, Physical Review B 63(7) (2001).
[75] Y. Lu, J. Song, J. Huang, J. Lou, Surface dislocation nucleation mediated deformation and ultrahigh strength in sub-10-nm gold nanowires, Nano Research 4 (2011) 1261-1267.
[76] D. Kong, S. Sun, T. Xin, L. Xiao, X. Sha, L. Yan, S. Mao, J. Zou, L. Wang, X. Han, Reveal the size effect on the plasticity of ultra-small sized Ag Nanowires with in situ atomic-scale microscopy, Journal of Alloys and Compounds 676 (2016).
[77] H.S. Park, W. Cai, H.D. Espinosa, H.C. Huang, Mechanics of Crystalline Nanowires, Mrs Bulletin 34(3) (2009) 178-183.
[78] G. Yun, H.S. Park, Surface stress effects on the bending properties of fcc metal nanowires, Physical Review B 79(19) (2009).
[79] F.Y. Wang, Y.F. Dai, J.W. Zhao, Q.J. Li, B. Zhang, Effect of size on fracture and tensile manipulation of gold nanowires, J. Nanopart. Res. 16(12) (2014) 12.

[80] F.Y. Wang, Y.F. Dai, J.W. Zhao, Q.J. Li, Uniaxial tension-induced fracture in gold nanowires with the dependence on size and atomic vacancies, Physical Chemistry Chemical Physics 16(45) (2014) 24716-24726.
[81] J. Biener, A.M. Hodge, A.V. Hamza, Microscopic failure behavior of nanoporous gold, Applied Physics Letters 87(12) (2005) 121908.
[82] N.J. Briot, T. Kennerknecht, C. Eberl, T.J. Balk, Mechanical properties of bulk single crystalline nanoporous gold investigated by millimetre-scale tension and compression testing, Philosophical Magazine 94(8) (2014) 847-866.

Chapter 5: The Mechanical Response of Nanoporous Gold and Silver Lattices with Varying Alloy Compositions and Surface Segregations

Nathan Beets[1]*, Diana Farkas[1], Karsten Albe[2]

1 Department of Materials Science and Engineering, Virginia Tech
Holden Hall, 445 Old Turner St #213, Blacksburg, VA 24060
2 Materials Modeling Division, Technical University of Darmstadt
L1|08 211 Otto-Berndt-Str. 3 64287 Darmstadt

* Corresponding Author.

email: bnathan2@vt.edu

5.0. Abstract:

The mechanical response of a mixed gold and silver lattice is studied via molecular dynamics simulations. The segregation of silver to the surfaces of a nanoporous structure to minimize energy are studied and characterized with a variance constrained, Monte Carlo simulation scheme. Dislocation evolution in alloyed and pure elemental structures is analyzed. The yield response of the material is investigated in the context of an existing theoretical model that predicts yield stress based on a surface term.

5.1. Introduction:

Nanoporous gold (NPG) is an open cellular material made up of nanoscale interconnected ligaments and pores, which has received widespread interest in the scientific community due to its unique physical properties [1-11]. The structure of this material, which can be approximated by a series of randomly-oriented nanowires connected at nodes, has a high surface area to volume ratio which, when combined with the unique mechanical and chemical properties of gold nanowires, allows for many interesting applications, such as actuation[12-16], catalysis [17, 18], and sensing [19, 20].

NPG is created via electro-chemical dealloying, whereby a parent alloy of mixed gold/silver leaf is submerged in an acidic electrolyte bath at a certain temperature and voltage for a certain amount of time; typically in the range of minutes to hours with temperature ranges from 300-500 K [21-23]. Gold/silver leaf is widely used in part because it is a miscible system that, when synthesized properly, will have a perfect random mixture of gold and silver atoms with no phase separation or miscibility gap [24]. Furthermore, gold and silver have distinctly different oxidation energies, so when submerged in an acid bath of a particular concentration, the element with the lower oxidation energy will leach away slowly, leaving behind a fully connected porous structure. This process has been replicated computationally via kinetic Monte Carlo methods [12].

Because this method uses simple, low cost materials, and can be done at room (or slightly elevated) temperature, it is very attractive from a synthesis standpoint. Aspects of the morphology such as ligament diameter, connectivity, and solid volume fraction can be controlled through calculation of the potential, electrolyte composition, and various post-processing treatments, such as annealing [25-28]. Furthermore, this method preserves the grain structure and orientation of the parent alloy after dealloying [29].

Mechanical properties, specifically the relation of structure connectivity, ligament diameter, volume fraction, and capillary effects from the free surface to the mechanical response have been studied previously [1, 7, 9, 22, 30-35]. These studies have universally shown that nanoporous structures are brittle in tension, but ductile in compression, distinctly different from the uniformly ductile mechanical behavior of bulk polycrystalline Au. The reason for this behavior and the subsequent weakening of the material has been studied in the context nanowire mechanics with great success. Indeed, it has been shown that the mechanical behavior of this material can be best understood as a network or "forest" nanowires. [11, 36-38] It has also been shown that the surface tension, and the additional stress that is introduced in the lattice because of the resulting capillary forces, plays a major role in mechanical behavior of individual ligaments and by extension, of the entire lattice [9, 31]

However, very little has been done to understand the effect of adding alloying elements to the nanoporous lattice – specifically, the effect of the addition of silver. And while a careful dealloying procedure will leave behind a primarily gold lattice, there will inevitably be some silver left behind [39]. Most of the systems that have been studied thus far have only considered pure elemental systems with no alloying components. One paper by Hodge et. al from 2009 studied the concentration of residual silver in a nanoporous gold lattice, and characterized its effects on the mechanical properties [40]. Beyond this, little has been done to understand the effects that addition of silver has on the mechanical properties of nanoporous lattice, and how chemical segregation within the lattice affects surface tension, yielding, lattice mismatch in the bulk, and dislocation behavior.

Fortunately, the effect of alloying elements on the mechanical behavior on polycrystalline systems has been studied [41-44]. Thanks to the work done to understand the mechanics and thermodynamics of nanocrystaline alloy systems, we can make a well educated guess on the effect of alloying elements on the mechanical properties of our ideal nanoporous lattice. In conjunction with our theoretical understanding of the mechanical behavior of nanoporous lattices, and the effects of the surface on mechanical behavior, we can have a decent idea of how these samples should behave with the addition of silver into the lattice, which we can test with molecular dynamics simulations.

This study will utilize molecular dynamics along with a Monte Carlo sampling algorithm to characterize the effect that the addition of silver, both in a random atomic placement, as well as in a chemically separated placement has on the mechanical behavior of these lattices. The effects that this addition and reorganization has on general elastic properties, surface tension, and lattice and dislocation structure will all be examined. We will conclude by fitting the gathered mechanical data to an analytical model for the yield stress, and show how the yielding of nano-structured miscible systems can be understood in the context of a surface contribution term.

5.2. Methods:

To generate a nanoporous gold structure, we used a modified version of the Cahn Hilliard equations to create a fully separated three-dimensional binary phase field. This is the same method used by Crowson et al [8, 45] and has been shown to accurately replicate nanoporous structures recreated from nuclear magnetic resonance scans, in terms of ligament aspect ratio and diameter variation. The details of how this method was used to create our specific morphology are covered in section 3.1. All visualization, dislocation analysis, and surface energy/stress analysis was done with the OVITO software package [46].

Our goal with this project was to understand nanoscale mechanical properties of an alloyed material in the context of our understanding of the overall mechanical behavior of both pure silver and gold structures. So, to create a nearly identical silver lattice, we simply rescaled the structure to have a lattice parameter of 4.09, and labeled these "Ag atoms." To create a sample with mixed gold and silver atoms, we used a random number generator that sampled over a Bernoulli distribution weighted to give us 38% Au, and 62% Ag throughout the atoms in the lattice. The lattice parameter was also altered to reflect this change, going from 4.08 nm to 4.0833 nm. Two other samples were also created using the same base structure, both with mixed alloy compositions of 38% Ag. How and why these additional samples were created will be covered in section 2.2 and 3.1.

For this study, we also wanted to look at the effects that elemental segregation have on the mechanical properties of the structure. For some alloy systems, atoms preferentially segregate to the surface, usually during post-processing procedures at elevated temperatures that can lead to higher diffusion rates [47] [41-44]. This preferential segregation in the alloy structure can lead to differences in the mechanical properties by changing the gamma surface and dislocation nucleation energy of a material at it's surface or interface, and of course, by changing the structure and energy of said interface.

The Variance-Constrained Semi Grand Canonical Ensemble offers a sampling environment to study chemical segregation, because it allows one to set the chemical potential and potential difference for a mixed elemental system, and use Monte Carlo methods to sample the positions of atoms with different elemental identities, until the lowest energy state is found. A paper written by Sadigh et al. provides the details of the process that calculates ensemble energy with minimization and an interatomic potential which can efficiently sample several thousand steps over a structure with several million atoms [48]. It has been integrated as a fix in LAMMPS. We use this method (abbreviated form here as VC-SGCMC) in conjunction with the structure generated and the selected interatomic potentials to see how the mixed structure preferentially relaxes at a given temperature, defined composition, and chemical potential difference.

To simulate forces on these atoms, we used the interatomic potential functions from the 1986 paper by Foiles and Baskes. [49] The interaction of the two interatomic potentials was accomplished via arithmetic mixing [50]. The way these potentials and their mixture were thermodynamically validated will be covered in section 3.1.

To simulate mechanical behavior of the generated lattices, the LAMMPS molecular dynamics package was used [51]. All dynamic deformation simulations were run in the NPT thermodynamic ensemble, and temperature and pressure were controlled with a noose-hoover thermostat and barostat. All VC-SGCMC simulations were run in the NVT ensemble, by necessity of the algorithm mechanics. All samples were simulated at 300K, and the pressure on the non-deforming sides was held at zero.

A key component of this study was the generation of equilibrated, low energy structures with consistent atomic concentration. Slow chemical dealloying processes will naturally allow for diffusion-based segregation, but since this process can take minutes to hours in real time, modeling this diffusion using traditional large-scale molecular dynamics is not possible. Monte Carlo methods, however, provide an efficient way to sample different atom configurations in a structure while keeping the concentration of that structure constant. These methods swap atom identities, and calculate energies associated with particular configurations via integration with the LAMMPS NVT ensemble and a predefined structure. To calculate the average energy of a structure of a particular concentration analytically, one would need to evaluate the function:

$$\langle U\rangle = \frac{1}{Z_{NVT}} \int e^{-U(r^N)/k_b T} U(r^N) dr^N \quad [1]$$

Wherein Z_{NVT} is commonly described as the partition function, written as;

$$Z_{NVT} = \int e^{-U(r^N)/k_b T} dr^N \quad [2]$$

and the term dr^N can be described as…

$$dr^N = dx_1 dy_1 dz_1 dx_2 dy_2 dz_2 \ldots dx_N dy_N dz_N \quad [3]$$

Calculating the value of <U> and Z analytically is practically impossible, but by sampling different configurations and calculating their energy, one can get a reasonable estimate of the form of Z, and the value of <U> for various systems. A configuration sample structure in LAMMPS can be produced by multiple methods, but in the basic metropolis Monte Carlo algorithm, this works by holding positions and relative concentrations constant, but swapping atom identities, for a binary or multi-component system. After a swap, the energy of the structure is determined by the ensemble (NVT, in this case) and the assigned interatomic potential. The swap probability (pi+1) is determined by the following:

$$\frac{p_{i+1}}{p_i} = exp\left(\frac{-\Delta E_{i,i+1}}{k_b T}\right) \quad [4]$$

Whether a trial is accepted or not depends on

$$\Delta E_{i,i+1} = \begin{cases} \leq 0, Trial\ accepted \\ > 0, Trial\ accepted\ with\ probability\ exp\left(\frac{-\Delta E_{i,i+1}}{k_b T}\right) \end{cases} \quad [5]$$

The particular swapping process used in this study, described previously by Sadigh et al. [52] uses a semi-grand canonical ensemble, whereby atoms are exchanged with an external particle reservoir at constant chemical potential and temperature. One can hold the concentration, and input a single chemical potential difference term (Δμ) for a binary system, or (n-1) chemical potential difference terms for a system with (n) components. The formalism above will be largely unaltered, but this will introduce a new LaGrange multiplier term, (ΔμNΔc) which describes the driving forces originating from the variation of the concentration, and changes the acceptance probability of the trial move. Again, this allows for some accounting of the chemical potential difference between the two components being considered, with the probability function and partition function given in equations (6) and (7).

$$\frac{p_{i+1}}{p_i} = exp\left(\frac{-(\Delta E_{i,i+1} + \Delta\mu N \Delta c)}{k_b T}\right) \quad [6]$$

$$Z_{NVT}(\Delta\mu) = \int e^{\left(-\frac{\Delta\mu N \Delta c}{k_b T}\right)} dc \quad [7]$$

With this method, we can simulate atomic segregation with thermodynamics consistent with what we could expect for the miscible Au/Ag system.

5.3: Results

5.3.1 Interatomic potential testing, and sample generation:

With a reasonable way to simulate atom diffusion and segregation, it became necessary to find and validate an interatomic potential for the interaction of gold and silver atoms. At the time this paper was written, no reasonable potential for the interaction between gold and silver atoms was available, so we used the two interatomic potentials for gold and silver (respectively) developed by Foiles and Baskes, mentioned previously in section 2.1. To model the interaction between these atoms, the mixing scheme built into LAMMPS was used, which averages the two interatomic potential functions arithmetically. It was important to ensure that the system produced was miscible, so 11 cubical fully periodic samples were created, each containing roughly 32,000 atoms with concentrations varying from 0% to 100% Au, and random placement of atom identities throughout the structure. Each structure was energy-minimized, and total energy per atom was calculated, and plotted as a function of concentration, which can be seen in Figure 1a. The absolute value of the difference between the calculated energy per atom and the linear estimate between the energy values for pure gold and silver, respectively was also calculated. The linear approximation slightly over-estimates the actual energy values, as can be seen in Figure 1b, which plots the absolute value. To see if there was a miscibility gap, we took the derivative of the curve in Figure 1b over the energy per atom vs. concentration graph to get total chemical potential difference, and found that indeed, there were no local maxima or minima, and therefore no miscibility gaps in the energy landscape. This is shown in Figure 1c. This is consistent with the fact that the gold and silver mixture is a miscible system, and therefore, we can reasonably say that we are simulating reality with this interatomic potential combination.

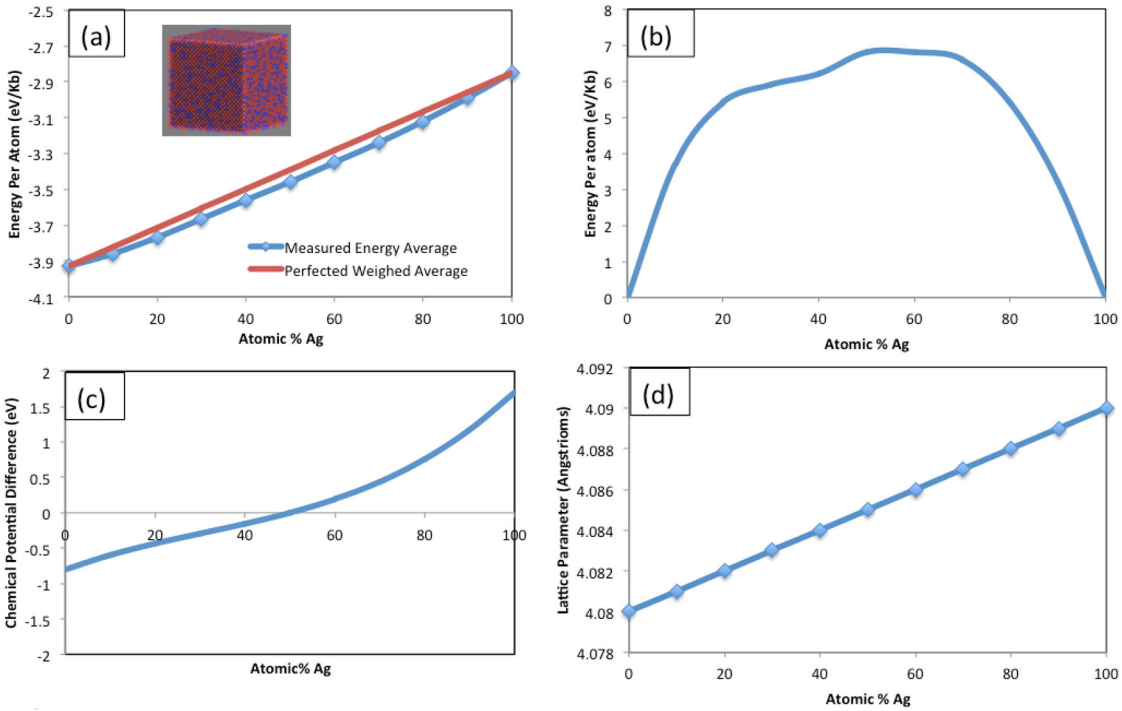

Figure 5-1: Thermodynamic and lattice constant data for the mixed alloy system: (a) Is the energy of the mixed samples with varying concentrations (red) plotted against the perfect weighted energy average between the energy of pure Au and pure Ag, respectively (red). (b) Is the absolute value of the difference of the red and blue curves. (c) is the chemical driving force as a function of composition of the block, showing no miscibility gap. (d) is the lattice parameter plotted against the atomic composition of silver (Ag) for a block with randomly distributed atom identities.

As a final check, we relaxed the cubical samples for 3 picoseconds at 300K in the NPT ensemble, and calculated the average lattice parameter for each structure. As expected, the relationship between concentration and lattice parameter was perfectly linear, going from 4.08 Angstroms for Au up to 4.09 Angstroms for Ag. This relationship is shown in Figure 1d.

We next wanted to create a series of computational samples that could reasonably replicate the structure of a nanoporous lattice. We employed the previously mentioned modification of the Cahn Hilliard Formalism to create a bicontinuous light and dark phase structure, which was fully periodic. After separation, a hard cutoff parameter was defined, to make the structure binary light and dark phase, and the light structure was filled with an FCC lattice of atoms, with [100] crystal faces parallel to cube edges of the periodic box. No additional corrections were made for preferential surface relaxation for certain crystalline faces, because at this particular ligament size, TEM microscopy reveals no preferential surface faceting [22]. The parameters for this simulation were modified so that the sample would have an average ligament diameter of 5.5 nm, well above the stability threshold for this material. The solid volume fraction was 42%, which is in the range for materials of this size where the Gibson-Ashby formalism for Yield Stress can still be reasonably applied [33]. The structure we produced filled a cubical box with dimensions of 48.96 nm × 48.96 nm × 48.96 nm, and a total of 3207225 atoms, in an FCC

crystalline lattice. The initial lattice parameter was 4.08 Angstroms. The surface area to volume ratio was 0.049 (1/m).

The lattice parameter was scaled to match the predicted lattice parameter from Figure 1d. At first, three structures were created, of (a) pure Au, (b) Pure Ag, and (c) a 38% random placement mixture of Ag in a majority Au structure, with lattice parameter adjusted to match. (4.0838 Angstroms). Then, the VC-SGCMC method (outlined in section 2.2) was employed carry out atom segregation, with the modified LaGrange multiplier (i.e, the chemical potential difference, $\Delta\mu$) of 1.08 eV/Atom, and a 38% total composition of Ag. Much silver segregated to the surface of the structure, leaving the internal composition 33% silver, and the external surface composition 66% silver. To delineate the effects of the bulk from the surface, we also created a random placement sample using the same structure with a total composition of 33% Ag, for mechanical testing. In total, this gave us 5 samples, all of which are shown in Figure 2.

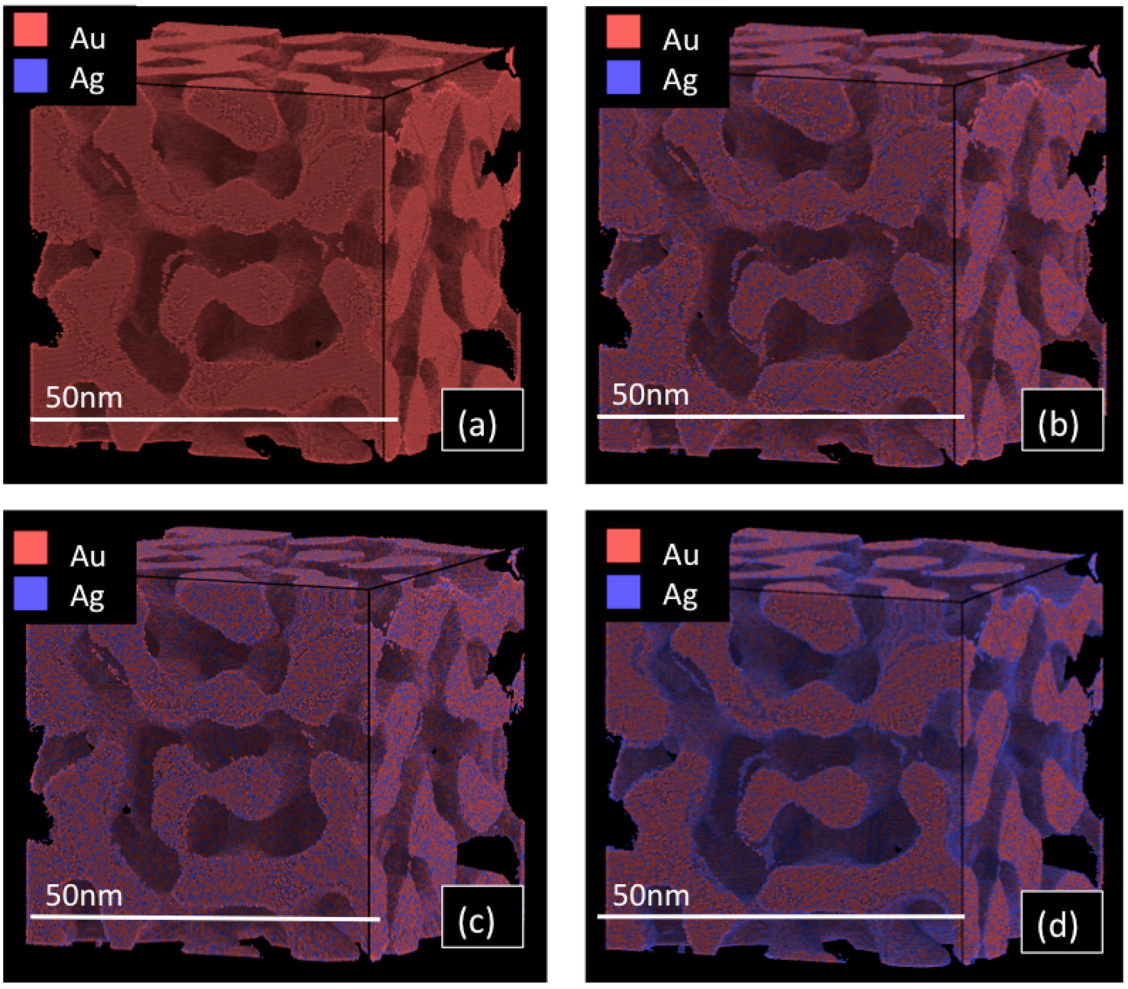

Figure 5-2: Images of our generated nanoporous structure, with different compositions of atoms. (a) is our pure monatomic lattice, used to simulate Au and Ag structures with the correct scaled lattice parameter. (b) is 33 percent Ag, with random atomic distribution. (c) is 38 percent Ag, with random atomic distribution. (d) is the equilibrated sample with overall 38% Ag, and surface composition of 66% Ag.

5.3.2 Relaxation and deformation results.

With the samples generated, we thermally relaxed each for 3 picoseconds at 300K, and then subjected the samples to uniaxial tensile and compressive deformation up to 0.1 strain in the x direction. The NPT thermodynamic ensemble was used, and Poisson contraction and expansion was allowed for the non-deformed sides. Pressure data was gathered from the LAMMPS thermodynamic output, and plotted as a function of strain for all samples. This is shown in Figure 3

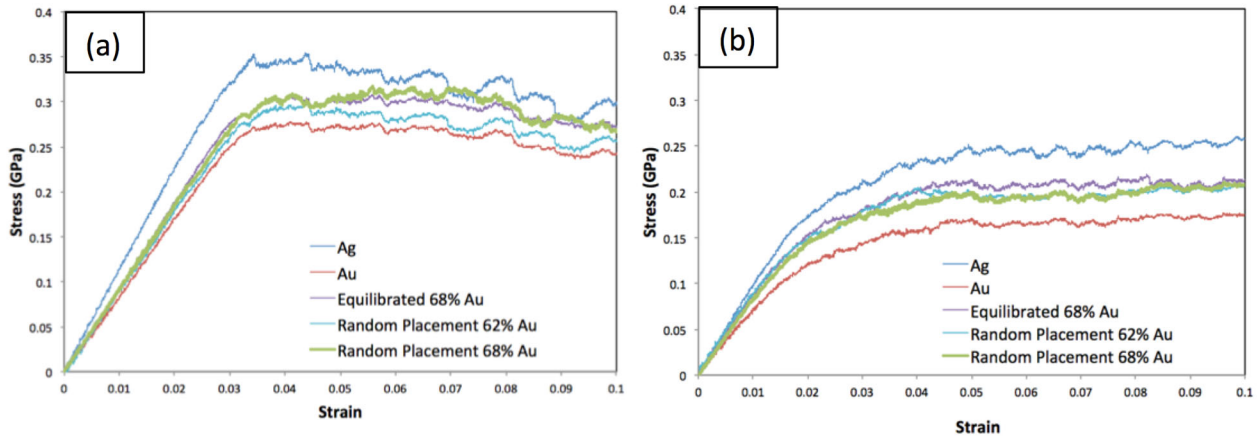

Figure 5-3: Stress/Strain curves for all samples in tension (a), and compression (b)

Yield and elastic modulus data was gathered from theses graphs, and is shown in Table 1.

Table 5-1: Yield Stress and Elastic Modulus data for different alloy compositions

Tension	Elastic Modulus (GPa)	Yield Stress (GPa)
Au	6.36	0.2649
Ag	9.91	0.347
62%Au_NonEquilibriated	7.51	0.295
62%Au_Equlibriated	7.9	0.307
67%Au_NonEquilibriated	7.85	0.312
Compression	Elastic Modulus (GPa)	Yield Stress (GPa)
Au	6.24	0.115
Ag	9.73	0.213
62%Au_NonEquilibriated	8.27	0.149
62%Au_Equlibriated	7.92	0.167
67%Au_NonEquilibriated	7.53	0.166

As expected, the results were significantly lower than what is typically expected for bulk gold and silver respectively, but when these values are compared to results from trans-axial nanowire deformation tests and scaled according to the modified Gibson-Ashby formalism, the values for

gold and silver are reasonable [33, 34]. It should be noted that both materials are elastically anisotropic, and how this affects deformation results in the context of nanowire deformation tests is described in the previous work [33].

The asymmetry in the elastic modulus and plastic response, and how this fits in the context of surface and capillary forces will be discussed in section 3.4

5.3.3 Dislocation behavior

After deformation, we investigated the effect that the addition of silver had on dislocation behavior in the different structures with different atomic compositions. Alloy composition can have a major impact on dislocation travel and overall plastic behavior, as has been observed for high entropy alloys [53]. So, we first calculated gamma surfaces for a [111] crystal face, deforming the sample in the [110] direction, above the first nucleation barrier for a periodic block of pure Au, pure Ag, and a random distribution of 30% Ag in Au. The results are shown in Figure 4:

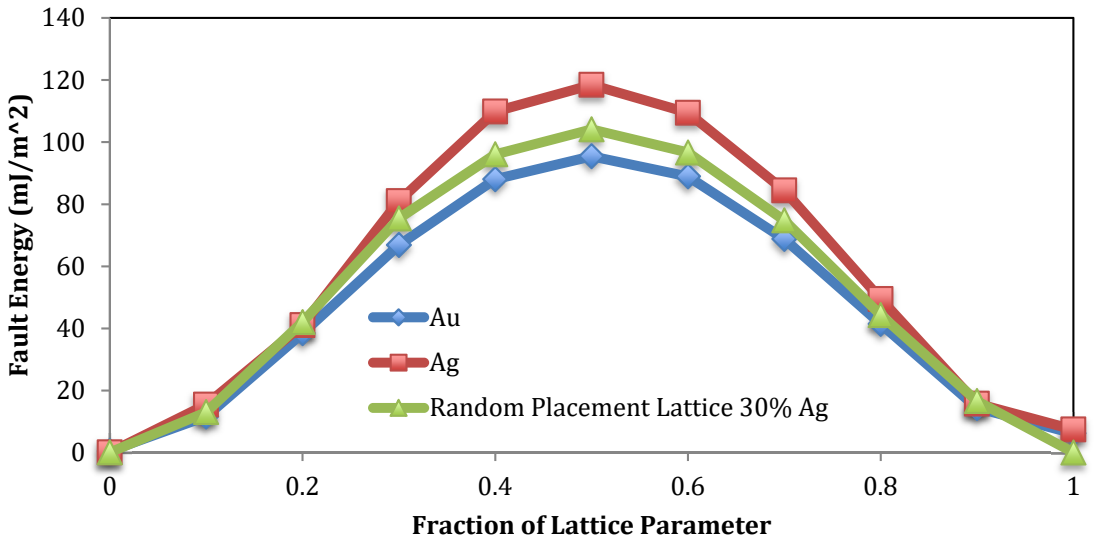

Figure 5-4: Gamma surfaces for Pure Ag, Pure Au, and a mixed block with 70% Au, 30% Ag, with all sampled deformed in the [1-10] direction along the {111} face.

As expected, silver has a higher energy barrier, and gold has a lower barrier, with the mixed alloy falling between the two, exactly where we would expect a 30% composition of silver to lie, according to a weighted average of the two curves.

Using the Dislocation Extraction Algorithm (DXA) included in the OVITO Software package, we were able to track total residual dislocation density as a function of both strain and alloy composition, specifically for samples undergoing compression, which is shown in Figure 5.

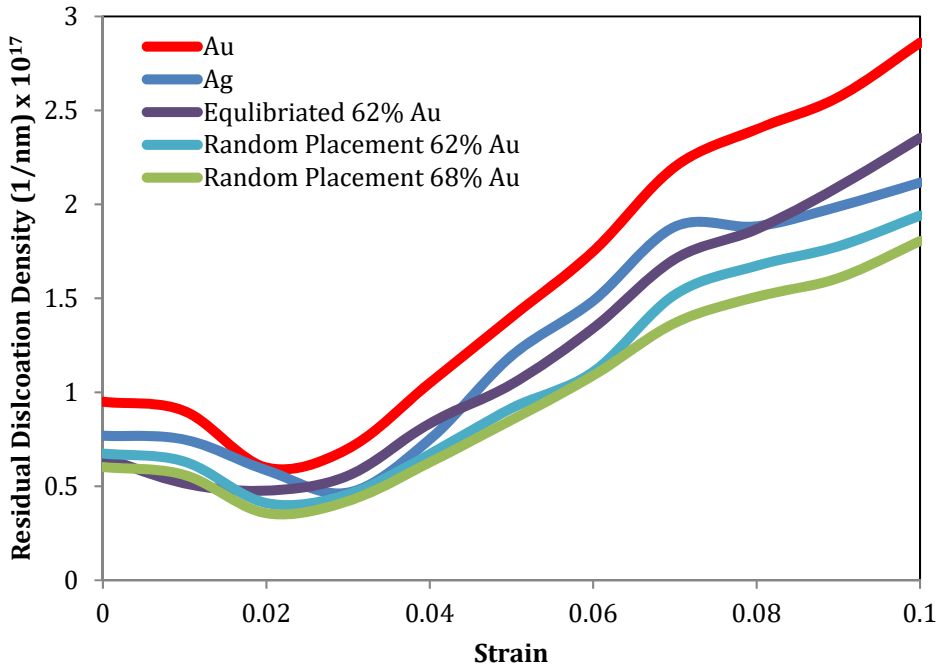

Figure 5-5: Residual dislocation densities for all samples in compression.

Non-zero residual dislocation densities are common for this kind of material after an initial thermal relaxation. No significantly unusual behavior was observed, and the residual dislocation densities for gold and silver are consistent with what one would expect from the gamma surfaces, and from what has been observed from previous work. However, the fact that dislocation density for all alloy structures are somewhat lower than either of the pure elemental samples suggests that there is some kind of activation barrier to nucleation that is dependent on surface concentration or bulk concentration, or both. This will be examined in the discussion section.

Looking at the structure itself during compression, we identified nucleation sites in the lattice, and found that independent of concentration, dislocations seemed to nucleate from the same part of the structure at roughly the same time. For the pure Au and Ag samples, and for the equilibrated and non equilibrated random placement sample, dislocations nucleated from the same steps on the surface at the same highly curved parts of the lattice, and proceeded along the same crystallographic plane. Leading and trailing shockley partial dislocations were observed. This is shown in Figure 6.

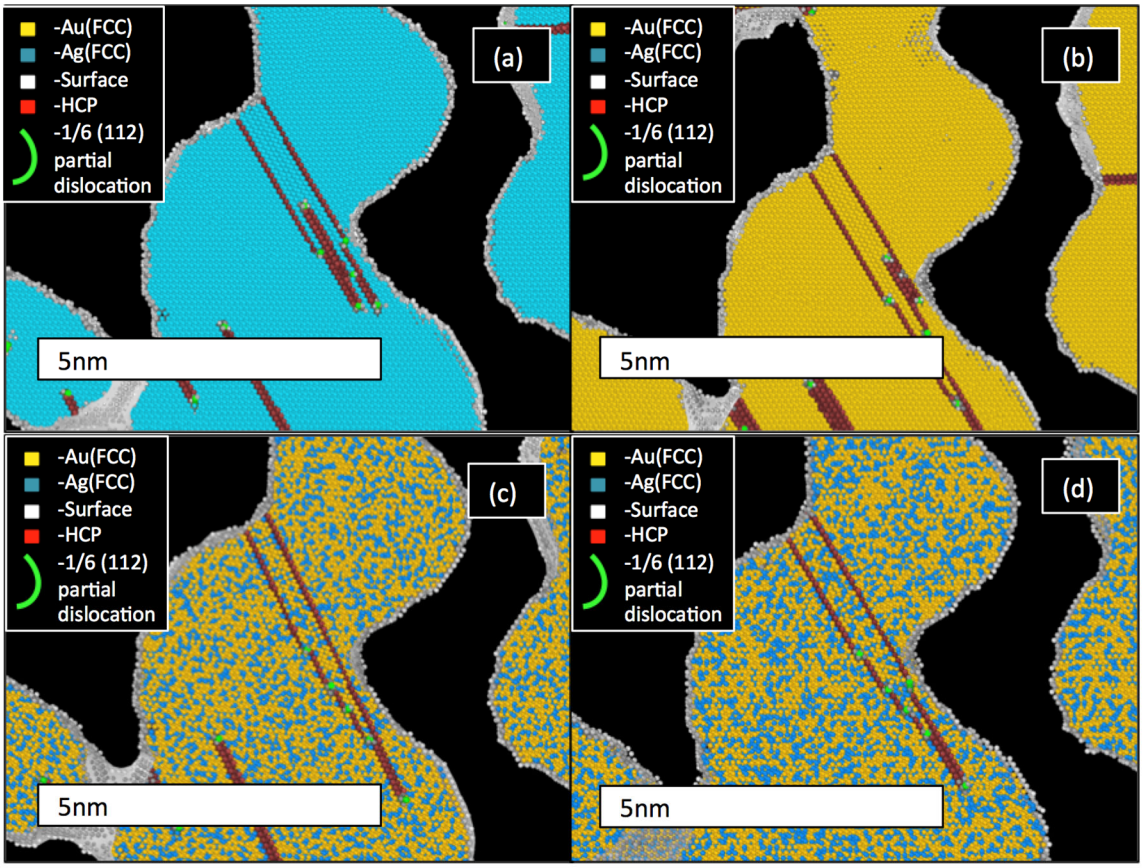

Figure 5-6: Dislocation nucleation and propagation in different lattices under compression. (a) is pure Ag, (b) is pure Au, (c) is a Non-Equilibrated mixture, with total composition 33% Ag, and 67% Au. (d) is the Equilibrated mixture, with total composition of 38% Ag, and 62% Au, and surface composition of 66% Ag, and 33% Au.

Looking at these dislocations from the perpendicular orientation, we see that even in the sample with random binary atom placement, the shape and distribution of these dislocations was not significantly different than the pure Au and Ag lattices, meaning that the bonding energies between the Au and Ag atoms are not significantly different enough to slow or halt the progression of dislocations through the lattice. This is shown in Figure 7. The comparable dislocation densities are another good indicator that bonding and premature strain hardening are not issues, even in the alloyed lattice.

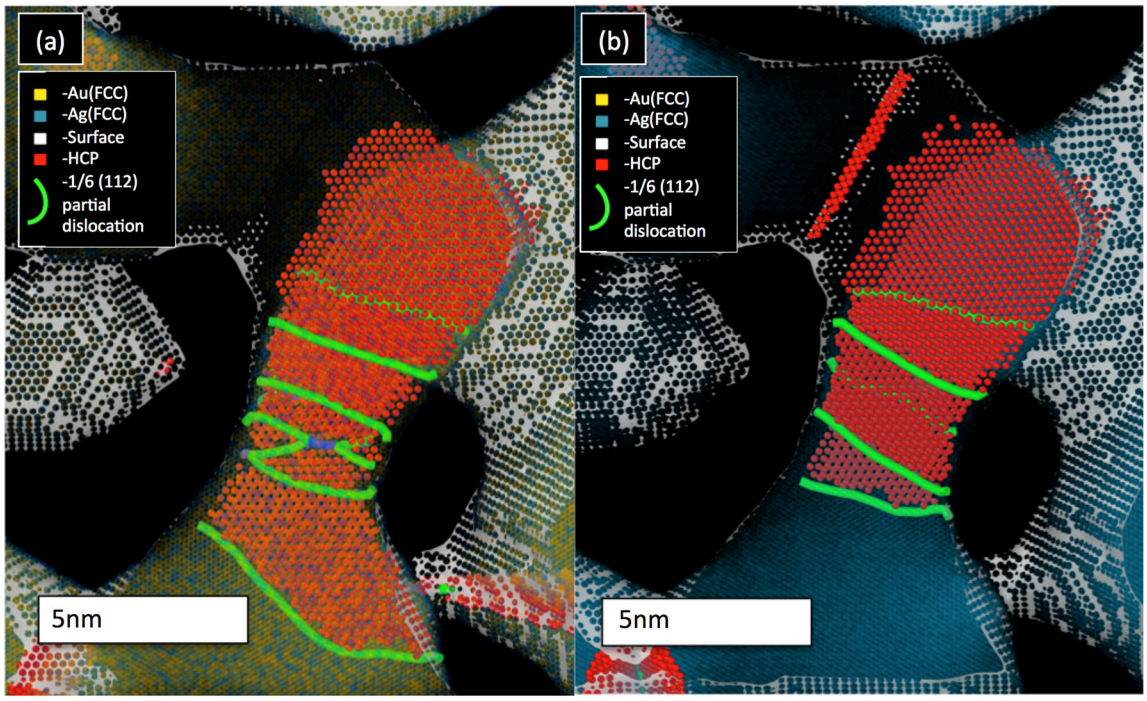

Figure 5-7: Comparison of Dislocation shape and distribution in (a) the equilibrated mixed sample, with surface composition of 66% Ag, and total composition of 38% Ag, and (b) the pure Ag sample.

5.3.4: effect of segregation and mixing on surface stress, and application to a model for segregation.

Our final piece of analysis sought to understand the mechanical properties of the bulk lattice in the context of surface composition, and it's influence on surface effects – i.e., the surface stress and energy. To first understand how differences in surface concentration affected stress and energy of the free solid surfaces of these materials, we created cubical samples similar to the ones described in section 3.1, with approximately 32,000 atoms per box, with the FCC crystal structure rotated such that the x-y plane had crystal faces {100}, {110}, {111}, parallel to the xy face (perpendicular to the z axis). To obtain the surface free energy (or free energy of formation), these samples were energy minimized using the minimize command in LAMMPS, and total energy was obtained. Then, the sample box was lengthened 40 nm in the Z direction, while leaving the atoms themselves unaltered to expose 2 free surfaces. Then, a second minimization was performed, and a second total energy value obtained by the same method. Total energy difference was then divided by total exposed area, according to the equation below:

$$E_s = \frac{(E_p - E_f)}{2A} \qquad [8]$$

Where E_s is the surface energy, E_p is the energy of the periodic box, and E_f is the energy of the box with free sides, and A is the surface area of the exposed sides. Surface Stress values were obtained by deforming the box in the x direction up to 0.081 nm, and measuring the change in energy, against the change in total surface area. This was done over 4 ps, which was a longer

simulation than our previous paper [34], so we believe these values to be more accurate. The results of these tests are shown in Table 2:

Table 5-2: Calculated Surface Stress and Surface energy values for varying surface concentrations of Au and Ag, respectively.

	Au J/m^2	Ag J/m^2	67%Au_33%Ag J/m^2	33%Au_67%Ag J/m^2	62%Au_38%Ag J/m^2
{100} Surface Energy	0.918	0.751	0.86289	0.83611	0.879
{110} Surface energy	0.98	0.762	0.93806	0.80634	0.844
{111} Surface Energy	0.79	0.699	0.71997	0.77903	0.827
{100} Surface Stress	1.779	1.57	1.70003	1.68597	1.772
{110} Surface Stress	1.824	1.62	1.75668	1.66232	1.734
{111} Surface Stress	1.813	1.51	1.73301	1.57599	1.705

Using these data, all energy and stress values were averaged, and plotted as a function of composition. As expected, we see a negative trend in energy as a function of composition of silver, which is consistent with the surface energy properties, calculated for this material from these potentials [54]. As expected, surface stress has consistently higher values than surface energy. This is shown in Figure 8.

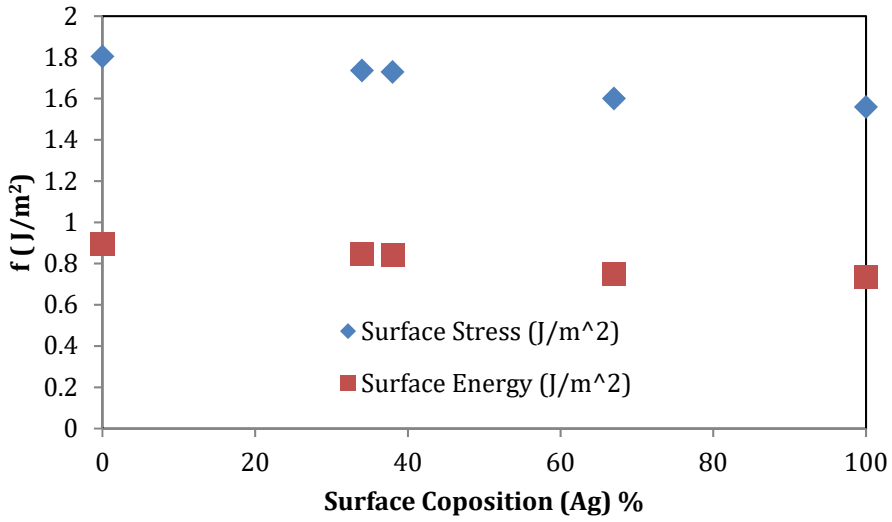

Figure 5-8: Surface stress and energy curves calculated from the free surface cubes

Now, according to a model for yield asymmetry derived by Farkas [9], the effect of an increase in the surface "term" (which we will refer to as "ε") should lead to a correspondent increase in the asymmetry of the tensile/compressive yield of the sample. The proposed model is given below.

$$\sigma_\gamma(d) = \sigma_0(d) \pm \sigma_\epsilon(d) \quad [9]$$

$\sigma_Y(d)$ here is the total yield stress, and $\sigma_0(d)$ is a term that is independent of the surface contribution for the ligament sizes up to 20 nm, and can be considered a constant for a given atomic concentration. This term can be still size-dependent through the "smaller is stronger" effect, but this is only applicable for ligaments above 20 nm. $\Sigma\varepsilon(d)$ is the surface dependent term, and can be represented as a function of surface area to volume ratio as:

$$\sigma_\epsilon(d) = \begin{cases} +\frac{2S\epsilon}{3V} & (tension) \\ -\frac{2S\epsilon}{3V} & (compression) \end{cases} \quad [10]$$

Where (S/V) is the surface area to volume ratio of our sample, and f is the surface contribution term. This model was shown to be valid for computational nanoporous samples where (S/V) was varied, but f held constant [34].

Evidently, an increase in the value of ε should lead to an increase in the asymmetry of the yield response of the material. So, taking the values from Table 1, we divided the values for tensile yield stress by compressive yield stress, to get a dimensionless asymmetry parameter shown in Figure 9

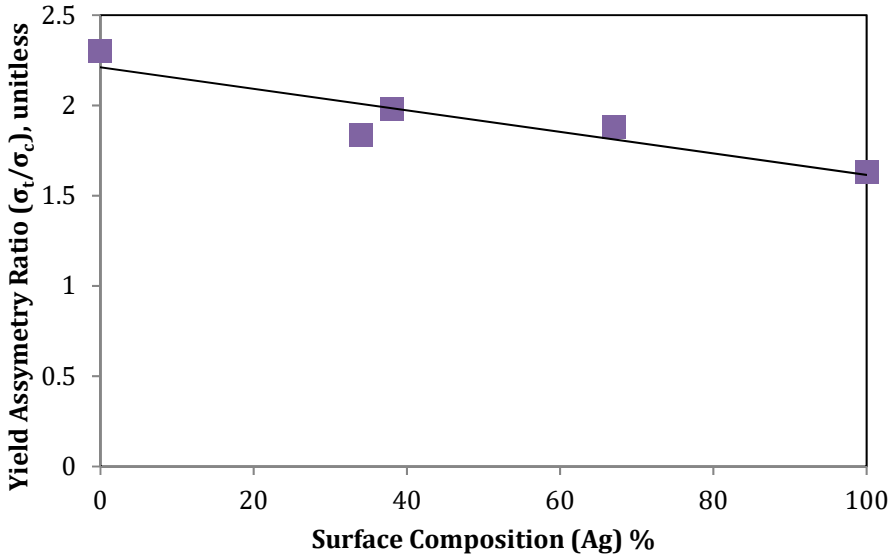

Figure 5-9: Yield asymmetry calculated from the stress/strain curves as a function of surface composition.

As expected, asymmetry increases roughly linearly with composition of Au, and by extension, magnitude of the surface term, f.

The dependence of the yield response on some contribution from the surface is obvious, but as an extra step we sought to understand whether the mechanical behavior conformed more to a model dependent on the stress or energy.

We first needed to isolate the surface dependent term from our model. To do this, we calculated $\sigma_0(d)$ by averaging the tension and compression terms from our model, and subtracted this from the total yield stress for both tension and compression terms, so that only $\sigma_s(d)$ remained. Then, we divided this term by the surface stress and the surface energy for the correspondent surface composition, giving us the following constant value, in units of (1/m).

$$\frac{\sigma_\epsilon(d)}{\epsilon} = \frac{2S}{3V} \qquad [11]$$

Using the surface mesh tool from OVITO, we were able to say that for the sample being considered had a (S/V) value of 0.049. So theoretically, this term should fall close to 0.0326 as possible. We divided the yield stress by the respective values for surface stress and surface energy for each individual composition, and obtained the results shown in Figure 10.

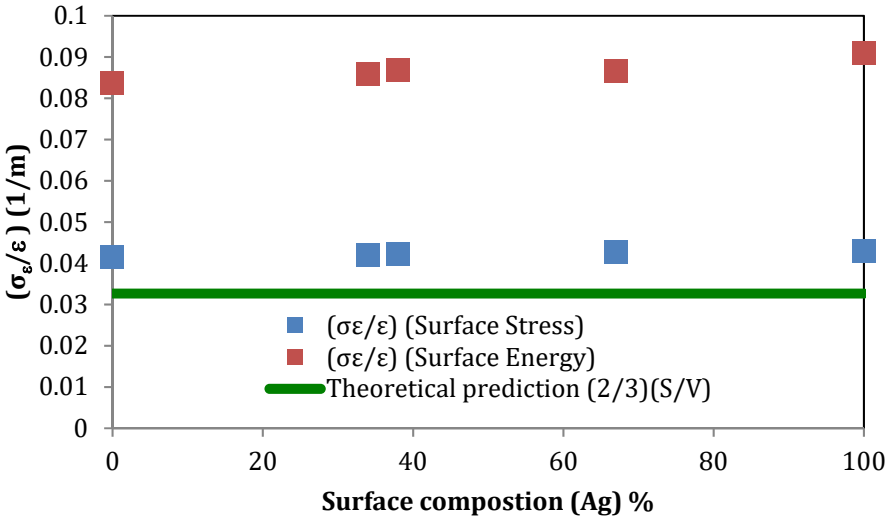

Figure 5-10: The parameter ($\sigma_\varepsilon/\varepsilon$) from equation 11 plotted as a function of surface stress and energy, for stress and energy as calculated form the free surface cubes. The green line is the model prediction of the equivalent value from the model, (2/3)(S/V).

The implications of these results will be covered in the discussion section.

5.4. Discussion:

In this study, we have shown how the effect of the addition of a silver component into a gold nanoporous lattice affects mechanical properties. We have demonstrated that the composition of the surface has a much greater bearing on the yield response, and that this response can be accurately predicted with an established surface dependent model, derived from fundamental thermodynamics. We have demonstrated that there are no unexpected hardening effects that arise from the segregation of silver to the solid surface. Furthermore, we have shown that the variation in the mechanical response as a function of surface composition can be accounted for by the "surface term" in our model.

According to the calculations of the surface-dependent model, the yield stress is very much more dependent upon the surface composition of our material than the internal composition. It is worth noting, however, that the elastic modulus of our material appears to be more dependent on the bulk composition, rather than the surface composition. However, this is not a problem, since while the elastic modulus and yield stress are obviously linked, the process that leads to yielding (primarily, emission of dislocations and twins) in a material is stress dependent. The elastic modulus below the stability threshold will be composition dependent.

When looking at the residual dislocation densities, it seemed odd that the densities for the alloy materials did not fall between the curves for pure silver and gold, respectively. Understanding this requires knowing the energy a dislocation relieves when it is emitted into a solid. The equation for the strain energy released by a dislocation is given below:

$$E = \frac{-\mu b(1-\upsilon)}{(1-\upsilon)} e\pi R^2 \cos(\theta_1)\cos(\theta_2)\epsilon \qquad [12]$$

Wherein μ is the shear modulus, υ is the Poisson ratio, e is the elliptic factor, R is the core radius, θ1 is the angle of the vector normal to the glide plane, θ2 is the angle of the glide direction, of the dislocation in question, and ε is a constant cofactor [55]. Many of these would change in a relaxed alloy structure, and have variations dependent on the local interatomic bonds being broken at a given moment as the dislocation travels. So, the inherent variability in composition, bond strengths, and concentration dependence would lead to this value being higher for the alloy system, leading to fewer dislocations. Evidently, the effect is not great enough to significantly alter the yield response or shape of the dislocations in question, but it may be high enough to allow for a slight increase, that could lead to less emission, and therefore, fewer overall dislocations in the alloy from the outset. But that is beyond the scope of this study.

Perhaps the most exciting result from this study is that the model for yielding behavior derived by Farkas is valid, when considered in the context of surface stress and energy. This model, derived from fundamental thermodynamics, has been shown to give reasonable results when the value of the surface term (ε) is held constant, and the value for surface area to volume ratio is varied. So, it is reasonable to assume that if the (S/V) ratio is held constant, then yield response should evolve in kind with the parameter (ε), which is indeed observed.

It is worth pointing out that the way the model is derived, the term "(ε)" is some component of the surface stress or energy, defined as

$$f = \gamma + \frac{\partial \gamma}{\partial e} \quad [13]$$

wherein "e" is the elastic strain, and γ is the pure surface energy. "f" is the general surface stress term. Our calculations shown in Figure 10 are proof that both f and γ serve as reasonable determiners for the mechanical response, and follow the expected trend of (2/3)(S/V). The relative proximity of both to the model prediction indicate that the surface stress term, as calculated, yields a much closer model fit than surface energy, but there is as far as the authors know no theoretical reason why this term should be equivalent to stress and not energy. In fact, one experimental study strongly suggests that the mechanical behavior is purely a function of the energy [56]. So, for this paper, we can say that the yield data seems to conform to a model dependent on the surface stress, but without more extensive simulations to validate the theory one way or the other, we cannot say for sure. Regardless, the fact that one can predict the mechanical behavior of the material with varying values of (ε), by employing the same model that was used to predict yielding behavior with varying values of (S/V) is significant. And, it validates the assumption that the surface controls yielding behavior.

5.5. Conclusions:

This paper represents a step in the direction of a more complete understanding of surface-driven mechanical response of nanoporous lattices, and has shown how residual silver will have minimal to positive effects on the strengthening of the lattice after dealloying. The addition of silver in the nanoporous lattice has little tangible effect on dislocation nucleation and density, and its contribution to variations in the structure are negligible, since the lattice parameter is so similar, and the structure stays remarkably well ordered when mixed. Yielding behavior is dependent on surface compositions and the capillary contributions therein, while elastic behavior is dependent on bulk composition. Trends in the yield response of this material as a function of size and surface composition can be effectively predicted with a surface-dependent model, and the trend in response seems to be mostly dependent upon the total surface stress.

5.6. Acknowledgements:
This work was supported by the National Science Foundation, DMREF program, number 1533969. The authors acknowledge of the resources of the Virginia Tech Advanced Research Computing Center, and the Nanoscale Characterization and Fabrication Laboratory at Virginia Tech.

5.7. References:
[1] N. Badwe, X. Chen, K. Sieradzki, Mechanical properties of nanoporous gold in tension, Acta Mater. 129 (2017) 251-258.
[2] T.J. Balk, C. Eberl, Y. Sun, K.J. Hemker, D.S. Gianola, Tensile and compressive microspecimen testing of bulk nanoporous gold, Jom 61(12) (2009) 26-31.
[3] A. Hodge, J. Hayes, J. Caro, J. Biener, A. Hamza, Characterization and Mechanical Behavior of Nanoporous Gold, Advanced Engineering Materials 8(9) (2006) 853-857.
[4] J. Biener, A.M. Hodge, A.V. Hamza, L.M. Hsiung, J.H. Satcher, Nanoporous Au: A high yield strength material, J. Appl. Phys. 97(2) (2005) 2-5.

[5] A.M. Hodge, J. Biener, J.R. Hayes, P.M. Bythrow, C.A. Volkert, A.V. Hamza, Scaling equation for yield strength of nanoporous open-cell foams, Acta Mater. 55(4) (2007) 1343-1349.
[6] N.J. Briot, T.J. Balk, Developing scaling relations for the yield strength of nanoporous gold, Philos. Mag. 95(27) (2015) 2955-2973.
[7] N.J. Briot, T. Kennerknecht, C. Eberl, T.J. Balk, Mechanical properties of bulk single crystalline nanoporous gold investigated by millimetre-scale tension and compression testing, Philos. Mag. 94(8) (2014) 847-866.
[8] D.A. Crowson, D. Farkas, S.G. Corcoran, Mechanical stability of nanoporous metals with small ligament sizes, Scripta Materialia 61(5) (2009) 497-499.
[9] D. Farkas, A. Caro, E. Bringa, D. Crowson, Mechanical response of nanoporous gold, Acta materialia 61(9) (2013) 3249-3256.
[10] M. Hakamada, M. Mabuchi, Mechanical strength of nanoporous gold fabricated by dealloying, Scr. Mater. 56(11) (2007) 1003-1006.
[11] J. Jiao, N. Huber, Deformation mechanisms in nanoporous metals: Effect of ligament shape and disorder, Computational Materials Science 127 (2017) 194-203.
[12] G. Masing, Zur Theorie der Resistenzgrenzen in Mischkristallen, Zeitschrift für anorganische und allgemeine Chemie 118(1) (1921) 293-308.
[13] J. Biener, a. Wittstock, L.a. Zepeda-Ruiz, M.M. Biener, V. Zielasek, D. Kramer, R.N. Viswanath, J. Weissmüller, M. Bäumer, a.V. Hamza, Surface-chemistry-driven actuation in nanoporous gold, Nature materials 8(1) (2009) 47-51.
[14] H.J. Jin, J. Weissmüller, Bulk nanoporous metal for actuation, Advanced Engineering Materials 12(8) (2010) 714-723.
[15] H.J. Jin, X.L. Wang, S. Parida, K. Wang, M. Seo, J. Weissmüller, Nanoporous au-pt alloys as large strain electrochemical actuators, Nano Letters 10(1) (2010) 187-194.
[16] E. Detsi, Z.G. Chen, W.P. Vellinga, P.R. Onck, J.T.M.D. Hosson, Actuating and Sensing Properties of Nanoporous Gold, Journal of Nanoscience and Nanotechnology 12(6) (2012) 4951-4955.
[17] Y. Ding, M. Chen, J. Erlebacher, Metallic mesoporous nanocomposites for electrocatalysis, Journal of the American Chemical Society 126(22) (2004) 6876-6877.
[18] C. Xu, J. Su, X. Xu, P. Liu, H. Zhao, F. Tian, Y. Ding, Low Temperature CO Oxidation over Unsupported Nanoporous Gold, J. Am. Chem. Soc. 129(1) (2006) 42-43.
[19] X.Y. Lang, L.Y. Chen, P.F. Guan, T. Fujita, M.W. Chen, Geometric effect on surface enhanced Raman scattering of nanoporous gold: Improving Raman scattering by tailoring ligament and nanopore ratios, Appl. Phys. Lett. 94(21) (2009) 213109.
[20] Y. Xue, J. Markmann, H. Duan, J. Weissmüller, P. Huber, Switchable imbibition in nanoporous gold, Nature communications 5(May) (2014) 4237-4237.
[21] Z. Qi, J. Weissmüller, Hierarchical nested-network nanostructure by dealloying, ACS Nano 7(7) (2013) 5948-5954.
[22] J. Stuckner, M. Murayama, Mechanical properties of nanoporous gold subjected to tensile stresses in real-time, sub-microscopic scale, Journal of Materials Science 54(18) (2019) 12106-12115.
[23] O. Okman, J.W. Kysar, Fabrication of crack-free blanket nanoporous gold thin films by galvanostatic dealloying, Journal of Alloys and Compounds 509(22) (2011) 6374-6381.
[24] O.J. Kleppa, Note on the thermodynamics of the liquidus and solidus curves in systems with complete solid solubility; the system silver-gold, Acta Metallurgica 8(11) (1960) 804-806.

[25] J.F. Huang, I.W. Sun, Fabrication and Surface Functionalization of Nanoporous Gold by Electrochemical Alloying/Dealloying of Au–Zn in an Ionic Liquid, and the Self-Assembly of L-Cysteine Monolayers, Advanced Functional Materials 15(6) (2005) 989-994.
[26] J. Zeng, F. Zhao, M. Li, C.-H. Li, T.R. Lee, W.-C. Shih, Morphological control and plasmonic tuning of nanoporous gold disks by surface modifications, Journal of Materials Chemistry C 3(2) (2015) 247-252.
[27] Y. Jin, R. Li, L. Zuo, T. Zhang, Correlation between dealloying conditions and coarsening behaviors of nanoporous silver produced by chemical dealloying of Ca-Ag metallic glass, Journal of Alloys and Compounds 695 (2017) 1600-1609.
[28] L. Chaoqing, L. Lixian, L. Ying, L. Qin, Fabrication, Characterization of Ultra-low-density Bulk Nanoporous Gold with Uniform Structure and Volume Shrinkage Control During Drying, Rare Metal Materials and Engineering 47(8) (2018) 2322-2327.
[29] S. Van Petegem, S. Brandstetter, A.M. Hodge, B.S. El-Dasher, J. Biener, B. Schmitt, C. Borca, H. Van Swygenhoven, On the microstructure of nanoporous gold: an X-ray diffraction study, Nano letters 9(3) (2009) 1158-63.
[30] N. Mameka, J. Markmann, J. Weissmüller, On the impact of capillarity for strength at the nanoscale, Nature Communications 8(1) (2017) 1976.
[31] H.-J. Jin, J. Weissmüller, D. Farkas, Mechanical response of nanoporous metals: A story of size, surface stress, and severed struts, MRS Bulletin 43(1) (2018) 35-42.
[32] N. Huber, Connections Between Topology and Macroscopic Mechanical Properties of Three-Dimensional Open-Pore Materials, Frontiers in Materials 5 (2018) 69.
[33] N. Beets, D. Farkas, Mechanical Response of Au Foams of Varying Porosity from Atomistic Simulations, JOM 70(10) (2018) 2185-2191.
[34] N. Beets, D. Farkas, S. Corcoran, Deformation mechanisms and scaling relations in the mechanical response of nano-porous Au, Acta Mater. 165 (2019) 626-637.
[35] K. Wang, A. Kobler, C. Kübel, H. Jelitto, G. Schneider, J. Weissmüller, Nanoporous-gold-based composites: toward tensile ductility, NPG Asia Materials 7(6) (2015) e187-e187.
[36] L. Lührs, B. Zandersons, N. Huber, J. Weissmüller, Plastic Poisson's Ratio of Nanoporous Metals: A Macroscopic Signature of Tension–Compression Asymmetry at the Nanoscale, Nano Letters 17(10) (2017) 6258-6266.
[37] P. Peng, H. Sun, A.P. Gerlich, W. Guo, Y. Zhu, L. Liu, G. Zou, C.V. Singh, N. Zhou, Near-ideal compressive strength of nanoporous silver composed of nanowires, Acta Materialia 173 (2019) 163-173.
[38] J. Biener, A.M. Hodge, J.R. Hayes, C.A. Volkert, L.A. Zepeda-Ruiz, A.V. Hamza, F.F. Abraham, Size Effects on the Mechanical Behavior of Nanoporous Au, Nano Letters 6(10) (2006) 2379-2382.
[39] J. Erlebacher, I. McCue, Geometric characterization of nanoporous metals, Acta Mater. 60(17) (2012) 6164-6174.
[40] A.M. Hodge, R.T. Doucette, M.M. Biener, J. Biener, O. Cervantes, A.V. Hamza, {A}g effects on the elastic modulus values of nanoporous {A}u foams, J. Mater. Res. 24(4) (2009) 1600-1606.
[41] A.R. Yavari, Mechanically Prepared Nanocrystalline Materials (<I>Overview</I>), Materials Transactions, JIM 36(2) (1995) 228-239.
[42] M. Park, T. Chookajorn, C.A. Schuh, Nano-phase separation sintering in nanostructure-stable vs. bulk-stable alloys, Acta Materialia 145 (2018) 123-133.

[43] A. Khalajhedayati, Z. Pan, T.J. Rupert, Manipulating the interfacial structure of nanomaterials to achieve a unique combination of strength and ductility, Nature Communications 7 (2016) 10802.
[44] T. Chookajorn, C.A. Schuh, Thermodynamics of stable nanocrystalline alloys: A Monte Carlo analysis, Physical Review B 89(6) (2014) 064102.
[45] D. Crowson, D. Farkas, S.G. Corcoran, Geometric relaxation of nanoporous metals: The role of surface relaxation, Scripta materialia 56(11) 919-922.
[46] A. Stukowski, Visualization and analysis of atomistic simulation data with OVITO–the Open Visualization Tool, Modelling and Simulation in Materials Science and Engineering 18(1) (2009) 015012.
[47] D. Fuks, V. Segel, Temperature dependence of the enhancement factors for diffusion in dilute substitutional alloys, Materials Letters 21(5) (1994) 399-404.
[48] B. Sadigh, P. Erhart, A. Stukowski, A. Caro, E. Martinez, L. Zepeda-Ruiz, Scalable parallel Monte Carlo algorithm for atomistic simulations of precipitation in alloys, Physical Review B 85(18) (2012) 184203.
[49] S.M. Foiles, M. I. Baskes, M. Daw, Embedded-atom-method functions for the fcc metals Cu, Ag, Au, Ni, Pd, Pt, and their alloys, 1986.
[50] D. Wolff, W.G. Rudd, Tabulated potentials in molecular dynamics simulations, Computer Physics Communications 120(1) (1999) 20-32.
[51] S. Plimpton, Fast Parallel Algorithms for Short-Range Molecular Dynamics, Journal of Computational Physics 117(1) (1995) 1-19.
[52] B. Sadigh, Scalable parallel Monte Carlo algorithm for atomistic simulations of precipitation in alloys. , Physical Review B 85(18) (2012) 184203.
[53] I. Alabd Alhafez, C.J. Ruestes, E.M. Bringa, H.M. Urbassek, Nanoindentation into a high-entropy alloy – An atomistic study, Journal of Alloys and Compounds 803 (2019) 618-624.
[54] Z.T. Lucas Hale, Chaneler Beckler, NIST Intteratomic Potentials Repository. <https://www.ctcms.nist.gov/potentials/entry/1986--Foiles-S-M-Baskes-M-I-Daw-M-S--Ag/1986--Foiles-S-M--Ag--LAMMPS--ipr1.html>, 2019).
[55] P. Hirel, J. Godet, S. Brochard, L. Pizzagalli, P. Beauchamp, Determination of activation parameters for dislocation formation from a surface in fcc metals by atomistic simulations, Physical Review B 78(6) (2008) 064109.
[56] J. Weissmüller, K. Sieradzki, Dealloyed nanoporous materials with interface-controlled behavior, MRS Bulletin 43(1) (2018) 14-1

Chapter 6: Mechanical Response of a Bicontinuous Copper-Molybdenum Nano-composite: Experiments and Simulations

Nathan Beets(a)*, Yuchi Cui(b), Diana Farkas(a) and Amit Misra(b)
(a) Department of Materials Science and Engineering, Virginia Tech
Holden Hall, 445 Old Turner St, Blacksburg, VA 24060
(b) Department of Materials Science and Engineering, The University of Michigan
Herbert H. Dow Building, 2300 Hayward St, Ann Arbor, MI, 48109
* Corresponding Author

6.0 Abstract

We present the results of a combined experimental and simulation-based study of the mechanical response of a bicontinuous copper-molybdenum nanocomposite, where high strength and good plastic deformability were observed. The experimental sample, prepared by co-sputtering Cu and Mo, achieved a feature size of around 15 nm. Corresponding digital nanostructures with feature sizes between 9 to 15 nm were generated using a phase field model. Virtual compression testing was performed using molecular dynamics simulation. The resultant mechanical response of these samples was analyzed at the macroscopic and atomistic levels. Strain partitioning was observed, where most of the plastic deformation occurs through dislocations that are emitted from the interface into the FCC Cu phase. The interface also acts as a barrier to dislocation propagation. The nanocomposites exhibit high strain hardening rate and plastic co-deformation in Cu and Mo intertwined phases. No shear banding is observed after 30% compression in both experiment and simulation. The bicontinuous, intertwined morphology of metallic FCC/BCC nanocomposites is effective in producing high yield strengths, high strain hardening rate and uniform distribution of plasticity in the sample volume.

Keywords: Metallic nanocomposite, mechanical behavior, interfaces

6.1 Introduction

In standard bulk media, yield strength and plasticity are desirable but conventionally considered mutually exclusive, so there is a pressing interest in novel composite materials that can deform plastically while maintaining high strength[1]. Metallic nano-composites have received great attention due to their exceptional properties in this regard[2, 3]. Most studies have focused on multilayers of different metals[4-9]. Their high strength is generally attributed to the role of the interface as a barrier to slip transmission. Experimentally, these structures have been shown to reach between (1/2) and (1/3) of the theoretical limit for strength. The effects of temperature, microstructure, and feature size on mechanical behavior of lamellar composites have also been investigated [10, 11]. Composite strength is a function of the feature size, which follows a general "smaller is stronger" trend. However, the formation of shear bands as a primary deformation mechanism leads to undesirable failure of the material upon the onset of plasticity. This means that while layered structures provide strength closer to the theoretical limit, they have very limited deformability [3, 8, 9, 12-18] [19].

It has been suggested that novel composite morphologies may resolve this issue by eliminating or blocking possible shear bands. In fact, this has been confirmed experimentally by methods such as introducing nanotwin substructures into the grains, or altering grain size and structure [20, 21]. A new method of high temperature, instantaneous structural generation via co-sputtering of immiscible metallic media has created novel separated composite structures with varying morphologies that can be tuned by the conditions of deposition rate and substrate temperature [22-26]. This new method generates composites with large completely phase-separated pure Copper/Molybdenum bicontinuous structures with ligaments of a few nm in length scale that possesses very high strength [26, 27]. Bicontinuous alloy structures with nanoscale features have great potential for resisting flow localization and they can have high strength with overall superior mechanical properties. Of the samples observed, three morphologies were identified based on different combinations of deposition conditions and substrate temperature, with separated phase concentrations varying from lateral concentration modulation (resembling nano-sized layered structures) to random concentration modulation (resembling a spinodally decomposed structure). Mechanical tests of the random concentration modulation structure (referred to form now on as the RCM structure) revealed that it maintained a high strength, and excellent deformability, with compression tests on isolated pillars up to 30% strain revealing no shear banding whatsoever [27]. Thus, the RCM morphology is important as a model system, because it is a phase-separated morphology of immiscible components with very different mechanical properties. Understanding the interplay between the two phases from an energetics and structural point of view can serve as a template by which to design other similar metallic nano-composites with desirable mechanical properties. An understanding of the role of the interface on deformation and mechanical behavior and how this can be applied to other materials generally with immiscible, phase-separated regions will be useful for nano-composite design moving forward[18].

Atomistic simulations have been very useful in understanding the reasons for the specific role of interfaces in layered nano-composites [13, 14, 25, 28-33] as well as bicontinuous nano-porous structures [10, 22-25]. Specifically, molecular dynamics techniques have been shown to be useful in modeling the specific effects of interfaces [13, 28, 30-35]. For these composite systems, it has been shown that the structure and energy of the interface plays a major role in the deformation behavior [29, 36-38]. Especially, atomistic studies have shown that for FCC interfaces, a Kurdjumov-Sachs (KS) orientation can lead to improved mechanical properties [36, 37]. So, we incorporate a combined experimental and computational molecular modeling approach to characterize the properties of the structure.

The purpose of the present work is to understand deformation mechanisms in bicontinuous nano-composites of nearly equiatomic Cu/Mo composition. We present a combined experimental and simulation study of the compression response of these structures. A specific focus is on the relationship between ligament diameter and morphology with general properties such as yield stress, dislocation nucleation and propagation and strain hardening. Using large-scale parallel computing techniques, we are able to reach the same feature sizes as in the experiments. Molecular dynamics simulations were conducted on a series of computationally generated samples that can be directly compared with the experimental results obtained in order to gain

insight into the fundamental deformation mechanisms and how mechanical properties are affected by feature size.

6.2. Methods

6.2.1 Experimental Methods

Cu and Mo were co-deposited onto Si substrates with oxide surface layer by direct-current (DC) magnetron sputtering at 800o C. The Si substrate was chosen to minimize the substrate effect during the mechanical testing due to its high hardness. 99.999% pure Cu and 99.95% pure Mo targets were confocally oriented during deposition and the nominal deposition rate was held at 0.7 nm/s for each of the constituents. The pressure prior to deposition was maintained below 2.7× 10-7 Pa. The final thickness of the thin film nanocomposite was set as 1 μm.

Scanning electron microscopy (SEM) characterization of the samples was conducted in a FEI Magellan 400 SEM. A double Cs-corrected JEOL3100R05 was used to perform transmission electron microscopy (TEM) and scanning TEM (STEM) characterizations. Elastic modulus and hardness of the nanocomposite were measured from nanoindentation tests conducted using Hysitron TI 950 Triboindenter. Diamond Berkovich tip was used to make 150 nm deep indentations to get an average measurement. Hysitron PI 85 SEM Picoindenter was used to conduct in situ nanopillar compression tests. Diamond flat-punch indenters were used in displacement control mode to maintain a fixed strain rate of 2×10-3/s. Focused ion beam (FIB) in FEI Helios Nanolab DualBeam SEM was used to prepare nanopillar and TEM foils. The beam current used for the final step of sample preparation was chosen at 50 pA to minimize ion beam damage. The as-fabricated cylindrical nanopillars have diameters of 450 nm and heights of 1 μm, which is the thickness of the deposited thin film. Due to the Gaussian profile of the ions in the FIB and re-deposition effect, the nanopillars have inevitable taper angles of ~ 2.2o. Four pillars were tested to provide an average stress-strain curve.

6.2.2 Computational Methods

The LAMMPS software package developed by Steve Plimpton [39] was used to carry out all the molecular dynamics simulations. The EAM (Embedded Atom Method) potential developed by Gong et al. was used to model the atomic interaction in the copper-molybdenum system [32, 40]. This potential was developed based on ab initio calculations that were performed to predict the structures, lattice constants, and cohesive energies of the metastable Cu75Mo25, Cu50Mo50, and Cu25Mo75 phases, as well as the elastic behavior of pure Cu and Mo phases. The predicted structures and lattice constants are in good agreement with the data reported in the literature.

In addition, we computed the generalized stacking fault energies for both pure FCC copper and pure BCC molybdenum phases. For copper, we obtained stable and unstable stacking fault energies of 0.120 J/m2 and 0.040 J/m2 respectively. These values are in good agreement with the ab initio calculations reported by Brandl et. al. of 0.164 J/m2 and 0.038 J/m2.[41] For molybdenum, the generalized unstable stacking fault energy predicted by the potential is 1.18 J/m2. This value is in reasonable agreement with the ab initio result of 1.7 J/m2 reported by Park

et al. [42]. We conclude that this potential is adequate to study trends in mechanical behavior of both phases in the composites.

In order to generate a bicontinuous structure similar to the experimental sample, we employed a phase field scheme based on the Cahn-Hilliard formalism to create an interconnected two phase structure. Even though the Cahn-Hilliard formalism applies to spinodal decomposition, this technique has been shown to mimic the structure of nanoporous gold lattices [38, 43]. In the present work, a random 50/50 bicontinuous phase field was generated, and served as our general morphology, seen in Figure 1. The structure is periodic on all sides. The technique is adequate for mimicking the randomly modulating, continuous phases of the deposited Cu-Mo lattice. The comparison of the simulation sample with the experiments is shown in Figure 1.

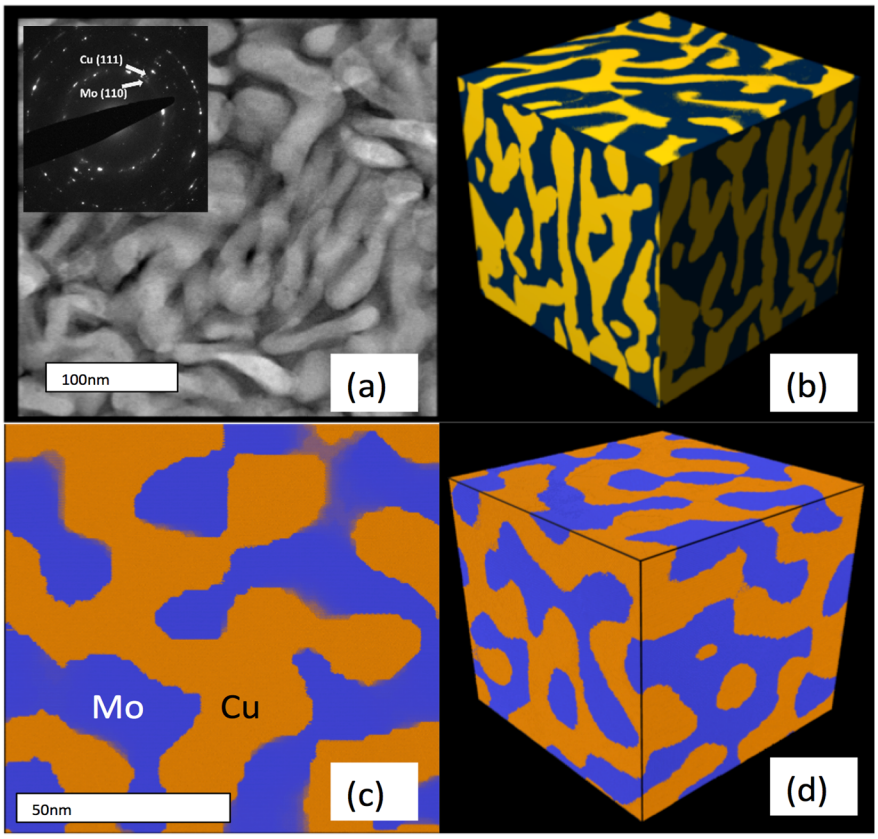

Figure 6-1: Sample structure for the experimental and computational sample. (a) and (c) show a slice of the sample structure with Random concentration modulation in the microstructure. (b) shows a recreation of the expected structure from a series of 2D SEM images, and (d) shows the whole generated computational sample, with 15nm average ligament diameter.

Once created, the base morphology was rescaled to have box dimensions corresponding to average internal ligament diameters of 9 nm, 12 nm and 15 nm. The samples were cubic with dimensions of 65.0 nm, 86.6 nm, and 108.3 nm, respectively. Average ligament diameter was determined using the AQUAMI code developed by Joshua Stuckner [44]. While only the largest of these samples was observed to have ligament diameters comparable to those observed experimentally, the feature size for the experimental samples is by no means uniform for a particular morphology, and by creating three otherwise identical samples with the only

significant difference being their feature size, we were able to observe how macro-scale mechanical properties such as yield stress and dislocation density changed with feature size.

The individual phases were populated with atoms in the FCC and BCC structures, with lattice parameters 3.61 Å and 3.15 Å respectively, corresponding to the lattice parameters for copper and molybdenum. The orientation relationship of these two phases was a Kurdjumov-Sachs (K-S) orientation relationship [37, 45]. This orientation relationship was chosen to match the experimental samples (see the results section). The three samples were deformed uniaxially in in compression using the NPT ensemble up to 30% strain. Under these conditions, the trans-axial sides were allowed to expand to account for the elastic and plastic Poisson effect.

Each sample was relaxed and deformed using a Noose-Hoover thermostat and barostat, and equilibrated at 300 K for approximately 2 ns. After equilibration, each sample was deformed in compression at a rate of (3x108) s-1 up to 30% strain. It should be noted that even though the simulations achieved the same length scale as the experiments, the strain rates in the molecular dynamics study are much faster than in the experiments.

The deformation was strain-controlled with the stress and energy levels of all atoms on the interior and surfaces monitored as the deformation proceeded. Selected snapshots were obtained by quenching the samples from 300 K to 10K in 0.01 ns in order to eliminate thermal vibrations and study the local distribution of stresses. Visualization of defects was performed using OVITO [38], which included the analysis of dislocations by the DXA dislocation extraction formalism [38] and analysis of volume and surface area relationships via the surface mesh formalism [44, 46].

6.3. Results:

6.3.1 Experimental Characterization

Figure 1a shows a STEM image of the as-deposited sample. Cu phases present darker contrast due to its lower atomic weight. Bicontinuous intertwined structure can be observed in both images with an average ligament size of ~ 15 nm. The inset is a selected area diffraction pattern (SADP) of the region. Diffraction spots from FCC Cu and BCC Mo can be observed. A 3-dimensional reconstruction of the structure based on the two images can be found in Figure 1b. Figure 2b shows an atomic image at the Cu/Mo interface. A Kurdjumov-Sachs (KS) orientation relationship can be traced, where Cu (111)FCC//Mo(110)BCC and Cu [10$\bar{1}$]FCC//Mo [11$\bar{1}$]BCC.

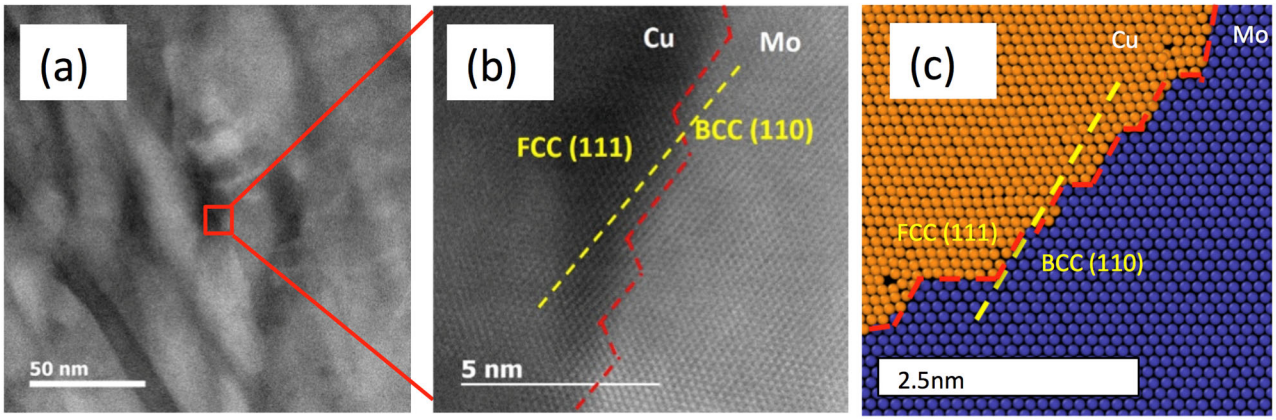

Figure 6-2: (a) shows a magnified view of the microstructure from an SEM image. (b) and (c) show the Kurdjumov Sachs orientation observed at the interface, captured in a TEM image and OVITO illustration, respectively.

6.3.2 Interface structure and energy

In both experimental and simulated samples, the orientation relationship between the BCC and FCC phases is the Kurdjumov-Sachs relationship. Experimental TEM analysis demonstrated this was the dominant preferred orientation relationship in the samples after self-organization. In the simulated samples we studied the structure and energy of the interface in detail. Prior to sample deformation, we relaxed the computational sample using the NPT ensemble at 300K for 2ns. A detailed view of the interface structure both experimentally and computationally is shown in Figure 3. After relaxation, we isolated the interface atoms by selecting atoms in the lattice with nearest neighbors of a different type within a 0.3 nm radius. The interface region contained 53% copper, and 47% molybdenum, similar to the overall composition of the composite.

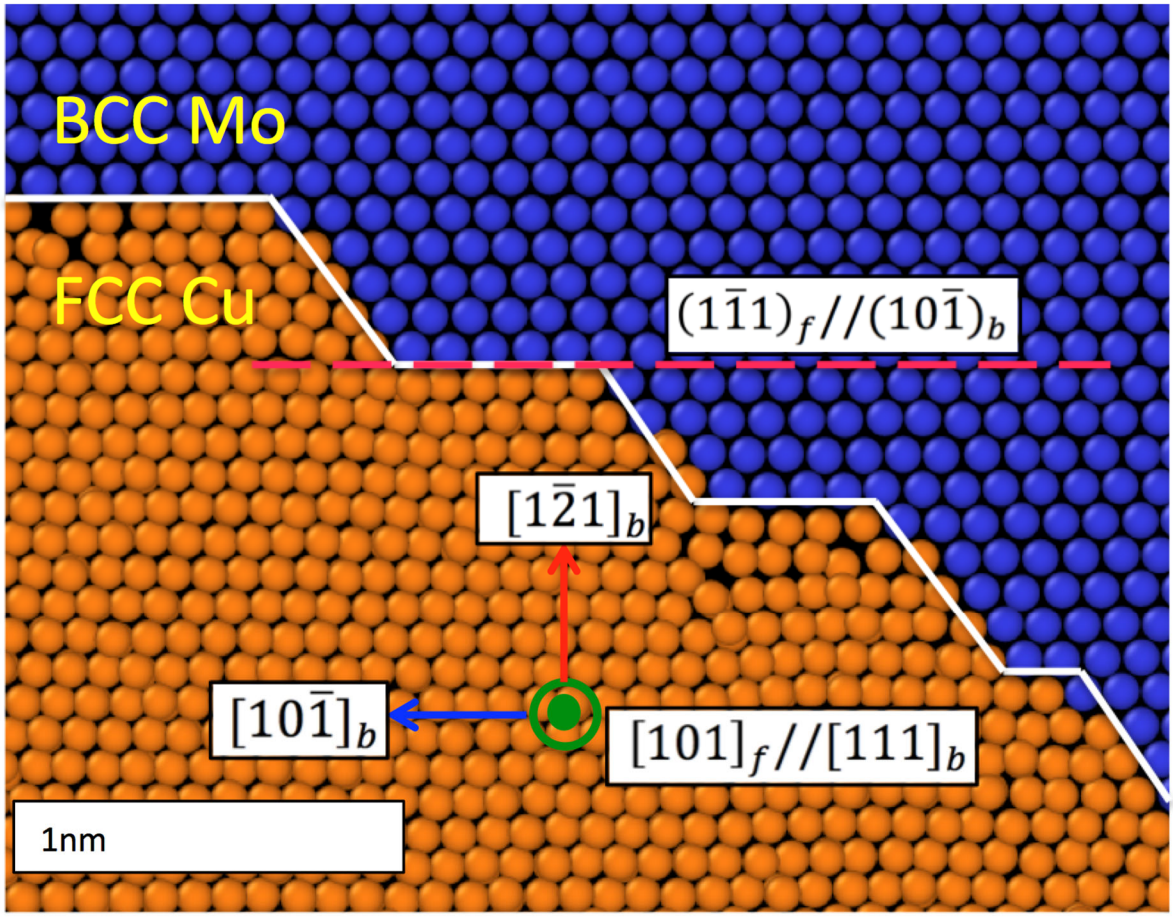

Figure 6-3: A slice of the sample with a Kurdjumov Sachs interface between the FCC and BCC phases. This detail of the interface structure in the computational sample shows faceting along compact planes.

In order to estimate the interface energy, we first calculated the total interface area for all three samples, and quenched samples to 10K, getting the total energy from the LAMMPS output file. We also calculated the average energy of perfect lattice molybdenum BCC atoms and copper FCC atoms at 10K. This was done by separate relaxation of the perfect lattices at 10K using exactly the same conditions as used in the composite. We found average per atom energy of the copper to be -3.5142 eV per atom, and -6.8102 eV per atom for the molybdenum. Using these numbers, the interface area and the total number of atoms of each type in our sample, the interface energy can be calculated as follows:

$$E_{Interface} = \frac{(E_{total} - E_{perfect})}{(Interface\ Area)} \quad (1)$$

The resulting interface energies are given in Table 1 for the three ligament sizes studied.

Table 6-1: Interface energies as a function of average ligament diameter

Average Ligament Diameter (nm)	Interface Energy at 10K (J/m^2)
9	1.318
12	1.301
15	1.297

These values can be compared to ab initio calculations of similar systems available in the literature with K-S interface orientations. For the Cu-Nb system interface energies are reported to be between 0.580 J/m2 and 1.07 J/m2[37, 47, 48]. For the Ni-Cr System, interface energies were calculated to be 0.67 J/m2[49]. For the Ag-Fe System, interface energies were calculated to be 1.13 J/m2[50]. In the study by Beyerlein et al. for Cu-Nb interfaces, it was found that interface energy increased by 50 percent when steps and curvature were introduced[47]. So, while these reported interfacial energies for planar interfaces are somewhat lower than our calculated value of approximately 1.3 J/m2, this can be due to the steps and curvature of our interface. Considering this, our value of 1.3 J/m2 is reasonable when compared to similar K-S interface systems.

Faceting is prevalent in both experimental and simulated samples, as shown in Figures 2b, 2c and 3. The preference is for BCC <110> and <111> faceting. The energy distribution of the atoms in the simulated interface is shown in Figure 4, separately for the Cu and Mo atoms. These data show the structure and energy distribution for atoms in the interface for the relaxed sample immediately prior to deformation. The energy profile for copper and molybdenum atom types are noticeably different. The copper atoms in the interface do not show specific peaks in the energy distribution, whereas the Mo atoms clearly do. The peaks in the energy distribution correlate with atoms in specific facets of the interface, described in Figure 4. This suggests that the observed faceting is driven by the energetics of the Mo atoms in the interface. Prior to any applied deformation, the copper lattice conforms to the structure dictated by the molybdenum. This lattice strain accommodates the difference in atomic sizes between the two component species. The K-S orientation relationship relaxed in this way is still advantageous even in cases where the two atomic sizes do not match, such as in the present case or the Cu/Nb system [30].

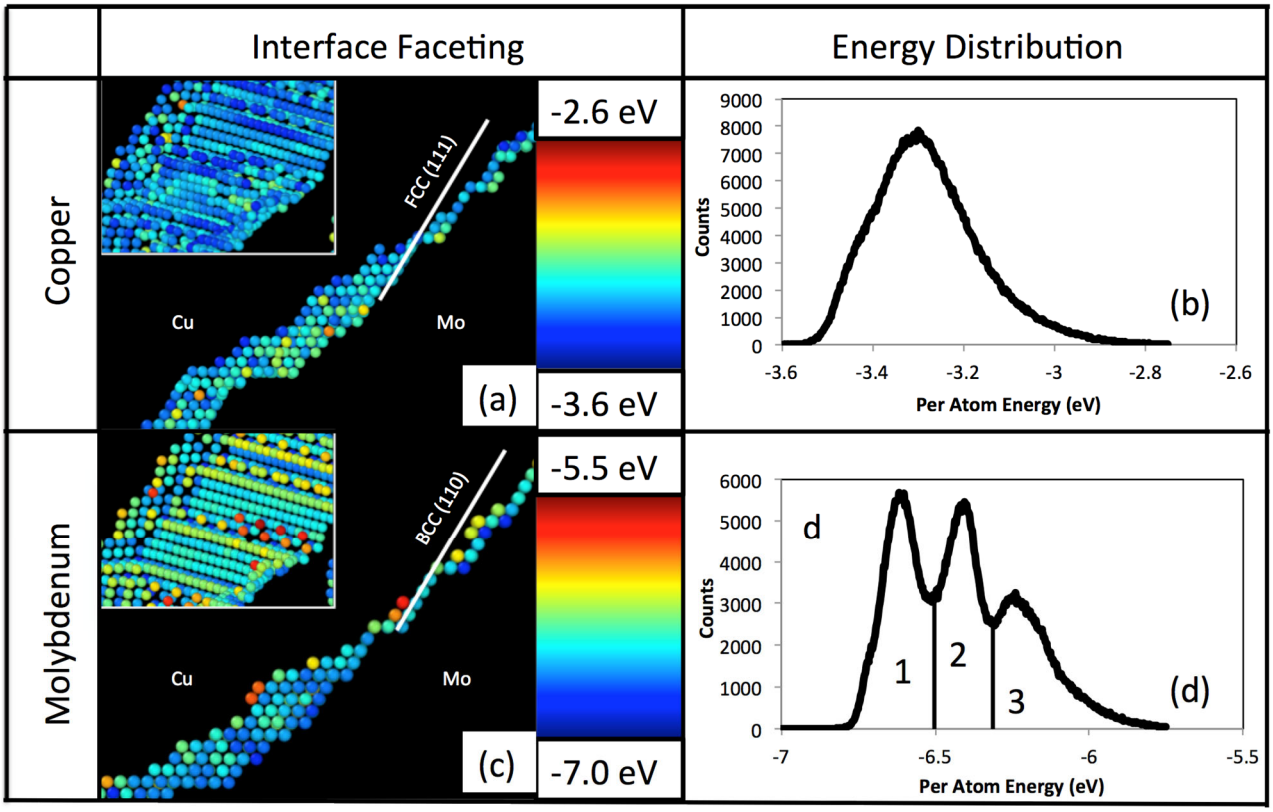

Figure 6-4: Structure (a and c) and energy(b and d) distribution profiles of the interface, for both copper and molybdenum atoms, respectively. (a) and (b) show the copper section interface with faceting and no distinct energy segregation, while (c) and (d) show the molybdenum section of the interface with faceting and distinct energy segregation. The numbered sections correspond to (1) majority 111 and 110 planes, (2) majority 110 planes and (3) no specific low index planes.

It is important to note that during relaxation, some dislocations are nucleated in the copper phase, even without any applied deformation. Dislocation measurements and their role in mechanical properties will be discussed in section 3.5.

6.3.3 Experimental Mechanical Testing

The elastic modulus of the random concentration modulation composite was measured from nanoindentation tests performed using a Hysitron TI950 Triboindenter with a diamond Berkovich tip. A total of 25 indents were made at displace control mode with depth of 150 nm. From the linear portion of the unloading curve, the elastic unloading stiffness can be calculated as S= dP/dh. Coupled with the geometry of the tip, the effective modulus Eeff can then be derived and provided by the Triboindenter software. The derivation of Eeff is defined as follows:

$$\frac{1}{E_{eff}} = \frac{1-\nu^2}{E} + \frac{1-\nu_i^2}{E_i} \quad (2)$$

where E and v are the elastic and Poisson's ratio of the sample respectively, and the subscript i denoted the indenter, which is diamond. Using the measured Eeff = 188 ± 14 GPa, ¬v =0.3, Ei = 1140 and vi = 0.07 (given by Hysitron), the elastic modulus of the nanocomposite was calculated as 204 ± 18 GPa. Using rule of mixtures, the average bulk modulus of Cu and Mo is ½ (130+330) = 230 GPa. The slight difference might come from the surface roughness of the thin film nanocomposite, measured at 39 nm. The nanoindentation test also gives hardiness value (H) = 7.35 ±1.50 GPa. Using H=Kσy with K=3, the yield strength, σy, of the nanocomposite was estimated to be 2.45 GPa.

Nanopillar compression tests were also conducted to measure the stress-strain response of the nanocomposite. The average true stress strain curve obtained from four pillar tests is shown in Figure 5. At 0.2 % offset, the yield stress is measured as 2.2 ± 0.2 GPa, in agreement with the estimation from the nanoindentation results. Due to the compliance of the in situ apparatus, the linear portion of the stress strain curve does not represent the true elastic modulus of the nano-composite. The peak flow stress is 2.4 ± 0.3 GPa, followed by a near-flat stress curve above 2.2 GPa till the end of the test at 35 % compression, which implies a stable deformation without localized shear band formation.

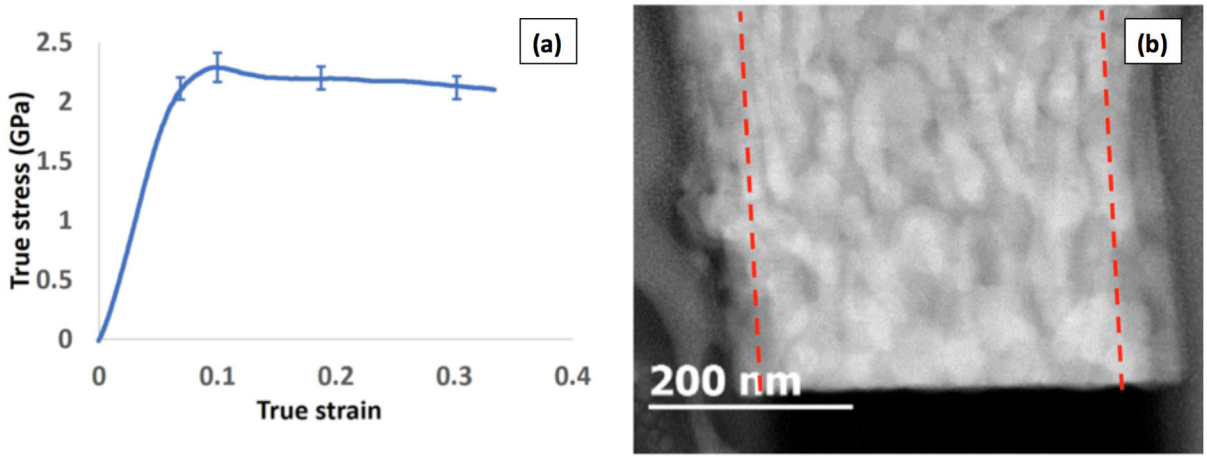

Figure 6-5: The total stress strain curves for four experimental samples with error bars (a), all with the same ligament diameter, and an image of how the 15 nm experimental sample deformed after a 30% uniaxial deformation (b).

6.3.4 Simulated Stress Strain Curves and Analysis

From the simulations in the strain controlled virtual compressive testing, we obtain the total yield stress in the compressed direction, which is 2.49 GPa for the 9 nm sample, 2.51 GPa for the 12 nm sample, and 2.53 GPa for the 15 nm sample. The results shown in Figure 6a for the three ligament sizes studied. The results for the elastic modulus are 171.2 GPa for the 9 nm composite, 174.7 GPa for the 12 nm composite, and 178.2 GPa for the 15 nm composite, increasing slightly with increasing ligament diameter and decreasing interfacial area to total volume ratio. These results indicate that ligament diameter on this scale and for these particular morphologies has a small, nearly inconsequential effect on elastic response. For comparison, we calculated the elastic moduli for pure Cu and pure Mo blocks in the same orientations as in the nanocomposite by creating differently oriented blocks of pure Copper and Molybdenum that

were identical in their orientation to the simulated bicontinuous composite – that is, copper deformed in the [110] direction, and molybdenum deformed in the [111] direction. The values were 133 and 281 GPa respectively, meaning that the average expected elastic modulus for the 50/50 composite is about 200 GPa. To test the validity of these values from a theoretical standpoint, we took the three tensor components (C11, C12, C44) for copper and molybdenum from the paper describing the interatomic potential we used [40] and assumed strictly uniaxial compression. Calculating the full compliance tensors for both elements, we transformed both with a series of direction cosine matrices, as given by the equation below, so that finding the elastic modulus in a particular direction would be as simple as adding a single row of values.

$$C'_{ijkl} = a_{im}a_{jn}a_{ko}a_{lp}C_{mnop} \tag{3}$$

where Cmnop is the original tensor, with C1111 representing uniaxial component for the {100} direction. The aim, ajn , ako, aip, are direction cosine matrices. We calculated the elastic modulus of the Copper in the <110> direction to be 126.5 GPa, and the elastic modulus of the Molybdenum in the <111> direction to be 303.2 GPa, demonstrating relatively good agreement between the simulated and theoretical results. Our simulation results for the elastic modulus, when averaged agree well with the experimental value obtained for the nanocomposite of 204 ± 18 GPa. It is important to note that Cu and Mo are elastically anisotropic, and so these 2 moduli values (and thus their average) differ considerably from the polycrystalline Cu and Mo measurements.

The dependence of the maximum stress on the ligament size is shown in Figure 6b. The smaller ligaments show slightly higher maximum stresses. This is consistent with the well-known "smaller is stronger" effect. Figure 6b also shows the yield strength values as a function of ligament size; they are 2.49 GPa for the 9 nm sample, 2.51 GPa for the 12 nm sample, and 2.53 GPa for the 15 nm sample. This dependence, like that of the elastic modulus, is weak in the range of ligament sizes studied here. Furthermore, these values are very close the to the experimentally measured values of 2.45 GPa.

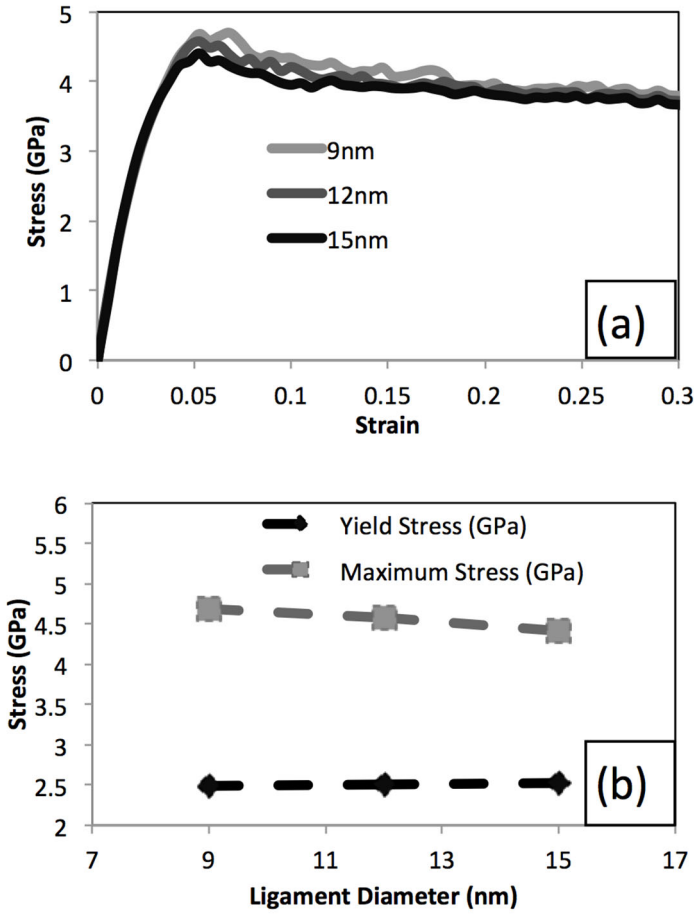

Figure 6-6: (a) The simulated stress strain curves obtained under compression for three different ligament diameters. (b) The maximum stress and yield stress as a function of ligament size, showing the "smaller is stronger" effect, as well as the yield stress values, as a function of ligament diameter.

In order to analyze the separate contributions of the constituent phases in more detail, we studied the individual atom stress tensor. By adding the hydrostatic stress tensor components corresponding to the direction of applied stress on all Cu atoms we were able to generate a stress strain curve only for the Cu component and similarly for the Mo component. The results are shown in Figure 7, showing the difference in stress evolution by atom type, as a function of strain for each ligament diameter. The overall stress of the composite is intermediate between those corresponding to the two phases. Our results indicate that about 70% of the load is taken by the Mo BCC phase, up to plastic yield in Mo. The results show, as expected, that copper yields earlier than molybdenum.

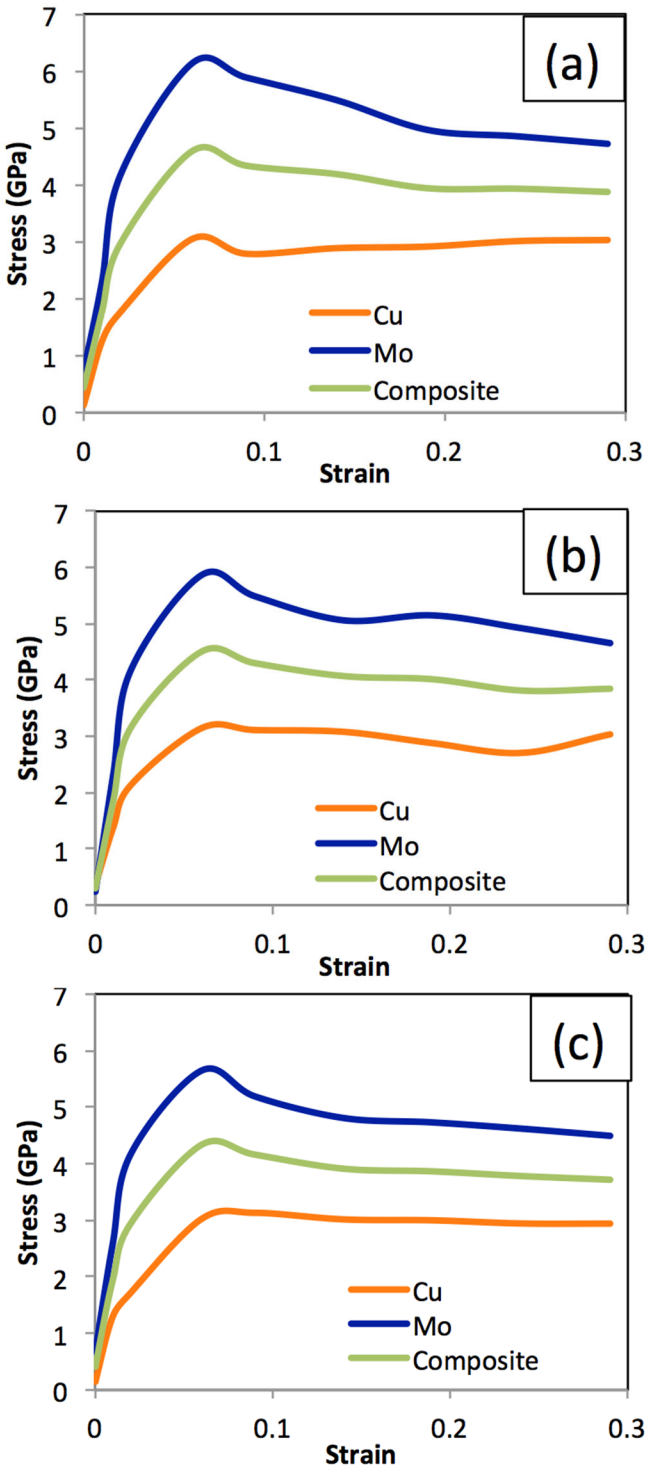

Figure 6-7: Stress Evolution separated by atom type for Cu atoms and Mo atoms, respectively. (a) is the stress profile for the 9nm sample, (b) is the stress profile for the 12nm sample, and (c) is the stress profile for the 15nm sample.

The observed ratio of load carried by the separate phases in the sample up to onset of plasticity in the whole composite at approximately 0.03 strain (($\sigma(Mo)/\sigma(Cu)$) = 2.24, averaged for all 3

samples) was found to be roughly equivalent to the ratio of directionally-dependent elastic moduli calculated form the elastic constants for our samples ((E(Mo)/E(Cu)) = 2.12). It would be interesting to see if this is a fundamental relation for other materials with similar morphologies.

The observations from Figure 7 imply that the deformation of the composite can be broken up into stages, defined by the yield of the separated components. In stage I, from the start of the deformation, both components deform elastically. In stage II, the copper yields and deforms plastically, while the molybdenum deforms elastically. In stage III, both components deform plastically. From our simulations (see section 3.5, and calculations on elastic vs. plastic strain in both lattices), we were able to pinpoint stress/strain values where first the copper yields (stage I to stage II) and the molybdenum yields (stage II to stage III). This was confirmed using the 0.2% line test. For stage II, the "origin" was taken to be the stress and strain coordinates for the end of stage I. The values for these stage transition points are given in Table 2. Interestingly, there seems to be no feature size dependence for the transition from stages I to II, and only a slight dependence going from stage II to stage III.

Table 6-2: Estimated stresses and strains for the different stages in the deformation of the composite.

	Transition from stage I to II				Transition from stage II to III			
Ligament diameter (nm)	σ (GPa)	σ Cu, (GPa)	σ Mo (GPa)	ε	σ (GPa)	σ Cu (GPa)	σ Mo (GPa)	ε,
9	2.49	1.76	4.15	0.025	4.71	3.05	6.14	0.051
12	2.51	1.79	4.18	0.023	4.56	3.15	5.87	0.048
15	2.53	1.71	4.16	0.024	4.29	3.02	5.65	0.047

Strain hardening rates and exponents for the Cu phase were calculated for stage II, and are reported in Table 3. These results also show a small feature size dependence.

Table 6-3: Strain hardening rate constants for the copper phase: linear and power law model.

Ligament diameter (nm)	Linear Strain Hardening rate (GPa/ε)	Strength Coefficient (MPa)	Strain Hardening exponent
9	61.7	1361	0.48
12	59.8	1263	0.46
15	55.1	938	0.37

6.3.5 Plastic Deformation Mechanisms

Dislocations nucleating from the interface are the main mechanism of plastic deformation for both FCC copper and BCC molybdenum phases. The nucleation process is depicted in Figure 8. The dislocations in the copper phase were identified to be Shockley partials that create stacking faults in the Cu lattice. While trailing partials are seen to come out in some cases, they often

occur later in the deformation, leaving a stacking fault behind for much of the deformation. Trailing partials often emerge at about 0.03 additional strain after nucleation of the leading partial. Due to entanglement and the interaction with other stacking faults, they often do not completely eliminate the stacking faults created by the leading partials. These dislocations travel through the Cu up to the neighboring interface, and are not transmitted to the Mo.

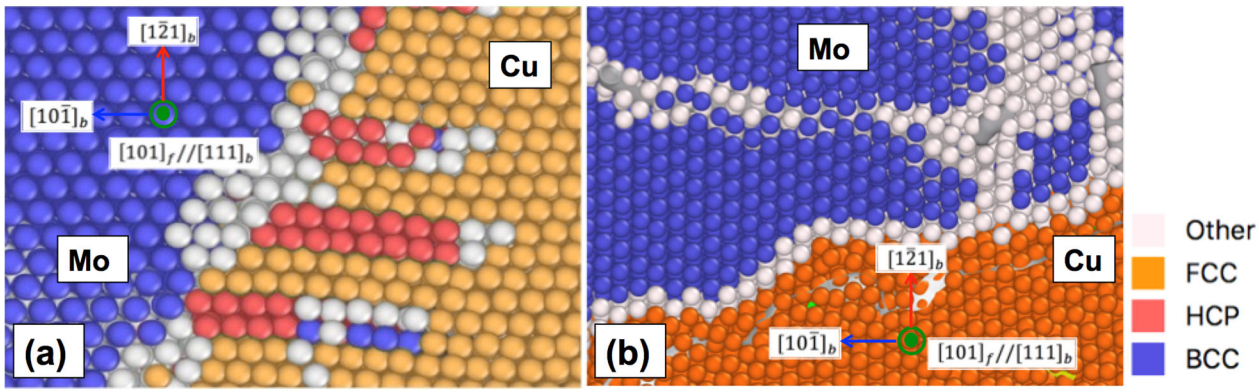

Figure 6-8: Emission of dislocations from the interface into the fcc Cu. The atoms are colored by structure type. (a) demonstrates how stacking faults following leading shockley partials in the FCC lattice, while (b) demonstrates that while there are some disordered atoms around the dislocation core, no stacking fault is evident.

As more dislocations are emitted from the interface into the Cu FCC phase, the stacking faults created can be quantified using common neighbor analysis to identify atoms with hcp-like environments. Figure 9a shows that as deformation proceeds, the fraction of hcp-like Cu atoms increases greatly. As mentioned, these stacking faults can remain in the lattice for much of the deformation run, and act as barriers to other dislocations passing through from other directions, causing entanglement, and buildup of stress. A copper ligament with stacking fault formation at 4% strain and 6% strain are shown in Figure s 9b and 9c.

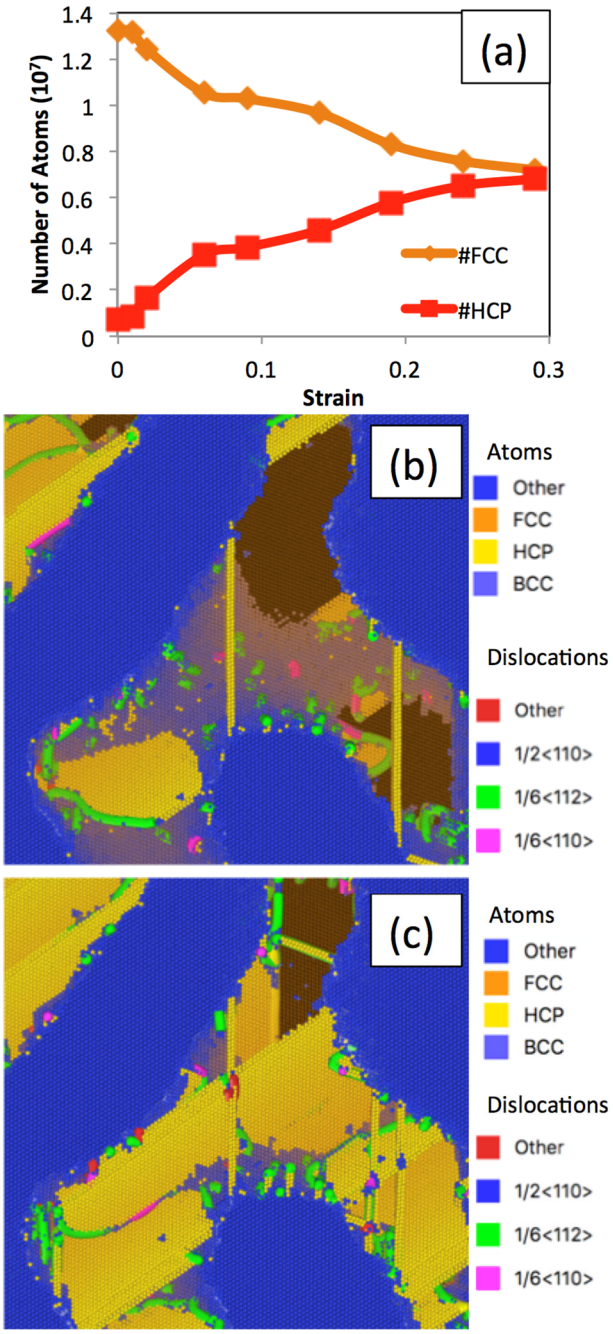

Figure 6-9: Proliferation of stacking faults in the lattice before and after the point of yield, as indicated by stacking faults (a) Evolution of structure type of copper atoms not in the interface for a slice of the 12 nm sample, (b) stacking fault profile for a single ligament before yielding. (c) stacking fault profile for a single ligament after yielding.

As Figure 9 demonstrates, the stacking faults left behind by leading Shockley partial dislocations hinder dislocations moving in other directions, leading to the near majority hcp phase change with increasing strain. The large degree of dislocation entanglement and blocking by the stacking fault planes leads to a distinct strain hardening effect, as mentioned in section 3.4, which is why when the stress profiles are separated and observed together (Figure 7) the

copper carries more or the same stress after plasticity, when the stress carried by the molybdenum decreases.

Residual dislocation density results are shown in Figure 10a. It is important to note that the higher density in the copper phase is due to dislocation entanglement and blocking by stacking faults in non-parallel planes, as mentioned earlier (10b). In fact, dislocation activity is the primary mode of deformation for both phases. The residual dislocation densities are much lower in the Mo phase because the 1/2<111> type dislocations do not leave stacking faults in the BCC structure (10c). Propagation of dislocations across the ligament can proceed unhindered by interaction with other faults. As expected from the differences in the lattice structure and Burgers vector, no dislocations were observed being transmitted from the copper to the molybdenum phase, or vice versa.

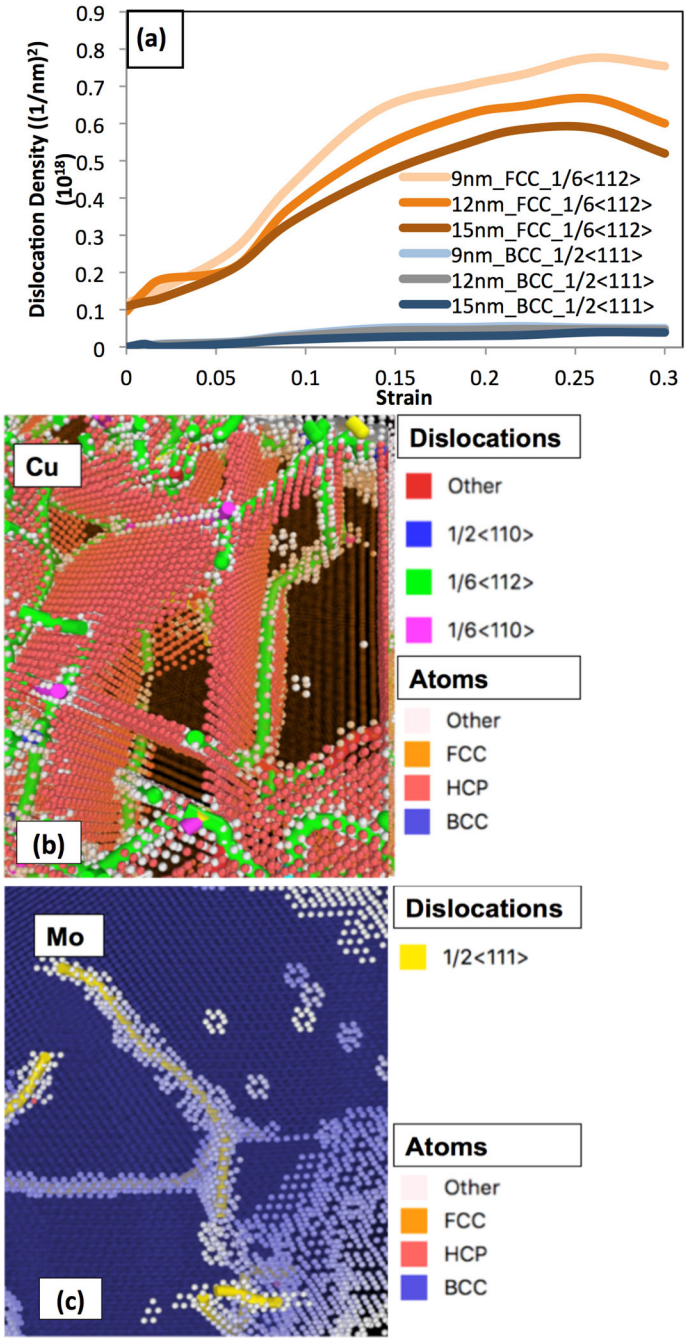

Figure 6-10: Dislocation evolution for all samples. (a) shows the dislocation density evolution of the entire series as a function of strain. (b) and (c) show the proliferation of dislocation lines in the copper and molybdenum phases, respectively, and the stacking faults that are left behind in the copper.

We also analyzed the residual elastic strain state of the sample as it underwent deformation. We calculated elastic strain along the direction of deformation at each step in the straining process for the two phases separately. To obtain the total elastic strain, we simply added these values. The results are shown in Figure 11a. The ratio of the residual elastic strain found in the two

phases is consistent with the ratio of their individual elastic moduli, up to yielding. At the final step of applied 0.3 strain, the total residual elastic strain was 0.0233, meaning that the total plastic strain should be closer to 0.277. To confirm this value, we unloaded the sample from the final deformation step, and found the total strain after relaxation to be 0.2761, a difference from the total strain of 0.0239 (Figure 11b). The unloading slope was 170.2 GPa, in agreement with the elastic modulus obtained during loading.

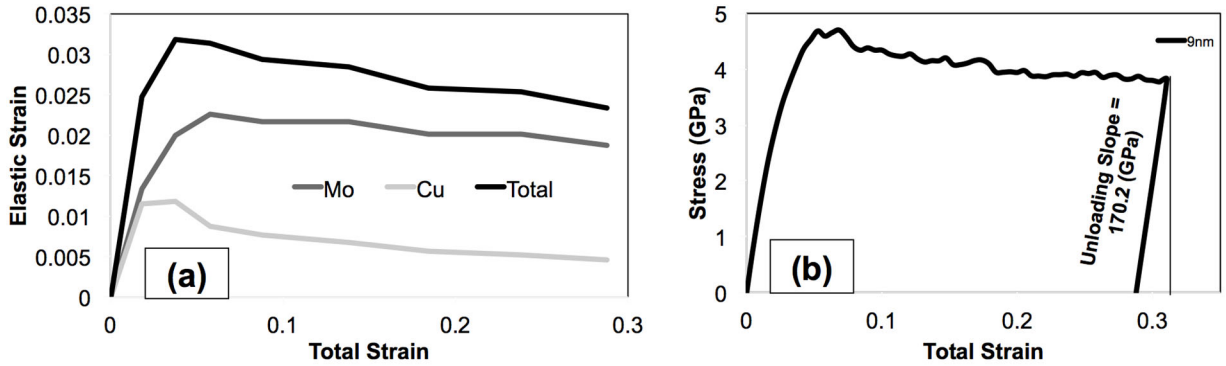

Figure 6-11: (a) A measurement of elastic strain as measured using the equilibrium lattice parameter for both the Cu and the Mo respectively; total elastic strain is simply the two curves added together. (b) The unloaded stress/strain curve with total unloaded strain equivalent to total elastic strain, and loading slope roughly equivalent to measured elastic modulus

To confirm that the measured elastic strain curves matched the onset of plasticity, we looked at the detailed stress/strain curves of the 9nm sample during the initial loading steps. It was found that the curve was in fact linear up to a strain of 0.245, and then approximately linear again up to a strain of 0.052, agreeing with the values obtained from the elastic strain curves.

As a final portion of our analysis, we looked at the atom-by-atom non-uniform displacement, defined as the atomic displacements minus the uniform deformation of the lattice. The average non-uniform displacement at the end of the compressive run was found to be 1.58 nm for the BCC phase, and 1.42 nm for the FCC phase for the 9 nm ligament diameter sample. In the BCC phase, displacement gradients are gradual, and dislocation paths can be seen in the displacement map. Dislocations glide freely from one interface to another within the ligament. In the FCC phase, dislocations tangle and encounter stacking faults, causing them to change direction, or be stopped in the interior of the ligaments. Importantly, any shear bands that may try to form in the lattice under strain are arrested by the interface, and the complex morphology ensures that any observed shearing behavior is kept as ligament-by-ligament phenomena localized to the ligament on which they occur, and uncoordinated with other shear events in other ligaments. In other words, no sample-wide shear banding is observed. In fact both parts of the lattice deform together, with total atomic non-uniform displacements rarely going above 3 nm, even after a 30% compressive deformation, with the overall morphology of the sample not being compromised. This is shown in Figure 12.

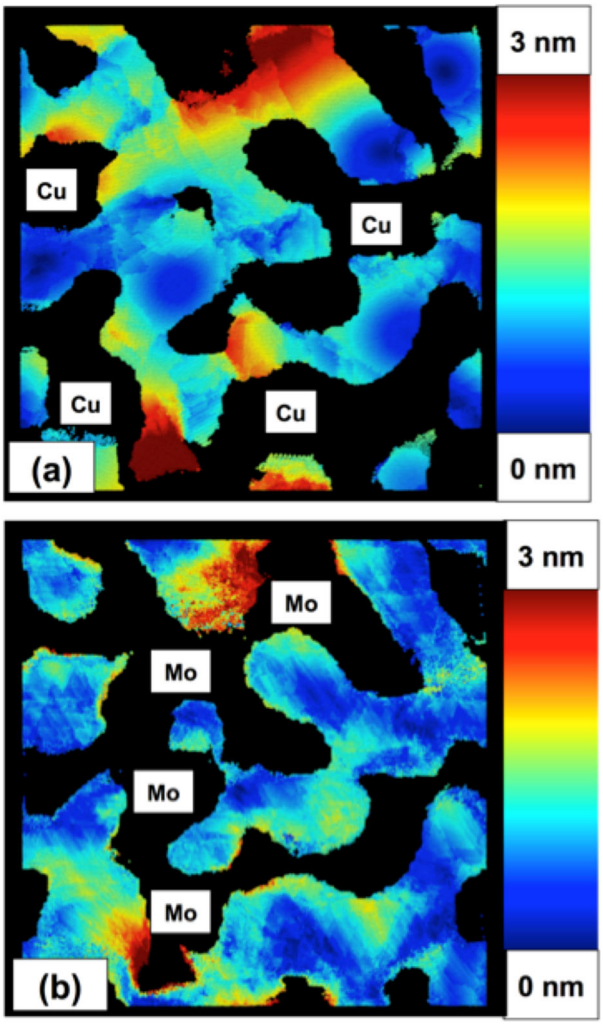

Figure 6-12: A nonuniform displacement map colored with different color schemes, separated by atom type for Molybdenum (a) and Copper (b)

6.4. Discussion

6.4.1 High strength of the bicontinuous nano-composite

Exceptional high yield strength around 2.5 GPa was measured in the bicontinuous Cu-Mo nano-composite, from both of our experiment and simulation, which is comparable to the 2.8 GPa measured in 3 nm Cu/Mo multilayers [46]. Previous studies on multilayer structures show that at 15 nm length scale, confined layer slip (CLS) accounts for the major deformation mechanism [20, 21]. Using the CLS model, the applied shear stress to propagate a glide loop, τ_cls, can be calculated as

$$\tau_{cls} = \frac{\mu b}{8\pi h}\left(\frac{4-\nu}{1-\nu}\right)\left[ln\frac{\alpha h}{b}\right] \quad (4)$$

where μ is the shear modulus, b is the length of the Burgers vector, h is the individual layer thickness, v is the Poisson's ratio and α represents the dislocation core cutoff parameter [21].

Low value of α would imply a wide dislocation core. Substituting μ = 48 GPa, b = 0.147 nm, (as calculated for 1/6<112> vectors with lattice parameter 0.361 nm) v = 0.35 for Cu and using α = 1 for compact core, τ_cls can be calculated as 0.69 GPa for hCu = 15 nm \ The normal yield strength σ_cls can be estimated as τ_cls multiplied by a Taylor factor of 3.1, which equals 1.42 GPa. Repeating this calculation for both the copper and molybdenum components, and the three feature sizes, we obtain yield values predicted by the CLS model given in Table 4. For Mo we used μ = 120 GPa, b = 0.273 nm and v = 0.32.

Table 6-4: Resolved (τ) and Yield (σ) stresses predicted by the confined layer slip model.

Ligament diameter (nm)	τ_{cls} Cu (GPa)	τ_{cls} Mo (GPa)	σ_{cls}Cu (GPa)	σ_{cls}Mo (GPa)
9	0.68	2.74	2.11	8.50
12	0.54	2.18	1.69	6.78
15	0.46	1.85	1.42	5.75

The average of the predicted yield for the copper phase across the three feature sizes is nearly identical to the averages from both the experimental and computational stress/strain curves in Figures 5 and 6, but there is larger variation in the values predicted by the CSL model. The lack of variation in the bicontinuous simulations may be related to the effects of the highly ordered interface. The bicontinuous simulations certainly give values that are consistent with the CSL model, with a weaker dependence on feature sizes.

As shown in Figure 10a, after yielding, the residual dislocation density in Cu phase increases drastically while there are only modest dislocation activities in Mo. This is expected as Mo has higher yield strength compared to Cu. When Cu starts to yield, as indicated in Figure 11, Mo is still deforming elastically. A situation of mechanical incompatibility, similar to what has been observed in heterogeneous materials, is created [51]. Because of the constraint from the Mo phase, Cu cannot plastically deform freely. Strain gradient would then be generated near the Cu/Mo interface. Geometrically necessary dislocations need be generated in Cu to accommodate this strain gradient, making Cu appear stronger. As a result, a synergetic strengthening of the intertwined phases takes place and increases the overall yield strength of the nanocomposite. The large disparity of residual dislocation density in Figure 10a evidences the above discussed strain partitioning in Cu and Mo. The entanglement of dislocations in Cu can be shown in Figure 9b and 9c, providing support to the strain hardening in Cu.

6.4.2 Co-deformation of Cu and Mo

During the compression test, deformation of the bicontinuous nano-composite can be generally divided into three stages. In stage I, both Cu and Mo deform elastically, up to 0.03 strain. As shown in Figure 11a, the strain values in Cu and Mo are the same during this stage. The whole composite deforms in a same way as a monolithic material, only that the two phases are sharing load according to their elastic modulus. As indicated in Figure 7, ratio of the load in the two phases (σ(Mo)/σ(Cu)) is 2.24, close to the ratio of directional elastic moduli of the phases at 2.12.

In stage II at a strain of approximately 0.023, Cu starts to deform plastically, through dislocation nucleation from the interface, while Mo is still in the elastic regime. As our simulation indicates, the dislocations in Cu are Shockley partials, which travel through the Cu ligament and stop at the interface, leaving a stacking fault. As discussed earlier, Mo phase is containing the deformation of Cu during this stage, lead to the generation of geometrically necessary dislocations in Cu. As the deformation further proceeds, in stage III at a strain of around 0.05, both phases deform plastically, with generation of dislocations in the Mo phase. Due to strain partitioning, drastic dislocation activities can be observed in the Cu phase. As shown in Figure 11a from the MD simulations, elastic strain is even partially relieved in Cu. Although there is a great difference in the residual dislocation activity in the two phases, after the compression test is completed at 0.3 strain, no void was observed in the sample from both the experimental and simulation results. Due to the intertwined morphology, the harder to deform Mo phase geometrically controls the deformation of the global nano-composite. Consequently, the two phases would co-deform in a synergistically way.

In the experimental samples, identifying a clear transition from both elastic to copper plastic/molybdenum elastic to both plastic (see stage discussion in section 3.4) is difficult, since the experimental results are not separated by phases. However, there is general very good agreement in the overall stress/strain curves obtained from the simulations and the experiment. This is despite the high strain rate that is necessary in the simulations.

6.4.3 Improved deformability of the bicontinuous nano-composite

Apart from the high strength, the bicontinuous intertwined morphology in metallic nano-composites provides advantage of good plastic deformability over previously studied anisotropic structures such as nanolaminates. No shear band formation was observed after over 30% compression (experimentally as well as in simulations). Many factors contribute to this improved plasticity. First of all, the Cu-Mo interface acts as a strong barrier to dislocations. Dislocation slip in Cu would not cross the interface and enter the Mo phase, and vice versa. Therefore, there is little probability for a single slip event to transmit through the whole sample and lead to strain localization. As shown in Figure 12, discrete regions where a number of dislocations have passed through can be observed in Mo phase. These regions can be between 2 and 5 lattice parameters wide, and span the width of a ligament. These are only seen in the molybdenum part of the lattice, and create discreet segments of the lattice that are more highly deformed than the lattice around them. However, as the slip is not continuous across the interface, this effect is not observed in Cu. As a result, shear band across multiple ligaments are not generated. Another factor is the large disparity in the mechanical properties of Cu and Mo, especially elastic modulus and yield strength. This is the reason the strain gradient is created and promotes high strain hardening, as described in section 3.4, and Table 3. An analogy can be drawn between our system to a heterogeneous materials, exampled by dual phase steels, which have been shown to have extraordinary work hardening and high ductility [52]. Last and probably most important factor is the bicontinuous intertwined morphology, which provides geometric constraint between the two phases. Further, the abundance of interface dislocation sources and their tortuous shape provide multiple sites for dislocation nucleation and arrestment. This promotes the wide spread of dislocation activities in Cu and less probability of shear band propagation.

6.5. Conclusions

From both experimental and simulation results, it has been shown that a Cu-Mo nano-composite with bicontinuous intertwined morphology possess simultaneous high strength and uniform deformability. Based on MD simulations, a large disparity in dislocation density was observed in the Cu and Mo phases after yielding. Strain partitioning and high strain hardening rate due to the mechanical incompatibility of the two phases explains the remarkable mechanical behavior of the nanocomposite. We conclude that a composite with nanoscale bicontinuous morphology and composed of two metals with disparate mechanical behavior in the monolithic form and containing bi-metallic interfaces that are strong barriers to dislocation glide will exhibit high strength and plastic co-deformability.

6.6 Acknowledgements

This work was supported by the National Science Foundation, DMREF program, grant numbers 1533969 and 1533557. The authors acknowledge discussion with M.J. Demkowicz, as well as assistance from B. Derby in sputter deposition and from Sean Corcoran with the structure generation and tensor calculations.

6.7 References

[1] M.J. Buehler, A. Misra, Mechanical behavior of nanocomposites, MRS Bulletin 44(1) (2019) 19-24.
[2] J. Wang, Q. Zhou, S. Shao, A. Misra, Strength and plasticity of nanolaminated materials, 2016.
[3] K. Wu, J.Y. Zhang, P. Zhang, Y.Q. Wang, G. Liu, G.J. Zhang, J. Sun, Fracture behavior and adhesion energy of nanostructured Cu/Mo multilayer films, Materials Science and Engineering: A 613 (2014) 130-135.
[4] I.J. Beyerlein, M.J. Demkowicz, A. Misra, B.P. Uberuaga, Defect-interface interactions, Progress in Materials Science 74 (2015) 125-210.
[5] Z. Liu, M.A. Monclús, L.W. Yang, M. Castillo-Rodríguez, J.M. Molina-Aldareguía, J. Llorca, Tensile deformation and fracture mechanisms of Cu/Nb nanolaminates studied by in situ TEM mechanical tests, Extreme Mechanics Letters 25 (2018) 60-65.
[6] S. Zheng, I.J. Beyerlein, J.S. Carpenter, K. Kang, J. Wang, W. Han, N.A. Mara, High-strength and thermally stable bulk nanolayered composites due to twin-induced interfaces, Nature Communications 4 (2013) 1696.
[7] J.S. Carpenter, S.C. Vogel, J.E. LeDonne, D.L. Hammon, I.J. Beyerlein, N.A. Mara, Bulk texture evolution of Cu–Nb nanolamellar composites during accumulative roll bonding, Acta Mater. 60(4) (2012) 1576-1586.
[8] J. Li, Y. Chen, S. Xue, H. Wang, X. Zhang, Comparison of size dependent strengthening mechanisms in Ag/Fe and Ag/Ni multilayers, Acta Mater. 114 (2016) 154-163.
[9] G. Dehm, B.N. Jaya, R. Raghavan, C. Kirchlechner, Overview on micro- and nanomechanical testing: New insights in interface plasticity and fracture at small length scales, Acta Materialia 142 (2018) 248-282.

[10] I. Souli, G.C. Gruber, V.L. Terziyska, J. Zechner, C. Mitterer, Thermal stability of immiscible sputter-deposited Cu-Mo thin films, Journal of Alloys and Compounds 783 (2019) 208-218.
[11] T. Xie, J. Zhu, L. Fu, R. Zhang, N. Li, M. Yang, J. Wang, W. Qin, W. Yang, D. Li, L. Zhou, The evolution of hardness in Cu-W alloy thin films, Materials Science and Engineering: A 729 (2018) 170-177.
[12] M. R, P. Bellon, R.S. Averback, Wear Resistance of Cu/Ag Multilayers: A Microscopic Study, ACS Applied Materials & Interfaces 10(17) (2018) 15288-15297.
[13] M. Damadam, S. Shao, I. Salehinia, G. Ayoub, H.M. Zbib, Molecular dynamics simulations of mechanical behavior in nanoscale ceramic–metallic multilayer composites, Materials Research Letters 5(5) (2017) 306-313.
[14] S. Weng, H. Ning, N. Hu, C. Yan, T. Fu, X. Peng, S. Fu, J. Zhang, C. Xu, D. Sun, Y. Liu, L. Wu, Strengthening effects of twin interface in Cu/Ni multilayer thin films – A molecular dynamics study, Materials & Design 111 (2016) 1-8.
[15] M.D. Gram, J.S. Carpenter, P.M. Anderson, An indentation-based method to determine constituent strengths within nanolayered composites, Acta Materialia 92 (2015) 255-264.
[16] A. Kelling, K.R. Mangipudi, I. Knorr, T. Liese, H.-U. Krebs, C.A. Volkert, Investigating fracture of nanoscale metal–ceramic multilayers in the transmission electron microscope, Scripta Materialia 115 (2016) 42-45.
[17] L.W. Yang, C. Mayer, N. Li, J.K. Baldwin, N.A. Mara, N. Chawla, J.M. Molina-Aldareguia, J. Llorca, Mechanical properties of metal-ceramic nanolaminates: Effect of constraint and temperature, Acta Materialia 142 (2018) 37-48.
[18] C.X. Huang, Y.F. Wang, X.L. Ma, S. Yin, H.W. Höppel, M. Göken, X.L. Wu, H.J. Gao, Y.T. Zhu, Interface affected zone for optimal strength and ductility in heterogeneous laminate, Materials Today 21(7) (2018) 713-719.
[19] J. Wang, A. Misra, R.G. Hoagland, J.P. Hirth, Slip transmission across fcc/bcc interfaces with varying interface shear strengths, Acta Mater 60(4) (2012) 1503-1513.
[20] B.M. Clemens, H. Kung, S.A. Barnett, Structure and Strength of Multilayers, MRS Bulletin 24(2) (2013) 20-26.
[21] A. Misra, J.P. Hirth, R.G. Hoagland, Length-scale-dependent deformation mechanisms in incoherent metallic multilayered composites, Acta Mater. 53(18) (2005) 4817-4824.
[22] B. Derby, Y. Cui, J.K. Baldwin, A. Misra, Effects of substrate temperature and deposition rate on the phase separated morphology of co-sputtered, Cu-Mo thin films, Thin Solid Films 647 (2018) 50-56.
[23] F.T.N. Vüllers, R. Spolenak, From solid solutions to fully phase separated interpenetrating networks in sputter deposited “immiscible” W–Cu thin films, Acta Mater. 99 (2015) 213-227.
[24] C.M. Müller, A.S. Sologubenko, S.S.A. Gerstl, M.J. Süess, D. Courty, R. Spolenak, Nanoscale Cu/Ta multilayer deposition by co-sputtering on a rotating substrate. Empirical model and experiment, Surface and Coatings Technology 302 (2016) 284-292.
[25] C.M. Müller, S. Parviainen, F. Djurabekova, K. Nordlund, R. Spolenak, The as-deposited structure of co-sputtered Cu–Ta alloys, studied by X-ray diffraction and molecular dynamics simulations, Acta Materialia 82 (2015) 51-63.
[26] Y. Cui, B. Derby, N. Li, A. Misra, Design of bicontinuous metallic nanocomposites for high-strength and plasticity, Materials & Design 166 (2019) 107602.

[27] Y.C. Cui, B. Derby, N. Li, N.A. Mara, A. Misra, Suppression of shear banding in high-strength Cu/Mo nanocomposites with hierarchical bicontinuous intertwined structures, Materials Research Letters 6(3) (2018) 184-190.
[28] S. Huang, J. Wang, N. Li, J. Zhang, C. Zhou, Atomistic simulations of plasticity in heterogeneous nanocrystalline Ni lamella, Computational Materials Science 141 (2018) 229-234.
[29] J. Wang, R.G. Hoagland, J.P. Hirth, A. Misra, Atomistic modeling of the interaction of glide dislocations with "weak" interfaces, Acta Materialia 56(19) (2008) 5685-5693.
[30] J. Zhou, R.S. Averback, P. Bellon, Stability and amorphization of Cu-Nb interfaces during severe plastic deformation: Molecular dynamics simulations of simple shear, Acta Materialia 73 (2014) 116-127.
[31] M. Damadam, S. Shao, G. Ayoub, H.M. Zbib, Recent advances in modeling of interfaces and mechanical behavior of multilayer metallic/ceramic composites, Journal of Materials Science 53(8) (2018) 5604-5617.
[32] G.C. Ma, J.L. Fan, H.R. Gong, Mechanical behavior of Cu-W interface systems upon tensile loading from molecular dynamics simulations, Computational Materials Science 152 (2018) 165-168.
[33] M. Asta, S.M. Foiles, A.A. Quong, First-principles calculations of bulk and interfacial thermodynamic properties for fcc-based Al-Sc alloys, Physical Review B 57(18) (1998) 11265-11275.
[34] J. Chen, M.A. Tschopp, A.M. Dongare, Role of nanoscale Cu/Ta interfaces on the shock compression and spall failure of nanocrystalline Cu/Ta systems at the atomic scales, Journal of Materials Science 53(8) (2018) 5745-5765.
[35] Q.-J. Li, B. Xu, S. Hara, J. Li, E. Ma, Sample-size-dependent surface dislocation nucleation in nanoscale crystals, Acta Mater. 145 (2018) 19-29.
[36] X.Y. Liu, R.G. Hoagland, M.J. Demkowicz, M. Nastasi, A. Misra, The Influence of Lattice Misfit on the Atomic Structures and Defect Energetics of Face Centered Cubic-Body Centered Cubic Interfaces, Journal of Engineering Materials and Technology-Transactions of the Asme 134(2) (2012).
[37] K. Kang, J. Wang, I.J. Beyerlein, Atomic structure variations of mechanically stable fcc-bcc interfaces, J. Appl. Phys. 111(5) (2012).
[38] D.A. Crowson, D. Farkas, S.G. Corcoran, Mechanical stability of nanoporous metals with small ligament sizes, Scripta materialia 61(5) 497-499.
[39] S. Plimpton, Fast Parallel Algorithms for Short-Range Molecular Dynamics, Journal of Computational Physics 117(1) (1995).
[40] H.R. Gong, L.T. Kong, B.X. Liu, Metastability of an immiscible Cu-Mo system calculated from first-principles and a derived n-body potential, Physical Review B 69(2) (2004) 024202.
[41] C. Brandl, P.M. Derlet, H. Van Swygenhoven, General-stacking-fault energies in highly strained metallic environments: Ab initio calculations, Physical Review B 76(5) (2007) 8.
[42] H. Park, M.R. Fellinger, T.J. Lenosky, W.W. Tipton, D.R. Trinkle, S.P. Rudin, C. Woodward, J.W. Wilkins, R.G. Hennig, Ab initio based empirical potential used to study the mechanical properties of molybdenum, Physical Review B 85(21) (2012) 10.
[43] N. Beets, D. Farkas, S. Corcoran, Deformation mechanisms and scaling relations in the mechanical response of nano-porous Au, Acta Mater. 165 (2019) 626-637.
[44] A. Stukowski, Visualization and analysis of atomistic simulation data with OVITO–the Open Visualization Tool, Modeling and Simulation in Materials Science and Engineering 18(015012) (2009).

[45] S. Alexander, A. Karsten, Dislocation detection algorithm for atomistic simulations, Model. Simul. Mater. Sci. Eng. 18(2) (2010) 025016.
[46] A. Stukowski, Computational Analysis Methods in Atomistic Modeling of Crystals, JOM 66(3) (2014) 399-407.
[47] I.J. Beyerlein, N.A. Mara, J. Wang, J.S. Carpenter, S.J. Zheng, W.Z. Han, R.F. Zhang, K. Kang, T. Nizolek, T.M. Pollock, Structure-Property-Functionality of Bimetal Interfaces, Jom 64(10) (2012) 1192-1207.
[48] M.J. Demkowicz, R.G. Hoagland, Structure of Kurdjumov-Sachs interfaces in simulations of a copper-niobium bilayer, Journal of Nuclear Materials 372(1) (2008) 45-52.
[49] S. Lu, H.L. Zhang, Q.M. Hu, M.P.J. Punkkinen, B. Johansson, L. Vitos, Magnetic effect on the interfacial energy of the Ni(111)/Cr(110) interface, Journal of Physics-Condensed Matter 26(35) (2014).
[50] S. Lu, Q.M. Hu, M.P.J. Punkkinen, B. Johansson, L. Vitos, First-principles study of fcc-Ag/bcc-Fe interfaces, Physical Review B 87(22) (2013).
[51] X. Wu, Y. Zhu, Heterogeneous materials: a new class of materials with unprecedented mechanical properties, 2017.
[52] K. Park, M. Nishiyama, N. Nakada, T. Tsuchiyama, S. Takaki, Effect of the martensite distribution on the strain hardening and ductile fracture behaviors in dual-phase steel, Materials Science and Engineering: A 604 (2014) 135-141.

Chapter 7: Summary and Conclusions

This dissertation describes research efforts designed to understand the mechanical response of bicontinuous porous and composite materials in the context of molecular dynamics simulations. This research highlights the role that surface and interfaces play on overall plastic response, both in the context of surface structure and surface energy. Atomic level resolution of the stress and energy distributions in these materials, as well as their residual dislocation distribution offers new insights into the causes of plasticity, and integration with continuum, phase-field, and monte-carlo methods allows for results that can be more reasonably compared with experimental findings. The key results from these studies are, in brief:

1. Load-bearing connectivity for dealloyed nanoporous samples scales as a function of the solid volume fraction squared for 5nm ligament diameter nanoporous gold. This scaling factor can be applied to the Gibson-Ashby relations directly, and gives reasonable results.
2. For nanoporous gold structures with ligament diameters less than 20 nm, a distinct tension/compression asymmetry ratio can be observed with yield response diverging with decreasing ligament diameter. Structures can be modeled as a forest of nanowires, and have higher yield stress in tension, and lower yield stresses in compression.
3. The magnitude of the tension/compression asymmetry observed in the yield response of nanoporous gold can be accurately predicted with a model based on the surface area to volume ratio (S/V) and surface stress (f).
4. Fracture in nanoporous gold can be effectively modeled with deformation mechanisms nearly identical to those observed in experimental fracture samples, with nearly identical propagation rates and stress intensity (K) via a combined MD/continuum mechanics simulation method.
5. Sequential necking and fracture of ligaments ahead of a crack tip can be accurately predicted, based on their shape, diameter, and crystalline orientation relative to the advancing tip. This can hopefully be integrated into an optimizable algorithm for predictive failure in the future.
6. The addition of silver into a nanoporous lattice causes nearly perfect linear scaling of yield response and elastic modulus that one would expect in a well-ordered, defect-free, relaxed structure. Yield response of a nanoporous lattice seems to be entirely dependent on the surface stress, and results fit nicely with the yield model from chapter 3.
7. Phase-separated bicontinuous copper and molybdenum nanocomposites preferentially relax to a Kurdjimov-Sacchs interface orientation relationship, in a structure with ligament diameters ranging from 9nm-15nm. No shear banding is observed, even after 30% compressive loading. Elastic strain never exceeds 2.3%. Minimal disorder at the interface means that even for the smallest ligament diameter, the material approaches theoretical strength.
8. Phase separation corresponds to stress separation proportional to the ratio of elastic moduli up to plasticity in the model composite structure. Plasticity events correspond almost exactly to the predictions from confined layer slip stresses necessary to nucleate a glide loop. This morphology has yet to be investigated for other materials, but this morphology has the potential to be a model for a new class of high-strength, easily manufactured composite materials.